

University of Bath



PHD

Analysis of medaka YAP mutant affecting 3D body shape formation

Wang, Huijia

Award date:
2015

Awarding institution:
University of Bath

[Link to publication](#)

General rights

Copyright and moral rights for the publications made accessible in the public portal are retained by the authors and/or other copyright owners and it is a condition of accessing publications that users recognise and abide by the legal requirements associated with these rights.

- Users may download and print one copy of any publication from the public portal for the purpose of private study or research.
- You may not further distribute the material or use it for any profit-making activity or commercial gain
- You may freely distribute the URL identifying the publication in the public portal ?

Take down policy

If you believe that this document breaches copyright please contact us providing details, and we will remove access to the work immediately and investigate your claim.

Download date: 23. May. 2019

Analysis of medaka YAP mutant affecting 3D body shape formation

Huijia Wang

A thesis submitted for the degree of Doctor of Philosophy

University of Bath
Department of Biology & Biochemistry
October 2014

COPYRIGHT

Attention is drawn to the fact that copyright of this thesis rests with the author. A copy of this thesis has been supplied on condition that anyone who consults it is understood to recognise that its copyright rests with the author and that they must not copy it or use material from it except as permitted by law or with the consent of the author.

This thesis may be made available for consultation within the University Library and may be photocopied or lent to other libraries for the purposes of consultation with effect from.....
Signed on behalf of the Faculty/School of.....

Table of contents	2
List of Figures	6
List of Tables	8
Acknowledgements	9
Abstract	10
List of Abbreviations	11
Chapter 1: Introduction	13
1.1 Three dimensional (3D) body shaping	14
1.2 The role of the extracellular matrix (ECM) in the formation of 3D organs	14
1.3 Yes-associated-protein (YAP) and Hippo pathway	15
1.3.1 Yes-associated-protein (YAP)	15
1.3.2 The mammalian Hippo signalling pathway	17
1.3.3 The Hippo pathway in organ size regulation and tumorigenesis	19
1.4 Medaka (<i>Oryzias latipes</i>) as a model organism	21
1.5 Aims of the project	24
Chapter 2: Materials and Methods	25
2.1 Fish husbandry	25
2.1.1 Medaka strains used	25
2.1.2 Incubation and staging of embryos	25
2.2 Dechoriation of medaka embryos	25
2.3 Microinjection of medaka embryos	26
2.3.1 Morpholino oligonucleotide knockdown analysis in medaka	27
2.3.2 Phenotypic rescue experiments	27
2.3.3 70kDaFN mRNA injection experiments	28
2.3.4 MNFP injection experiments	28
2.4 Genotyping of medaka embryos	28
2.5 Whole-mount <i>in situ</i> hybridisation in medaka embryos	28
2.5.1 Fixation, dehydration and rehydration	29

2.5.2 Proteinase K digestion	29
2.5.3 Prehybridisation and hybridization	30
2.5.4 Blocking and antibody incubation	30
2.5.5 Staining reaction and clearing	30
2.5.6 Imaging	31
2.6 cDNA cloning and construction	32
2.7 Whole-mount immunohistochemistry (IHC) of medaka embryos	32
2.8 Cryosectioning and immunofluorescence staining of medaka embryos	34
2.8.1 Embedding and sectioning	34
2.8.2 Antibody staining	35
2.9 Time-lapse microscopy imaging of live embryos during morphogenesis	36
2.10 Assessment of epiboly progression in medaka embryos	36
2.11 Enveloping layer cell shape analysis during gastrulation	36
2.12 Gravity experiments	37
2.13 Human 3D spheroid analysis	38
2.14 Western blotting	39
2.15 Quantitative RT-PCR analysis	40
2.16 Statistical analyses	40
Chapter 3: General characterization of medaka <i>hirame</i> (<i>hir</i>) mutant	41
3.1 Introduction	42
3.1.1 Identification of Medaka <i>hirame</i> (<i>hir</i>) mutant	42
3.1.2 Role of YAP during embryogenesis	44
3.1.3 Medaka epiboly	45
3.1.4 Aims	46
3.2 Results	47
3.2.1 Yes-associated protein (YAP) is mutated in <i>hirame</i> mutants	47
3.2.2 <i>hirame</i> mutants exhibit a slow epiboly phenotype	50
3.2.3 Organs/tissues are found collapsed and misaligned in <i>hirame</i> mutants	52
3.2.4 Somitogenesis is disturbed in <i>hirame</i> mutants	54

3.2.5 <i>hirame</i> mutants is hyper sensitive to external forces	57
3.2.6 Pigmentation is affected in <i>hirame</i> mutants	59
3.2.7 Cell proliferation defects do not underlie the <i>hirame</i> phenotype	61
3.3 Discussion	63
3.3.1 Medaka YAP mutant, <i>hirame</i> , exhibits a unique flattened phenotype	63
3.3.2 Four major traits underlie the <i>hirame</i> mutant phenotype including tissue collapse, tissue mislocation/misalignment, absence of essential organs and cell migration defects	63
3.3.3 YAP is required to maintain 3D body shape against external forces	64
3.3.4 YAP is required for neural crest development and retinal pigment epithelium formation	65
3.3.5 YAP and TAZ divides functions in medaka and cell proliferation defects do not underlie the <i>hirame</i> phenotype	66
3.3.6 Summary	66
Chapter 4: Analysis of sensory organ formation in <i>hirame</i> mutants	68
4.1 Introduction	69
4.1.1 Overview of sensory placodes	69
4.1.2 Induction of sensory placodes	71
4.1.3 Genes involved in sensory placodes development	72
4.1.4 Development of sensory organs in medaka embryo	73
4.1.4.1 Olfactory system formation in medaka	73
4.1.4.2 Eye formation in medaka	73
4.1.4.3 Ear development in medaka	74
4.1.5 Aims	74
4.2 Results	75
4.2.1 Formation of sensory placodes is affected in <i>hirame</i> mutants	75
4.2.2 The olfactory placode was mislocated and invagination did not occur in <i>hirame</i> mutants	76
4.2.3 Malformation of the retina and the lens in <i>hirame</i> mutant	

	82
4.2.4 Early ear development is disrupted in <i>hirame</i> mutants	86
4.3 Discussion	90
4.3.1 The development of sensory placodes is affected in <i>hirame</i> mutants	90
4.3.2 Sensory placodes do not invaginate and become mislocated with the presence of multiple placodes at later stage in <i>hirame</i> mutants	91
4.3.3 Filopodia formation between the sensory placodes and adjacent tissues is affected in <i>hirame</i> mutants	93
4.3.4 Coordinated tissue/organ growth is affected in <i>hirame</i> mutants	95
Chapter 5: Yes-associated protein (YAP) is required for Fibronectin (FN) fibril assembly	96
5.1 Introduction	97
5.1.1 Extracellular matrix (ECM) and Fibronectin (FN)	97
5.1.2 The role of Fibronectin (FN) during morphogenesis	99
5.1.2.1 FN in heart formation	99
5.1.2.2 FN in vascular morphogenesis	100
5.1.3 Formation of the Cuvierian ducts (CDs) and heart in medaka embryos	100
5.1.4 FN and somitogenesis	103
5.1.5 Aims	104
5.2 Results	105
5.2.1 Abnormal Fibronectin (FN) localisation is observed during heart and Cuvierian ducts (CDs) formation in <i>hirame</i> mutants	105
5.2.2 <i>hirame</i> mutants exhibit aberrant Fibronectin (FN) assembly	108
5.2.3 Fibronectin (FN) assembly defects result in tissue dislocation but not flattening of tissues	111
5.2.4 Tissue polarity seems unaffected in <i>hirame</i> mutants while the oriented cell division is affected	115

5.2.5 Fibronectin-integrin interactions is affected in <i>hirame</i> mutants	117
5.2.6 Tissue tension appears reduced in <i>hirame</i> mutants	119
5.2.7 Actomyosin activation is reduced in <i>hirame</i> mutants	120
5.2.8 Tissue tension of enveloping layer (EVL) is reduced in <i>hirame</i> mutants	121
5.2.9 Over-polymerisation of F-actin leads to the aberrant Fibronectin assembly	123
5.3 Discussion	127
5.3.1 YAP is required for the formation of heart and Cuvierian ducts (CDs) via regulating Fibronectin (FN) assembly	127
5.3.2 Deficient oriented cell division contributes to tissue flattening in <i>hirame</i> mutants	129
5.3.3 FN fibril assembly is aberrant in <i>hirame</i> mutants but blockage of FN assembly does not cause tissue flattening	129
5.3.4 YAP is required for FN-integrin interaction that further regulates the coordinated tissue/organ growth	130
5.3.5 Actomyosin activity is reduced in <i>hirame</i> mutants and tissue tension is significantly reduced in the absence of YAP	131
Chapter 6: General discussion	133
6.1 The <i>hirame</i> phenotype and its underlying causes	134
6.2 Is the actomyosin-dependent tension main cause of the <i>hirame</i> phenotype?	136
6.3 YAP regulation of tissue tension and FN assembly is probably mediated by ARHGAP18	137
6.4 How YAP regulates the global 3D body shape of vertebrates?	137
6.5 Future work	140
Chapter 7: References	142
Chapter 8: Appendix	158
8.1 FN matrix is required for the formation of Cuvierian Ducts (CDs)	158
8.2 Publications	159

List of Figures

Figure 1.1 Schematic of YAP protein structure	16
Figure 1.2. Schematic of mammalian Hippo pathway	19
Figure 1.3 Images of live medaka embryos at st.19 (27.5 hpf), 25 (50 hpf) and 32 (101 hpf)	22
Figure 2.1 Schematic views of microinjection	26
Figure 2.2 Schematic views of three embedding orientations	38
Figure 3.1 A non-sense mutation causes the <i>hir</i> phenotype	43
Figure 3.2 The flattened <i>hirame</i> phenotype	43
Figure 3.3 Schematic of gastrulation in medaka	46
Figure 3.4 YAP is mutated in <i>hirame</i> mutant	48
Figure 3.5 <i>hirame</i> mutants exhibit slow epiboly	51
Figure 3.6 Organ collapse and misalignment in <i>hirame</i> mutants	53-54
Figure 3.7 Somitogenesis is disrupted in <i>hirame</i> mutants	55-56
Figure 3.8 <i>hirame</i> mutant is hyposensitive to external forces	57-58
Figure 3.9 Pigmentation is affected in <i>hirame</i> mutants	60
Figure 3.10 Cell proliferation defects do not contribute to the <i>hirame</i> phenotype	61
Figure 4.1 Schematic view of morphogenetic processes associated with the development of the early cranial placodes	69
Figure 4.2 Fate map of sensory placodes in a medaka embryo	70
Figure 4.3 Whole-mount <i>in situ</i> hybridisation of <i>Sox3</i> showing the disrupted sensory placodes formation in <i>hir</i> mutant	76
Figure 4.4 Expression patterns of medaka olfactory and otic placodes specific markers, <i>dlx3</i> and <i>cdh1</i> during early morphogenesis in WT embryos and <i>hir</i> mutants	78-79
Figure 4.5 Olfactory placode formation and later invagination is disturbed in <i>hir</i> mutants	81
Figure 4.6 Abnormal filopodia formation can be seen between the lens and retina in <i>hirame</i> mutants	83
Figure 4.7 Pronounced apoptosis is detected where the optic cup detaches from the forebrain and opens up	84

Figure 4.8 Multiple dislocated differentiated lenses are observed in <i>hirame</i> embryos	85
Figure 4.9 Early ear development is disturbed in <i>hirame</i>	87-88
Figure 5.1 Schematic views of modular structure of Fibronectin (FN) and the process of FN matrix assembly	98
Figure 5.2 Schematic summarising Cuvierian ducts (CDs) formation in medaka embryos	102
Figure 5.3 Medaka embryo heart development	103
Figure 5.4 Aberrant fibronectin deposition is observed during the formation of Cuvierian ducts (CDs) in <i>hirame</i> mutants	105-106
Figure 5.5 Aberrant Fibronectin deposition is observed during the heart formation in <i>hirame</i> mutants	107-108
Figure 5.6 Fibronectin fibril assembly is disrupted in <i>hirame</i> mutants	110-111
Figure 5.7 Blockage of FN assembly caused tissue dislocation but not flattening of tissues	112-113
Figure 5.8 Fibronectin assembly is completely blocked in FN 70kD injected WT embryos	114
Figure 5.9 Tissue polarity remains normal in <i>hirame</i> mutant	115
Figure 5.10 Oriented cell division is affected in the <i>hirame</i> lens placode	116
Figure 5.11 Fibronectin-integrin signalling is disrupted in <i>hirame</i> mutants	118
Figure 5.12 Tissue tension was reduced in <i>hirame</i> lens and retina	119-120
Figure 5.13 Phosphorylated MRLC levels are reduced in <i>hirame</i> mutants	121
Figure 5.14. EVL tension is reduced in <i>hirame</i> mutant embryos	122-123
Figure 5.15 F-actin and FN localizations in 2D cultured YAP KD human cells and <i>hir</i> mutant embryos	125-126
Figure 6.1 A model of YAP regulation of vertebrate 3D body shape	139
Figure 8.1 Fine Fibronectin matrix is required for guiding the migration of endothelial precursors that forms Cuvierian Ducts (CDs)	158

List of Tables

Table 1.1 Summary of the common stages of medaka development cited in this work and the corresponding hours of development	23
Table 2.1 Proteinase K treatment time for embryos at different stages	29
Table 2.2 Optimised dilution of anti-sense probes used in WISH	32
Table 2.3 Antibodies used for immunofluorescence staining	34
Table 3.1 Phenotype of medaka YAP MO injected embryos	49
Table 4.1 List of molecular markers used to detect the olfactory, lens and otic placode in this chapter	73
Table 6.1 Summary of the <i>hirame</i> phenotype and the potential underlying causes	134-135

Acknowledgements

I would like to express my deep appreciation and gratitude to my supervisor Dr Makoto Furutani-Seiki for his patient guidance throughout my PhD study; Dr Robert Kelsh for the provision of the fish facility; Marc for his maintenance of the fish and the University of Bath.

My thanks also go to my BFF Lei for her generous hospitality whenever I visit London; my lab mate, Sean for his invaluable statistical advice, being as a “punch-bag” and a “taxi driver” and everyone else in laboratory 0.39 and writing up room 0.40.

Besides, I would like to thank NDM for his gentle care and sweet encouragement over the past few years, which made my journey of research more colourful and delightful.

Last but not least, I must offer my special acknowledgement to my beloved parents for their devoted love, financial support and thoughtful care throughout my life.

Abstract

Vertebrate body shape depends on precise three-dimensional (3D) alignment of individual tissues which themselves have a defined 3D shape, but it is still unknown how this is achieved. Understanding the mechanisms by which 3D organs are generated and aligned is important for the improvement of regenerative medicine, which aims to facilitate 3D tissue/organ formation. A genome-wide medaka (*Oryzias latipes*) mutagenesis screen identified the *hirame* (*hir*) mutant, which has a point mutation in the WW1 protein domain of the Yes-associated protein (YAP) gene. The *hir* mutant exhibits a pronounced flattened body in which individual organs collapse and are not properly aligned. These features of the mutant make it an ideal model organism for the study of how individual 3D tissues/organs are developed and how they align coordinately to generate the global body shape.

In this study, YAP function in an intact mutant animal was analysed by various means, including immunohistochemistry (IHC) and time-lapse confocal microscopy, revealing a previously unrecognised crucial role for YAP. This study demonstrates that a single gene product governs the global 3D body shape by mediating not only cell behaviour within the tissue for production of its 3D morphology but also coordinated morphogenesis of adjacent tissues through ECM assembly around the tissues. Further *in vivo* and *in vitro* analyses demonstrated that the function of YAP is most likely regulated by actomyosin-mediated tissue tension.

List of Abbreviations

aPKC	atypical protein kinase C
AP	Alkaline-phosphatase
β-act	β -actin
BCIP	X-phosphate/5-bromo-4-chloro-3-indolyl phosphate
BSA	Bovine serum albumin
BSS	Balanced salt solution
CDs	Cuverian ducts
DAPI	4', 6-diamino-2-phenylindol-dihydrochloride
DIG	Digoxigenin
DMSO	Dimethyl sulphoxide
ECM	Extracellular matrix
EGFP	Enhanced green fluorescent protein
EtOH	Ethanol
EVL	Epithelial enveloping layer
FBS	Fetal bovine serum
Fig	Figure
FITC-dex	Fluorescein isothiocyanate dextran
FN	Fibronectin
GFP	Green fluorescent protein
h	Hour
<i>hir</i>	<i>hirame</i>
hpf	Hours Post Fertilization
Hyb B	Hybridisation buffer
ID	Inner diameter
IHC	Immunohistochemistry
KD	Knock-down
LWR	Length-width ratio
MeOH	Methanol
MNFP	Membrane-EGFP and H2B-RFP (nuclear red fluorescent protein)
MO	Morpholino
OD	Outer diameter
O/N	Overnight

papc	Paraxial protocadherin
PBS	Phosphate-buffered saline
PBST	Phosphate-buffered saline with 0.1% tween
PFA	Paraformaldehyde
Pro K	Proteinase K
PSM	Presomitic mesoderm
RT	Room temperature
SB	Splicing blocking
St	Stage
TB	Translation blocking
TCA	Trichloroacetic acid
WT	Wild-type
YAP	Yes-associated protein
ZO-1	Zonula occluden-1

Chapter 1: General introduction

1.1 Three dimensional (3D) body shaping

The vertebrate body is not just what we can see from outside, it is composed of organs/tissues that have their own 3D structures and alignment with its adjacent tissue to form a functional organ. For example, the nascent lens and naive retina undergo coordinated growth and invagination to position the lens correctly in the eye cup, thus forms a functional eye (Chauhan *et al.*, 2009). The ability of a living organism to adapt to changes from both external environment and the internal environment is essential during development (Nelson & Bissell, 2006). However, there was no animal model that directly showed how the body is shaped by withstanding external forces. *In vitro* tissue culture experiments suggest that 3D tissue morphogenesis depends on three components: force generation, transmission of force through the tissue, and response of tissues and extracellular matrix (ECM) to force (Mammoto & Ingber, 2010). The major cellular force-generating machinery is actomyosin, which involves motor protein myosins interacting with cytoskeletal structures such as actin fibers in the cell cortex (Vicente-Manzanares *et al.*, 2009). Cortical tensile forces are transmitted via cell-cell contact, generating tissue tension, or cell-ECM adhesions, thereby controlling assembly of the ECM, which serves as a scaffold for 3D tissue construction (Singh & Schwarzbauer, 2010). Although *in vitro* experiments revealed the three mechano-morphological processes, little is known about how these dynamic processes are orchestrated genetically to generate 3D body shape. A model organism is therefore needed to help us understand how 3D body shape is generated *in vivo*.

1.2 The role of the extracellular matrix (ECM) in the formation of 3D organs

The extracellular matrix (ECM) functions not only as a structural support for the formation of 3D tissues/organs, but also provides cues for cell proliferation and differentiation, supports the maintenance of differentiated tissues (Daley *et al.*, 2008). Tissue morphogenesis is regulated by various ECM components. Morphogenesis of the blood vessels, salivary gland, lung, breast, prostate, pancreas and kidney, is dependent on the ECM activities as well as on soluble factors (Kleinman *et al.*, 2003). Several ECM knockout mice are

embryonic lethal, including laminin, fibronectin (FN), collagen and perlecan, suggesting ECM is also important during early embryogenesis (Gustafsson & Fassler, 2000). Though ECM assembly is yet to be fully understood, the assembly process shows a hierarchy. ECM is linked to the internal cytoskeleton by transmembrane receptors integrins (Daley *et al.*, 2008). Integrin $\alpha_5\beta_1$ -mediated assembly of fibronectin (FN) into fibrils on the cell surface is required for other ECM proteins deposition (Daley *et al.*, 2008). Mechanical cues including tissue tension are necessary for FN assembly (Singh *et al.*, 2010). Analysing intact animals and identifying mutants affecting these processes is thus essential to elucidate the relationship between ECM formation and organogenesis.

1.3 Yes-associated-protein (YAP) and Hippo pathway

1.3.1 Yes-associated-protein (YAP)

Yes-associated protein (YAP) was first identified from chicken embryonic fibroblasts as a WW-domain protein that binds to the Src family kinase c-Yes via its SH3 binding motif (Sudol, 1994). YAP homologues were also identified later in mice and humans (Sudol *et al.*, 1995b) and an orthologue (Yorkie, Yki) in *Drosophila* (Huang *et al.*, 2005), as well as a mammalian paralogue named TAZ (transcriptional coactivator with PDZ-binding motif) (Wang *et al.*, 2009). YAP is evolutionarily conserved and it is believed that YAP have a function more in epithelium while TAZ is expressed more mesenchymally (Hong and Yaffe, 2006).

YAP is a multifunctional adaptor protein which contains several protein interaction domains including a TEAD binding domain, which is the main transcription factor partner for YAP, a 14-3-3 binding site, two WW domains, an SH3-binding motif and a PDZ binding motif at its C-terminus (Sudol *et al.*, 2012; Fig.1.1). The PDZ domain is critical for YAP crosstalk with other proteins involved in regulating organ size, such as the Wnt pathway (Dvl) and members of TGF β signalling (PALS1, AMOT and PATJ) (Cherrett *et al.*, 2012).

YAP is a 65kDa proline-rich phosphoprotein and functions as a transcriptional co-activator (Sudol *et al.*, 1995a). YAP positively regulates cell growth,

survival and proliferation to control organ growth (Saucedo and Edgar, 2007). Activation of YAP can expand the population of multipotent stem cells in the small intestine (Camargo *et al.*, 2007). Indeed, several reports have showed that YAP can regulate the neural progenitor pool. Overexpression of YAP in *Xenopus* expanded the *Pax3*⁺ neural progenitor pool in conjunction with TEAD binding (Gee *et al.*, 2011). YAP overexpression in the chick neural tube also caused expansion of the neural progenitor population (Cao *et al.*, 2008).

Activation and localisation of YAP is regulated by its phosphorylation at various sites. Human YAP has five conserved HXRXXS (H is histidine, R is arginine, S is serine) LATS phosphorylation motifs (Zhao *et al.*, 2010b). When phosphorylated at Serine 127 (S127), YAP nuclear translocation is inhibited by binding to 14-3-3 in the cytoplasm (Zhao *et al.*, 2007; Fig.1.1). The TEAD-binding region is required for 14-3-3 binding. S381 phosphorylation has been shown to initiate degradation of YAP (Zhao *et al.*, 2010b; Fig.1.1). The functions of phosphorylation at the three other sites (S61, S109 and S164) by LATS remain to be elucidated (Zhao *et al.*, 2010b). However, complete blockage of LATS phosphorylation by mutation of all five phosphorylation sites from serine to alanine can enhance nuclear localisation (called YAP5SA), gives a more active form of YAP in enhancing cell proliferation than mutation at just one site (YAPS127A), indicating these other serine residues are also crucial for YAP activity (Zhao *et al.*, 2009).

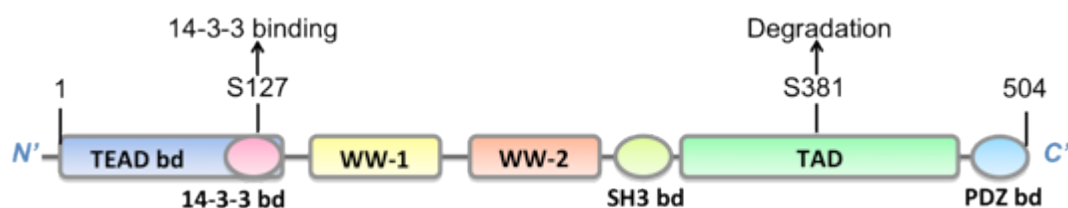


Figure 1.1 Schematic of YAP protein structure. YAP is a multifunctional adaptor protein which contains several protein interaction domains, including a TEAD binding domain praline-rich N-terminal, a 14-3-3 binding site, two WW domain, SH3 binding motifs, a C-terminal transcription activation domain and a consensus PDZ binding motif at its C-terminus. When phosphorylated at S127, 14-3-3 binding fosters YAP cytoplasmic sequestration, and when phosphorylated at S381, YAP degradation is initiated. TAD, transcription activation domain; bd, binding domain. Schematic modified from (Cherrett *et al.*, 2012).

1.3.2 The mammalian Hippo signalling pathway

The Hippo signalling pathway is gaining recognition as a major regulator of epithelial tissue and organ growth (Dong *et al.*, 2007; Camargo *et al.*, 2007), as well as tissue regeneration and self-renewal of stem cells (Zhao *et al.*, 2011). The core components in mammalian Hippo pathway are MST1/2, Sav1, LATS1/2, MOB1 and YAP/TAZ (Cherrett *et al.*, 2012; Fig.1.2). Two Hippo pathway components, Yorkie (Yki), the *Drosophila* homolog of YAP, together with Warts (*Drosophila* homolog of LATS1/2) can mediate fly intestinal stem cell proliferation and regeneration (Staley & Irvine 2010). Another study established an important role of YAP in mouse embryonic stem cell-renewal and pluripotency (Lian *et al.*, 2010). The research group also found YAP activation is associated with mouse embryonic fibroblasts generated iPS cells (Lian *et al.*, 2010).

The Hippo signalling pathway mediates cell number by phosphorylating and inhibiting the YAP/TAZ transcription coactivators to suppress cell proliferation and accelerate apoptosis and therefore regulates organ size (Zhao *et al.*, 2010a). Hippo pathway is closely associated with tumorigenesis, as its main components are either tumor suppressors or oncogenes (Zhao *et al.*, 2007). The pathway is also highly conserved within mammals (Saucedo and Edgar, 2007).

Recently, YAP has been found as one of the most downstream targets of Hippo pathway acting as a nuclear executor of the upstream inputs (Zhao *et al.*, 2007). The function of YAP is negatively regulated by the upstream components through phosphorylation (Camargo *et al.*, 2007). When phosphorylated, YAP is found in the cell plasma, binding 14-3-3 protein. YAP exerts its functions by shuttling into the nucleus to activate transcription of target genes by binding to the transcription factors, such as TEAD (Fig.1.2).

More focus has been put on the upstream regulators/inputs that activate Hippo signalling. Lately, many additional components of the Hippo pathway have been discovered which inserts more insight into how cells sense when to stop growing through extracellular/inter-cellular cues and activate the Hippo

pathway to inhibit growth. One example is the Crumbs (Crb) polarity complex (comprising Crb, PALS1-associated tight junction protein and Stardust, Bilder *et al.*, 2003). The Crb can regulate tissue size in *Drosophila* through the Hippo pathway via the effector Expanded (Ex, Chen *et al.*, 2010 & Grzeschik *et al.*, 2010). Apart from Ex, previous work in *Drosophila* has also indicated other apical membrane-associated FERM-domain proteins Merlin (Mer) and Kibra as the upstream regulators of Hippo pathway (Hamaratoglu *et al.*, 2006 & Baumgartner *et al.*, 2010). Another upstream regulator of the Hippo signalling pathway is the E-cadherin/catenin complex (Kim *et al.*, 2011). E-cadherin mediates the subcellular localisation of YAP and Hippo signalling pathway via controlling cell-cell contact directly to regulate cell proliferation (Kim *et al.*, 2011). E-cadherin-bound- β -catenin at the membrane is required for the regulation of the downstream activity of the Hippo signalling pathway. Mer also interacts with β -catenin to activate the Hippo pathway (Kim *et al.*, 2011). The adaptor protein α -catenin, one essential component of adherens junctions (AJs), also regulates Hippo signalling. YAP is negatively regulated by α -catenin through phosphorylation via its 14-3-3 binding domain (Schlegelmilch *et al.*, 2011, Fig. 1.2).

However, these upstream components have been studied mainly in the fly Hippo pathway with the exception of the mammalian Merlin orthologue, NF2 (Zhang *et al.*, 2010), thus further investigation is needed to clarify the relevance of these proteins in mammals in regulating the activity of YAP. Compared to the core components (MST1/2, Sav1, LATS1/2, MOB1 and YAP/TAZ) in the pathway, advanced definition of these upstream complexes is necessary.

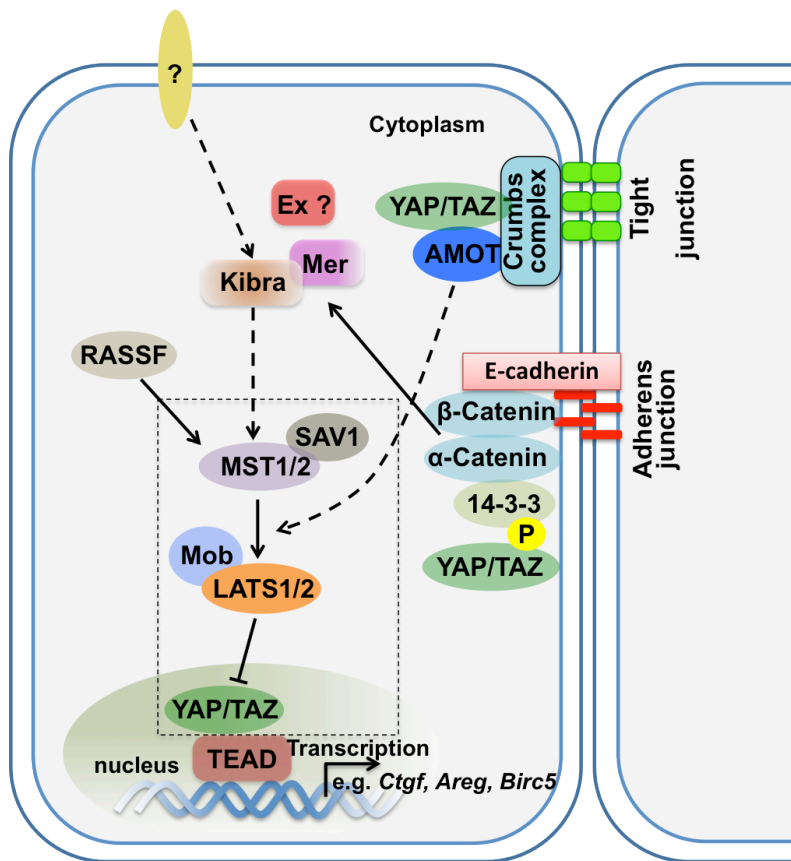


Figure 1.2. Schematic of mammalian Hippo pathway. The Hippo pathway is a serine/threonine kinase cascade. Core components in mammalian Hippo pathway include MST1/2, Sav1, LATS1/2, MOB1 and YAP/TAZ (contained within the dashed box). The nuclear executor of the pathway, YAP/TAZ, exerts its function by moving into the nucleus where it binds DNA indirectly via several transcription factors such as TEAD, to activate transcription of different target genes. YAP/TAZ is negatively regulated by upstream components of the pathway via phosphorylation, which leads to the cytoplasmic sequestering of YAP/TAZ. Upstream complexes, such as Crumbs complex at the tight junctions and E-cadherin/catenin complex at the adherens junctions can also regulate YAP/TAZ. Dashed arrows represent unresolved mechanisms, and question marks indicate unconfirmed members of the pathway. Schematic modified from (Ramos & Camargo, 2012; Kim *et al.*, 2011)

1.3.3 The Hippo pathway in organ size regulation and tumorigenesis

The Hippo pathway controls organ size by regulating the processes of cell proliferation, apoptosis, differentiation and polarity (Zhao *et al.*, 2007; Cherrett *et al.*, 2012). Inhibition of the core components in Hippo pathway has been shown to cause organ overgrowth in many animal models. Activation of Yki,

the *Drosophila* homolog of YAP, can dramatically enlarge the fly eyes, head as well as the eye imaginal discs (Dong *et al.*, 2007; Kango-Singh *et al.*, 2009). YAP overexpression specifically in mice liver using the ApoE promoter and Tet-on (Doxycycline-inducible) system led to a 4-fold increase in liver mass within 4 weeks (Dong *et al.*, 2007). Surprisingly, this 4-fold increase in size was reversible when Doxycycline was removed from the drinking water. The liver returned to normal size after around 2 weeks (Dong *et al.*, 2007). Depletion of other core Hippo pathway proteins MST1/2 and Sav1 in mouse livers, similar results were observed, as the negative regulators of YAP are no longer present (Zhou *et al.*, 2009; Lu *et al.*, 2010; Song *et al.*, 2010). Mouse Sav1, Mst1/2 or Lats2 mutants also exhibited an enlarged heart phenotype due to hyperproliferation of cardiomyocytes and thickened ventricular walls (Heallen *et al.*, 2011).

When the Hippo signalling pathway is affected, it can cause cancer. Constitutive overexpression of YAP in mice using the Tet-on system mentioned above caused tumorous nodules in only 8 weeks, followed by severe hepatocellular carcinoma after 12 weeks of overexpression (Dong *et al.*, 2007). YAP activates the transcription of target genes in nucleus by binding to the transcription factors. The TEAD family transcription factors (TEADs) have been identified as the most potently activated targets of YAP (Zhao *et al.*, 2008). Inhibition of TEADs or disturbance of YAP-TEAD interaction affects the activation of most YAP-targeted genes and largely decreases the activity of YAP in accelerating cell proliferation, oncogenic transformation, and epithelial- mesenchymal transition (EMT, Zhao *et al.*, 2008). EMT is an important process during development when cells lose epithelial character and cell-cell adhesion, and increase motility (Macara *et al.*, 2014). This process is down regulated in cancer when metastasis occurs. Enhanced YAP expression and nuclear localisation have been reported in various human cancers, including liver cancers, lung cancers, colon cancers, ovarian cancers, and prostate cancers (Dong *et al.*, 2007; Zhao *et al.*, 2007). Finally, mutations of other Hippo pathway components, including NF2, LATS1/2, MST1/2, WW45, MOB, and KIBRA, have been observed in various human cancers including breast cancer; ovarian carcinoma; colorectal cancer;

soft tissue sarcoma; melanoma; retinoblastoma; astrocytoma; and neurofibromatosis type 2 (Pan, 2010; Zhao *et al.*, 2010a; Bao *et al.*, 2011; Hill *et al.*, 2011)

1.4 Medaka (*Oryzias latipes*) as a model organism

Medaka, *Oryzias latipes*, a small egg-laying Asian-originated freshwater fish, has been studied over a century and has now been used extensively as an animal model for several decades (Wittbrodt *et al.*, 2002). Medaka has the following advantageous features for the study of embryology, genetics and ecotoxicology. Medaka fish can tolerate a varying range of salinity and temperatures (6°C to 40°C, Takeda & Shimada, 2010). It's easy to breed and maintain in the laboratory environment with robust reproduction, rapid development, short life cycle and highly resistant to common fish diseases (Wittbrodt *et al.*, 2002). The embryos of medaka are fertilised and develop externally and both the embryo and chorion are transparent which make it possible to visualise embryogenesis (Takeda & Shimada, 2010; Fig.1.3). Sexual dimorphism can be easily distinguished by the shape of the dorsal fin. One pair of fish can spawn about 30 to 50 eggs daily under 12/12 light cycles in the lab. Early embryos can be kept at low temperature (4°C) to slow down embryo development, which provide researcher with longer time for microinjection, transplantation etc. (Shima & Mitani, 2004).

Although the biological features of medaka are mostly shared with zebrafish (*Danio rerio*), another common model organism, Medaka has some distinct features as compared to zebrafish. First, the medaka genome is much smaller (800 Mb) than the zebrafish genome, and it is only one-third the size of the human genome (Takeda & Shimada, 2010). Second is the availability of highly polymorphic inbred strains in medaka. Third, medaka is particularly useful for sex-determination studies, as the sex-determining mechanism is not known in zebrafish. Finally, unlike zebrafish, which are tropical, medaka can withstand a wider range of temperature.

The published sequenced genome (Kasahara *et al.*, 2007), relative ease of producing transgenic lines (Tanaka *et al.*, 2001), alongside with already

identified many mutant phenotypes (Furutani-Seiki *et al.*, 2004) make medaka ever more useful as a model organism for areas such as carcinogenesis research (Law, 2001) as well as regeneration studies (e.g. Katogi *et al.*, 2004). Furthermore, it can faithfully model human disorders such as polycystic kidney disease (Mochizuki *et al.*, 2005) or malignant melanoma (Schartl *et al.*, 2010). The normal development of medaka has been staged and reported with detailed descriptions from early embryogenesis to adulthood (Iwamatsu, 2004). The stages of developing medaka embryos mentioned in this work has been summarised in Table 1.1.

The medaka *hirame* (*hir*) mutant, identified from the large-scale mutagenesis screen (Furutani-Seiki *et al.*, 2004), has a pronounced flattened body. Major organs such as brain, eye, neural tube and somites are found collapsed (see Chapter 3). This mutant can therefore serve as a useful tool for the study of how 3 dimensional (3D) tissues and organs are generated and how they align to give rise to the global body shape.

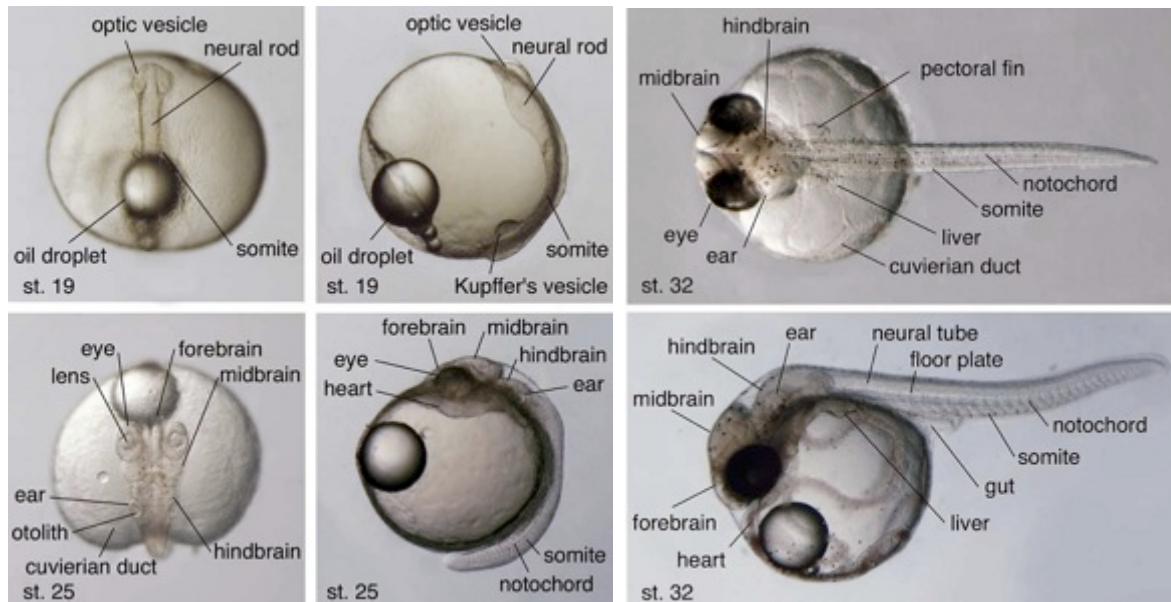


Figure 1.3 Images of live medaka embryos at st.19 (27.5 hpf), 25 (50 hpf) and 32 (101 hpf). Visible structures in live embryos are labelled. Dorsal views of left two and top right images. Lateral view of middle two and bottom right images. Anterior is to the top for the left two and middle two images; anterior is to the left for the right two images. Adapted from Furutani-Seiki *et al.*, (2004).

Developmental stage Hours	Hours post-fertilisation (hpf)
2 (1-cell)	0.5-1
10 (Early blastula stage)	6.5
12 (Pre-early gastrula stage, 50%epiboly)	10.5
13 (Early gastrula stage, 25%epiboly)	13
14 (Pre-mid gastrula stage)	15
15 (Mid gastrula stage, 50%epiboly)	17.5
16 (Late gastrula stage, 75% epiboly)	21
17 (Early neurula stage)	25
18 (Late neurula stage)	26
19 (100% epiboly)	27.5
20 (Formation of eye vesicles)	31.5
21 (Brain and otic vesicle formation)	34
22 (Appearance of heart anlage)	38
23 (formation of tubular heart)	41
24 (start of heart beating)	44
25 (onset of blood circulation)	50
26	54
27	58
28 (Onset of retinal pigmentation)	64
32	101

Table 1.1 Summary of the common stages of medaka development cited in this work and the corresponding hours of development. All embryos were incubated at 26.5±1°C (Iwamatsu, 2004).

1.5 Aims of the project

Building up a 3D shaped organ is associated with coordinated growth and alignment of multiple tissues. Growth among organs also might have to be coordinated to build up an integrated entire body. For example, the eye is constructed from lens placode and retina epithelia that form apposing each other and undergoes coordinated invagination to correctly position the lens in the eye cup (Chauhan *et al.*, 2009) and the eyes are aligned properly in the head to attain proper vision. Although the mechanisms that assist the coordinated growth between different tissues start to be unraveled, the underlying molecular mechanisms remain largely unknown. Moreover, the presence of a key regulator that orchestrates the complex processes for building 3D body shape has not previously been suspected.

A genome-wide phenotype-driven screen in medaka fish identified the *hirame* (*hir*) mutant (Furutani-Seiki *et al.*, 2004), which exhibited a unique flattened phenotype where tissues and organs collapsed and misaligned. Positional cloning identified that Yes-associated protein (YAP) is mutated in *hir* mutants (for details see Chapter 3.1.1). The aim of this study is to study the role of YAP for the generation of 3D tissues and their alignment to form organs that give rise to the global 3D body shape in vertebrates. This will firstly be done by a general morphological characterisation of the *hir* mutant (Chapter 3), followed by a more focused analysis of the sensory placodes, from which the sensory organs derived (Chapter 4). In the final result chapter (Chapter 5), possible molecular mechanisms underlying the unique *hir* phenotype will be investigated.

Chapter 2: Materials and Methods

2.1 Fish husbandry

The medaka fish strains used were grown and kept in the fish facility at the University of Bath under Home Office regulations. Breeding fish were kept at 23 (\pm 1) °C on a 12-h light/12-h dark cycle.

2.1.1 Medaka strains used

Medaka Wild-type (WT) strain Kyoto-Cab and the YAP mutant strain *hirame*^{54-20C} were used (Furutani-Seiki *et al.*, 2004). *hirame*^{54-20C} will be referred to *hir* from hereinafter. The following transgenic strains were generated in-house and also used: medaka *Tg(fli::EGFP)* and *Tg(cmlc2::EGFP)* that express EGFP in endothelial and cardiac progenitor cells respectively. Constructs used for generating the transgenic stains were provided by Weinstein Lab and Tsai Lab. Detailed procedures for making the two transgenic lines are described in previous publications (Lawson & Weinstein 2002; Huang *et al.*, 2003).

2.1.2 Incubation and staging of embryos

After being collected, sorted and cleaned, fertilised eggs were then incubated in 5cm Petri dishes (Sterilin Ltd., UK) containing embryo medium (NaCl 251.4 mM, KCl 8.5 mM, CaCl₂·2H₂O 16.5 mM, MgSO₄·7H₂O 16.5 mM) at the optimum temperature of 26 \pm 1 °C to enable development until the required stage. Embryos were staged according to medaka development staging tables (Iwamatsu, 2004).

2.2 Dechoriation of medaka embryos

Medaka embryos were gently rolled on a fine sandpaper (P2000 grit size, waterproof) to remove the hair on the surface of the chorion. Then a two-step treatment using a general protease and a hatching enzyme was required. Rolled embryos were incubated at 27 °C in Pronase (Calbiochem, USA) for 1 hour. After being washed with embryo medium for five times, embryos were incubated in hatching enzyme (an enzyme extracted from embryos during natural process of dechoriation, made as described in Porazinski *et al.*,

2011) at 27 °C for about 15 minutes up to 1.5 hours depending on the activity of the enzyme. Embryos were then transferred to sterile 1X Balanced salt solution (BSS, 130g NaCl, 8g KCl, 4g MgSO₄.7H₂O, 4g CaCl₂, and 10mg Phenol Red in 1L Milli Q Water; diluted 1:20 in Milli Q Water and pH adjusted to 7.4 by addition of 5% NaHCO₃ in Milli Q Water) using a glass Pasteur pipette when clear signs of disintegration of chorion were showed. Remaining chorions were manually removed by using micro-dissecting forceps (55 INOX A, DUMONT&FILS, Switzerland).

2.3 Microinjection of medaka embryos

mRNA, DNA or morpholino oligonucleotides were injected either at 1-cell (0.5 hpf) or 8-cell stage (approximately 2hpf) to deliver them to all cells or in a mosaic manner respectively (Fig.2.1). Injected embryos were incubated in embryo medium at 27°C until the required stage. Injection needles were made from borosilicate glass capillaries (GC100F-10, Clark electromedical instruments). The needles were pulled on a model PP-830 micropipette puller (Narishige scientific instrument lab, Japan). All injections were performed under a dissecting microscope (Leica MZ FL III) using a Microinjector 5242 apparatus (Eppendorf, Germany). The volume of one-shot of injection was 0.5 nl. For more details of microinjection, see Porazinski *et al.*, (2011) and Porazinski *et al.*, (2010).

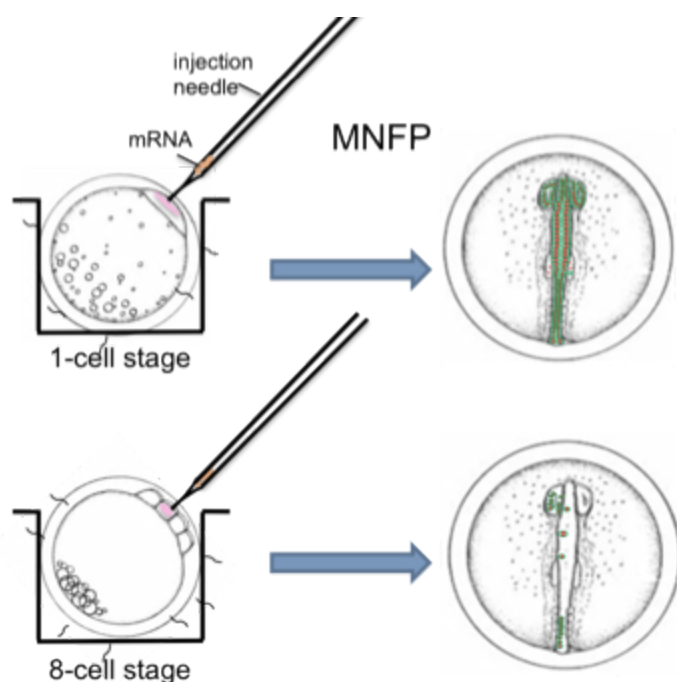


Figure 2.1 Schematic views of microinjection. 8-cell injection creates a mosaic of labeling cells in the embryo, which allows single cell tracing analysis. Drawings of embryos adapted from Iwamatsu (2004).

2.3.1 Morpholino oligonucleotide knockdown analysis in medaka

Morpholino oligonucleotide (MO) were synthesised by Gene Tools (USA) and were as follows:

MF YAP TB TGCGAACTCTTTGCGGCCCGAAAAC

MF YAP SB AGTGCTAGCCTGAGTTACAAAGAAG

MF TAZ TB CGCGTCCATGTGCGCCAGAAGTCAGA

MF TAZ SB AACCCAGAGGAAGACCTTACTTCAG

Control CCTCTTACCTCAGTTACAATTTATA

In medaka (MF above), two types of oligonucleotide, translation blocking (TB) and splicing blocking (SB) MOs were used to confirm the specificity of morpholino (MO) knockdown. Rescue of the phenotype by co-injecting corresponding mRNAs with the appropriate morpholino also confirmed the specificity of morpholino (MO) knockdown. TB MOs injection, SB MOs injection and MOs co-injection with *YAP* mRNA were all performed at early 1-cell (0.5 hpf) stage. 250pg YAP MOs was injected into WT embryos.

2.3.2 Phenotypic rescue experiments

Embryos from *hir*^{+/-} heterozygote crosses with Tg(*fli*::EGFP) or Tg(*cmcl2*::EGFP) were used for precise evaluation of rescue. mRNA of normal YAP and its variants were injected into *hir* mutants at 1-cell (0.5 hpf) stage. The *hir* phenotype rescue was judged via brain thickness, heart migration and Cuvier's duct formation. mRNAs were synthesised using SP6 mMACHINE Kit (Ambion, USA)

2.3.3 70kDaFN mRNA injection experiments

mRNA encoding N-terminal 70kDa fragments of medaka FN (FN 70kD), which act in a dominant negative manner to block FN assembly was injected into WT embryos at 1-cell stage (1 hpf). 70kDa N-terminal medaka FN1a+1b mRNA (250 pg) was injected into WT embryos. N-terminal 70kDa fragments of medaka FN1a and 1b was generated by PCR using KOD polymerase.

They were cloned into pCS2+EGFP with flexible linker (FL) to make EGFP fusion proteins that allow quantification and distribution of proteins of interest. mRNAs were synthesised using SP6 mMACHINE Kit (Ambion, USA).

2.3.4 MNFP injection experiments

To analyse the sensory placodes formation at cellular level, filopodia protrusions as well as oriented cell division plane, embryos were injected with mRNA (100pg) encoding membrane-EGFP and H2B-RFP (nuclear red fluorescent protein) (EGFP-CAAX+H2B-RFP, herein termed MNFP; Kretzschmar & Watt 2012) to label cell membranes green and nuclei red. For sensory placode and filopodia analysis, embryos were injected with MNFP at 1-cell stage (1 hpf). Cells were labeled in a mosaic manner by MNFP mRNA injection at the 8-cell (approximately 2hpf) stage for the cell division analysis.

2.4 Genotyping of medaka embryos

As it is impossible to distinguish the *hir* mutants from WT embryos at early development stages (<st.15, 17.5 hpf), it was necessary to genotype the embryos to confirm they were *hir* mutant embryos. Embryos were transferred to PCR tubes containing 25µl of 17mg/ml Proteinase K (P8044: Sigma, USA; diluted 1:10 in Tris-EDTA) for 4 hours at 55°C and 10 minutes at 94°C. Embryo DNA underwent PCR with primers for WT (5'-3' sequence: GCAAAGCCCTGCTCCAGTT) and *hir* (5'-3' sequence: GCAAAGCCCTGCTCCAGTA) YAP sequences (initialization: 95°C for 2 minutes; denaturation: 95°C for 30 seconds; annealing: 60°C for 30 seconds; extension: 72°C for 30 seconds; repeated for 35 cycles; final elongation: 72°C for 5 minutes; using Taq polymerase, Fermentas). Post-PCR samples were run on a 0.9% agarose gel along with WT and *hir* DNA controls to genotype them.

2.5 Whole-mount *in situ* hybridisation in medaka embryos

For more details of Whole-mount *in situ* hybridisation in medaka embryos, see Porazinski *et al.*, (2011)

2.5.1 Fixation, dehydration and rehydration

Dechorionated embryos were fixed in 4% paraformaldehyde (PFA, Sigma, USA)/phosphate-buffered saline (PBS, OXOID, England) at 4°C for three days. 4% PFA/PBS stocks were made by dissolving 40g PFA in 1litre 1X PBS. 1X PBS was prepared by dissolving 10 PBS tablets (OXOID, England) in 1L distilled H₂O and sterilised by autoclaving. Fixed embryos were rinsed five times with 1X PBST (800ml of distilled H₂O, 8g of NaCl, 0.2g of KCl, 1.44g of Na₂HPO₄ and 0.24g of KH₂PO₄, topped up to 1L with additional distilled H₂O. pH adjusted to 7.4 and sterilised by autoclaving. 1ml of Tween-20 (Sigma, USA) added to give a concentration of 0.1%) for five minutes each, before dehydration in a graded methanol (Fisher Scientific, UK) series in PBST. Consecutive 5-minute washes were carried out in 25% MeOH/PBST, 50% MeOH/PBST, 80% MeOH/PBST and 100%MeOH. The embryos were then rehydrated by 5-minute incubation in 80% MeOH/PBST, 50% MeOH/PBST and 25% MeOH/PBST and two 5-minute washes in 1X PBST. All procedures were performed in 2ml Eppendorf tubes at room temperature (RT).

2.5.2 Proteinase K digestion

Rehydrated embryos were then permeabilized in Proteinase K (ProK, 10µg/ml diluted in 1X PBST, Sigma, USA) treatment at 37°C. The length of ProK treatment was optimized and the results of which are showed in Table 2.1. Two 5-minute 1X PBST washes were carried out at RT afterwards. The embryos were then refixed in 4%PFA/PBS at RT for 2 hours.

Developmental stage at fixation	Length of ProK treatment (mins)
10	5
16	5
18	5
19	10
20	10
21	10
22	15
23	15
24	20
25	20
26	20
28	25

Table 2.1 Proteinase K treatment time for embryos at different stages. Pro K treatment times were defined by optimization experiments, the results of which are

summarised here. Left column shows developmental stage at which embryos were fixed. Right column shows necessary incubation period in Pro K to sufficiently permeabilise embryos.

2.5.3 Prehybridisation and hybridisation

After five 5-minute washes in 1X PBST, refixed embryos were prehybridised for 2 hours in Hyb+ Buffer (50% formamide, 5X SSC, 0.1% Tween-20, 50mg/mL heparin and 5 mg/mL torula (yeast) RNA) at 66°C. Hybridisation then took place overnight (O/N) on a shaker at 66°C in hybridisation mix. Hybridisation mix comprised of either sense or antisense RNA probe in Hyb Buffer (various dilution of different probes, see Table 2.2 for details). RNA anti-sense and sense probes were generated by Dr. Furutani-Seiki.

After O/N hybridisation, the probe was recovered and kept at -20°C freezer for future reuse. Embryos were firstly washed for 10 minutes in 66% Hyb B/33% 2xSSC, followed by a 10-minute rinse in 33% Hyb B/33% 2xSSC/33% Milli Q Water and a 10-minute wash in 2x SSC. Thereupon two 30-minute washes in 0.1xSSC were carried out. All washes mentioned above were performed at 66°C. Embryos were then rinsed twice in 1X PBST for 5 minutes each at RT.

2.5.4 Blocking and antibody incubation

The DIG-labelled probes were immunologically detected using an anti-DIG coupled to alkaline phosphatase (AP) antiserum (Roche). Embryos were first incubated in blocking solution (49mL PBST, 1mL 2% sheep serum, 0.1g BSA and 10% sodium azide diluted to 0.02% final concentration in solution) for 1 hour at RT on a rotator, before O/N incubation with anti-DIG-AP antiserum (1:5000 diluted in blocking solution) at 4°C.

2.5.5 Staining reaction and clearing

After O/N incubation, anti-DIG-AP antiserum solution was recovered for future reuse and the embryos were rinsed ten times in 1X PBST on a rotator at RT over a total time of 5 hours. The embryos were then washed in fresh prepared Alkaline-phosphatase (AP) buffer (100 mM Tris-HCL pH 9.5, 50mM MgCl₂, 100mM, NaCL and 0.01% Tween-20) three times for 5 minutes each, before

being transferred into ceramic wells containing 0.5ml NBT/BCIP solution (4.5 μ L NBT (Boehringer Ingelheim, Germany 75mg/mL in 70% DMF/30% H₂O) and 3.5 μ L BCIP (Boehringer Ingelheim, Germany, 50mg/mL in 100% DMF) in 1 mL AP buffer). Staining reaction was monitored from time to time and stopped by removing NBT/BCIP solution and washing embryos twice in 1X PBST for 5 minutes each.

Optional clearing steps can be used to reduce background noise. Stained embryos were rinsed in a series of ethanol (Fisher Scientific, UK). They were washed in 15% EtOH/PBST for 10 minutes, followed by a 20 minute wash in 80% EtOH/PBST before being transferred to 100% EtOH at 4°C O/N. Embryos were successively rinsed with 80% EtOH/PBST and 15% EtOH/PBST for 5 minutes each, finishing by five 5-minute washes in PBST at RT the next day.

2.5.6 Imaging

Stained embryos were briefly rinsed twice in 1X PBS before being soaked in a graded series of glycerol (Sigma, USA) diluted in PBS (20%, 50%, 80% and 100%). The embryos were left in each solution until they had sunk to the bottom of the eppendorf tube before transferring to the next graded solution. All glycerol washes were performed on a shaker. After sinking to the bottom, embryos were transferred to glass slides containing 100% glycerol and imaged. All embryos were photographed using a Leica DFC 300FX digital camera attached to an Axioplan2 Zeiss compound microscope using Leica Application Suite software.

Alternatively, embryos were sectioned as described in 2.6.1 and 2.6.2. Once samples were collected on glass slides, they were mounted with 80% glycerol/PBS and sealed with cover slips using nail polish. Sections were also examined and imaged using a Leica DFC 300FX digital camera.

Anti-sense probe	original vector	dilution (in Hyr+ B)
<i>Cdh1</i>	pBSSKM MFcdh1	1:10
<i>Dlx3</i>	N/A (gift from Wittbrodt lab)	1:20
<i>δ-crystallin</i>	N/A (gift from Wittbrodt lab)	1:20
<i>Fn1a</i>	pBSSKM MFFN1a	1:20
<i>Fn1b</i>	pBSSKM MFFN1b	1:20
<i>Itg-β₁</i>	N/A (gift from Wittbrodt lab)	1:25
<i>MyoD</i>	N/A (gift from Wittbrodt lab)	1:20
<i>Ntl</i>	N/A (gift from Wittbrodt lab)	1:20
<i>Pax2</i>	N/A (gift from Wittbrodt lab)	1:10
<i>Papc8</i>	pBS2SKM MKpapc8cDNA	1:10
<i>Sox3</i>	pCS2+MFsox3	1:10
<i>Sox10</i>	pBSSKM MFsox10	1:20
<i>YAP</i>	MFYAP1cDNAwithRI+xba	1:20

Table 2.2 Optimised dilution of anti-sense probes used in WISH.

2.6 cDNA cloning and construction

Total RNAs were converted to cDNA using the RNA-PCR kit ver.3 (Takara Bio, Japan) followed by PCR using KOD plus polymerase (Toyobo, Japan). For mRNA production, PCR amplified full-length cDNAs (medaka *YAP*, *70KDaFN1a,b* and *Cdh1*) were cloned into pCS2+ for mRNA synthesis, partial cDNAs of *Sox3*, *papc8*, *sox10*, *Fn1a* and *Fn1b* were cloned into pBluescript II SK- for Digoxigenin (DIG) labelled riboprobe synthesis.

N-terminal 70kDa fragments of medaka FN1a and 1b were generated by PCR using KOD polymerase. They were cloned into pCS2+EGFP with flexible linker (FL) to make EGFP fusion proteins that allow quantification and distribution of proteins of interest. mRNAs were synthesised using SP6 mMACHINE Kit (Ambion, USA).

2.7 Whole-mount immunohistochemistry (IHC) of medaka embryos

Embryos were fixed in either 4% PFA, dent fixative (80% MeOH/20% DMSO) or 2% trichloroacetic acid (TCA) depending on the antibody to be used (see Table 2.3) in eppendorf tubes. After fixation, embryos were washed three

times with 1X PBST and permeabilised with 0.5% Triton X-100 in PBS for 1 hour at RT. After three 1X PBST washes, embryos were incubated in blocking solution (PBDT: 49ml PBST, 1ml 2% sheep serum, 0.1g BSA, 0.02% Sodium Azide) at RT for 2 hours. About 50µl primary antibody solution (diluted in PBDT, dilutions see Table 2.3) was added into each tube and tubes were placed on a rotator at 4°C O/N. Primary antibodies were recovered on the second day and kept at 4°C for future reuse. The secondary antibodies were added after three 1X PBST washes and the tubes were wrapped with foil and then placed on a rotator at 4°C O/N. For the purpose of F-actin (phalloidin) and nuclei (TO-PRO-3) staining, the blocking step can be omitted. After permeabilisation, phalloidin and TO-PRO-3 diluted in the blocking solution (see Table 2.3 for dilution details) was added into each tube. Then eppendorf tubes were kept in dark on a rotator at 4°C O/N. On the third day, embryos were washed three times with 1X PBST for 10 minutes each on a shaker at RT. Before imaging, embryos were refixed with 4% PFA/PBS at RT for 2 hours.

For the cell death assay, TdT-mediated dUTP-biotin nick end labelling (TUNEL) was performed. TUNEL staining is not only limited to the detection of apoptotic cells but can also be used to detect DNA damage associated with non-apoptotic events such as necrotic cell death (Gavrieli *et al.*, 1992). The Roche In Situ Cell Death Detection Kit (TMR red, Catalogue No. 12156792910) was used according to manufacturers guidelines. An appropriate volume of reaction mix was added to each tube (5-7µl per embryo). Tubes were then left on a shaker for O/N incubation in the dark at RT. Control embryos were subjected to the label mixture only (no TdT enzyme added to tube). After O/N incubation, the TUNEL mix was removed and embryos were washed five times with PBST for 5 minutes each wash. All washes were carried out in the dark. TUNEL staining was assessed using fluorescence microscopy before carrying out staining for cell proliferation.

For imaging, embryos were mounted in 1.5% ultra-low gelling temperature agarose (Type IV-A: sigma, USA) solution (in Milli Q Water) in a 3.5cm culture

chamber (Iwaki, Japan), using a Leica SP5 confocal microscope or a Leica MZ16 FA fluorescent microscope.

Use	Antibody	Name	Source	Dilution	Fixative		
					Dent	PFA	TCA
Basal	Integrin β 1	8C8	Rabbit	1:1	Poor	Poor	Good
Apical	aPKC	C-20	Rabbit	1:100	Good	Good	OK
	Pan-cadherin	C-1821	Mouse	1:500	OK	OK	Good
	ZO-1	T8-754	Mouse	1:1	Good	Poor	OK
Basement Membrane	Fibronectin	Sigma F3648	Rabbit	1:100	Poor	Poor	Good
Cell death	Caspase-3		Rabbit	1:100	Good	Good	Good
proliferation	anti-phosphohistoneH3	#06-570 Upstate	Rabbit	1:500	OK	Good	OK
Nuclei	Topro3	T3605 Invitrogen		1:500	Good	Good	Good
Cell shape	Phalloidin 546	A22283 Invitrogen		1:250	NA	Good	NA
	Phalloidin 488	A12379 Invitrogen		1:250	NA	Good	NA
2nd antibody	Alexa Fluor 488	Molecular Probes	rabbit/mouse	1:250	Good	Good	Good
	Alexa Fluor 546	Molecular Probes	rabbit/mouse	1:250	Good	Good	Good

Table 2.3 Antibodies used for immunofluorescence staining.

2.8 Cryosectioning and immunofluorescence staining of medaka embryos

2.8.1 Embedding and sectioning

A similar fixative method was used as described in Section 2.5. Fixed embryos were rinsed three times with 1X PBS at RT (10 minutes for each wash). Then they were soaked in 10% sucrose (Sigma, USA)/PBS with 0.02% azide on a rotator until they sank. Embryos were then transferred to 20% sucrose/PBS for 10 minutes, followed by immersion in 15% cold-water fish

gelatin (Sigma, USA) in 35% sucrose/PBS for half an hour and finally in 25% gelatin/ 35% sucrose/PBS for another half an hour.

Set the cryostat (CM1850, Leica) at -28°C before sectioning. One embryo at a time was embedded in one section mould filled with 25% gelatin and orientated appropriately using a pair of forceps. Then the mould was placed on dry ice for at least 30 minutes before being transferred into the cryostat for a further 30 minutes. The frozen gelatin (containing the sample) was removed from the mould and glued to a metal specimen disc using OCT embedding medium (Tissue-Tek, Japan) inside the Cryostat set to -28°C . The cryostat was set to make $25\mu\text{m}$ sections and the sections were collected on superfrosted glass slides (Matsunami Glass Ind., Japan). Slides were dried O/N in a fume hood.

2.8.2 Antibody staining

A pap pen (Grale, AU) was used to draw circles around sections on each slide. Sections of embryos were permeabilised by dipping in acetone (Sigma, USA) into a staining jar for 30 seconds and then rehydrated in 1XPBS for another 30 seconds. After removing the excess liquid, slides were placed in a moist slide chamber and a blocking solution (1% albumin from bovine serum (Sigma, USA), 5% sheep serum (Sigma, USA) and 1% Azide) was added to each slide (about $500\ \mu\text{l}$ per slide). The slides were incubated in the chamber for 1 hour at RT. The blocking solution was then removed and replaced with the primary antibody diluted in the blocking solution (about $50\ \mu\text{l}$ per slide, dilution is dependent on the antibody, see Table 2.3 for details). All slides were covered with parafilm and incubated for 2 hours at RT. No primary antibody was added to the control slides. After three 10-minute 1X PBS washes, slides were incubated with second antibodies (dilutions see Table 2.3 for details) for 1.5 hours at RT. Second antibody was removed, followed by three 10-minute 1X PBS washes. For the purpose of F-actin (phalloidin) and nuclei (TO-PRO-3) staining, the blocking step can be omitted. After permeabilisation, slides were covered in the phalloidin and TO-PRO-3 diluted in the blocking solution (see Table 2.3 for dilution details) for half an hour at RT. PBS washes were then carried out.

After PBS washes, slides were left air-dry briefly before a coverslip (thickness 1, scientific lab supplies) was added onto the slides using Vectashield mounting medium (Vectashield, Vector laboratories, UK). Transparent nail polish was applied to seal the coverslip. The specimens were imaged using a confocal microscope (Leica TSC SP5).

2.9 Time-lapse microscopy imaging of live embryos during morphogenesis

Dechorionated embryos were placed in 1.5 % ultra-low gelling temperature agarose (Type IV-A: Sigma, USA) solution (in sterile 1X BSS) and transferred to a 3.5cm culture chamber with a glass base (Iwaki, Japan). Embryos were oriented using a sterilized hair-loop while the solution was still molten. The chamber was then placed on ice for about 20 minutes to allow agarose solidification. A confocal scanning microscope (Leica TSC SP5) was used to observe and record the images. Z stacks were taken at 0.99 μ m intervals over ranges of 100-500 μ m (depending on the tissue being imaged) and the exposure and gain were adjusted according to each embryo. Time interval was set from 6 minutes to 10 minutes. Temperature was maintained around 27°C to enable normal development. Total observation time varied from 10 hours up to 38 hours according to each embryo.

2.10 Assessment of epiboly progression in medaka embryos

Dechorionated embryos were periodically imaged at each developmental stage from st.15-21 (17.5-34 hpf) using the Leica MZ16 FA fluorescence-dissecting microscope. By placing embryos in custom-made moulds, epiboly was calculated as a percentage by measuring the coverage of the margin of the deep cell (DC) over the underlying yolk. Embryos were kept at 27°C throughout this process to enable normal development.

2.11 Enveloping layer cell shape analysis during gastrulation

Medaka embryos were fixed in pre-warmed PFA to prevent contraction of the blastoderm (deep cells and epithelial enveloping layer, EVL) at st.16.5 (23 hpf). Fixed embryos were stained with Phalloidin (A22283, Invitrogen, USA) to

demarcate the filamentous actin (F-actin) located at the cortex of EVL cells. Imaging was performed using the confocal setup previously described. Length-width (LWR) analysis for EVL cells was performed by measuring the ratio of the longest to shortest axis for cells at and up to 8 cells back from the EVL-yolk syncytial layer (YSL) margin as previously described (Köppen *et al.*, 1996). For cells at the leading edge of the EVL margin, length was measured as the distance between the midpoint of the leading edge of the cell and the animal-most region of the cell. Cell width was measured as the distance between the midpoints of the lateral cell boundaries of a cell, perpendicular to the length axis. For cells back from the leading edge of the EVL, length was defined as the longest axis of the cell along the animal to vegetal axis. Width measurements were made in the same way as for cells at the leading edge. Measurements were performed using Amira.

2.12 Gravity experiments

During *hir* mutant embryogenesis, different orientations of body flattening were observed. In order to test whether collapse correlated with the direction of gravity, gravity experiment was designed and performed.

Dechorionated embryos were embedded in the agarose as described in Section 2.7 at stage 17-18. Embryos were orientated in three ways; left side down, perpendicular and right side down (as shown in the Fig.2.2). After overnight developing at 27 °C degree incubator, embryos were checked under the dissecting microscope and only those orientation unchanged embryos were then fixed in 4% PFA/PBS at around stage 24. Fixed embryos were processed as described in Section 2.6.

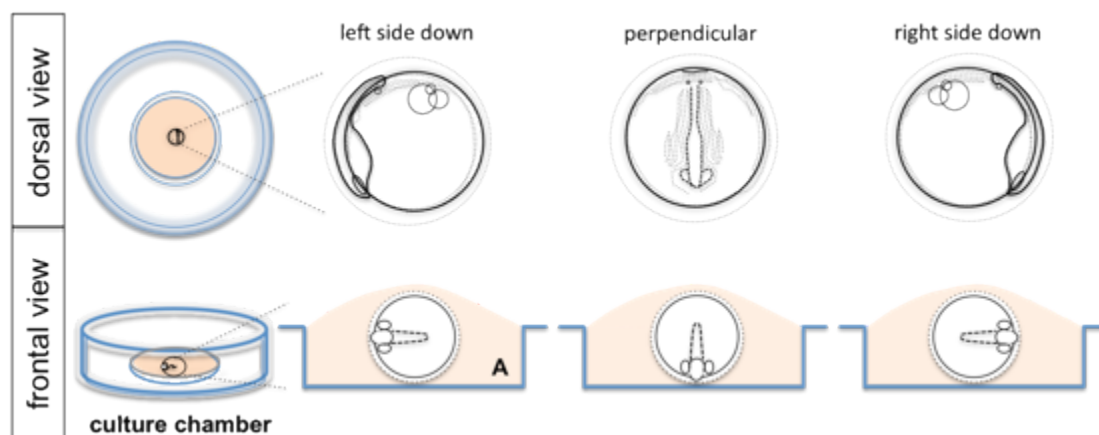


Figure 2.2 Schematic views of three embedding orientations. Dechorionated embryos were embedded in 1.5 % ultra-low gelling temperature agarose at stage17-18, and oriented in three positions. Top panel showing the dorsal view of the embedded embryos and bottom panel showing the frontal view. A, agarose.

2.13 Human 3D spheroid analysis

hTERT-RPE1 cells (American Type Culture Collection; CRL- 4000) were seeded in 6-well plates with a density of 2×10^5 cells per well. After each stealth RNA (100pmol) of Opti-Mem medium (Life Technologies, USA) was transfected using Lipofectamine RNAi Max (Life Technologies, USA), they were then incubated for 24h at 37°C. Trypsin treatment was employed to collect RNAi-transfected cells from 9 wells of 6-well plates. After being resuspended in 2 ml of 10% Fetal bovine serum (FBS; Hyclone, Thermo Fisher Scientific, USA)-DMEM, cells were seeded to 6 wells of a 12-well plate (Hydrocell, CellSeed Japan) and incubated for 48h at 37°C. Spheroids were fixed in 3% formalin and subjected to immunostaining. Reagents used for immunostaining: anti-FN (Sigma F3648, USA; 1:500), Alexa Fluor 546 Phalloidin (Invitrogen, A22283, USA; 1:200), TO-PRO-3 (T3605, Invitrogen, USA; 1:500). The list of primers is as below:

#1 Human YAP1 stealth RNA 5'-GCAACUCCAACCAGCAGCAACAGAU -3'

#2 Human YAP1 stealth RNA 5'-GGAAGGAGAUGGAAUGAACAUAGAA -3'

#1 Dog YAP1 stealth RNA 5'-UAUAUUUCUCCAUCCUGAGUCAUGG -3'

Negative control stealthRNA

2.14 Western blotting

Following dechoriation, embryos were transferred to 1.5ml Eppendorf tubes and rinsed with 1X PBS. After adding 1ml PBS, tubes were spun down at 3,000rpm for 2 minutes at 4°C followed by removal of supernatant. Repeat the PBS washing, spinning as well as the supernatant removal once. These steps are important as they remove the yolk so that lysis steps are not affected.

To perform lysis, 1X RIPA+ buffer (1ml RIPA- buffer (50mM Tris-HCl at pH 8, 150mM NaCl, 5mM EDTA, 15mM MgCl₂, 1% NP-40), 50µl 10% DOC, 1µl of 1M DTT, 1µl of 1.7mg/ml Aprotinin, 5µl of 200mM PMSF, 1µl of 100mM Na₃VO₄) containing 2mM Iodoacetic acid was added (about 1µl per embryo). Tubes were kept on ice for 10 minutes followed by spinning down at 4°C for 15 minutes at 12,500rpm. Supernatant was transferred to a new tube and 4X sample (16ml of 0.5M Tris-HCl at pH 6.8, 16ml glycerol, 3.2g SDS, 8ml β-mercaptoethanol, 32mg of bromophenol blue, made to 40ml volume with H₂O) buffer was added. Tubes were incubated at 100°C for 10 minutes and then cooled on ice. Samples were run on SDS-PAGE gels at 60V for half an hour followed by 1.5-2 hours at 130V allowing separation. Gels were then wet transferred to PVDF membranes for about 3 hours at 350mA. Membranes were gently rinsed with deionised water and incubated with 2% skim milk/TBS followed by multiple washes with deionised water. Primary antibodies diluted in 5% BSA/TBS/0.03% NaN₃ were added onto the membranes and then incubated overnight at 4°C. This was followed by five-time deionised water washes and secondary antibody incubation (in 2% skim milk/TBS) for 1-2 hours at RT. Fives 3-minute washes were performed with 0.2% TBST and twice with deionised water. Detection was carried out using the Western Chemilumi HRP kit (Femto).

Western blotting antibodies used were anti-Phospho-Ser19 MLC2 (3675, Cell Signaling) at a dilution of 1:100; anti-fibronectin pAb (F3648, Sigma Aldrich) with a dilution of 1:1000 (2% skim-milk), anti-YAP antibody (Cell Signalling #4912) diluted 1:500 and anti-GAPDH mAb (sc32233, Santa Cruz, 1:5000).

2.15 Quantitative RT–PCR analysis.

Total RNA was isolated from WT and *hir* mutant embryos at different developmental stages using TRIzol (Invitrogen, USA) according to the manufacturer's instructions. Superscript III reverse transcriptase (Invitrogen, USA) plus an oligo-dT primer were used to synthesize first-strand cDNA from 1mg total RNA. Each quantitative real-time RT–PCR was performed using the CFX96 real-time PCR detection system (Bio-Rad). For a 10ml PCR, cDNA template was mixed with the primers to final concentrations of 250nM and 5ml of SsoFast EvaGreen Supermix (Bio-Rad), respectively. The reaction was first incubated at 95 °C for 3.5min, followed by 45 cycles at 95 °C, 65°C and 72 °C for half a minute each.

2.16 Statistical analyses

Statistical significance between WT and mutant groups was tested using a Student's t-test (for two-way comparisons) or a one- way ANOVA (for multiple comparisons) with a Dunnett's T3 post-hoc test for two-way comparisons in SPSS 21. To test for differences in cell division angles between WT and *hir* embryos, the Kolmogorov-Smirnov (KS) test was performed. Available at: http://www.physics.csbsju.edu/stats/KStest.n.plot_form.html. Error bars on graphs show \pm standard error of the mean (S.E.M). P values of <0.05 were taken as statistically significant. All graphs were drawn in SPSS 21 or GraphPad Prism 5. Experiments were repeated for a minimum of three times with sufficient n numbers for each repeat to be confident that reported results are representative.

Chapter 3: General characterisation of medaka *hirame* (*hir*) mutant

3.1 Introduction

3.1.1 Identification of Medaka *hirame* (*hir*) mutant

Systematic phenotype-driven mutant screens involve random mutagenesis of the genome to generate mutants followed by screening for the phenotype of interest. The advantage of using mutagenesis is that it identifies the relatively small fraction of genes with unique and at least partially non-redundant functions (Haffter *et al.*, 1996), thus makes the phenotype-driven screen an unbiased approach to elucidate gene function (Porazinski *et al.*, 2011). Conversely, a gene-driven approach to remove the function of particular genes (i.e. knockout mutants) provides a complementary method. The value of phenotype-driven mutant screens is that they systematically analyse the biological processes into genetically defined steps (Porazinski *et al.*, 2011). Systematic mutant screens have been carried out in two teleost fish species, zebrafish (Haffter *et al.*, 1996) and medaka (Furutani-Seiki *et al.*, 2004). The zebrafish and medaka mutant screens were followed by a three-generation breeding to produce the homozygous F3 embryos. 2031 embryonic lethal mutations were identified, and 372 were selected for further analyses. Tissues affected by the mutations include forebrain, lateral line, liver, thymus, eye, somite and primordial germ cells. Remarkably, many mutations appear to be unique to Medaka (Furutani-Seiki *et al.*, 2004). One important mutant came out of this screen was *hirame* (*hir*) and it is under the classification where tissue organisation was affected (Furutani-Seiki *et al.*, 2004). This phenotype was not explicable by the current knowledge of vertebrate body pattern formation. The *hir* mutant has a different mechanism underlying the tissue defects.

The *hir* mutant embryos were extreme flattened due to the defect in hypoblast convergence and tissues dislocation including lens and heart (Watanabe *et al.*, 2004). The heart of the *hir* mutant was found beating next to the ears (Kitagawa *et al.*, 2004). Positional cloning identified a non-sense point mutation of ¹⁶⁴Leu (TTG to TAG) in the WW1 domain of Yes-associated protein (YAP) in *hir* mutants (Porazinski *et al.*, 2015; Fig.3.1).

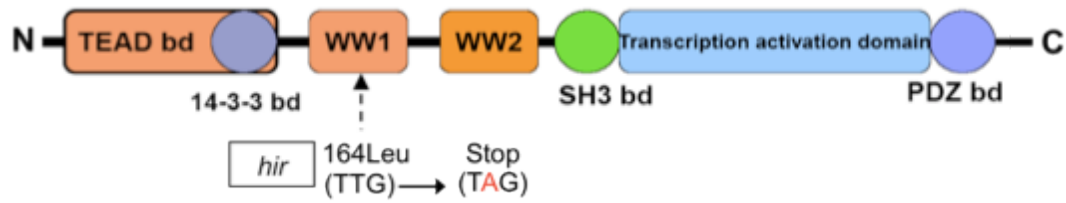


Figure 3.1 A non-sense mutation causes the *hir* phenotype. YAP cDNA encodes six protein binding domains/motifs and one transcription activation (TAC) domain. A non-sense mutation was found in the WW1 domain of YAP in *hir* mutants. Image adapted from Porazinski *et al.*, (2015)

The *hir* mutants display a remarkably flattened body (compare Fig.3.2 3 and 3'). Up to mid-neurulation at stage 21 (st.21), 34 hours post fertilisation (hpf); patterning of *hir* mutant embryos along the antero-posterior (A-P) and dorso-ventral (D- V) axes is normal. From st.21 (34 hpf), the body of the *hir* mutant embryos gradually becomes flattened (st.27, 58 hpf, Figure 3.2 3'). However, they survive until 6 days post fertilisation (6 dpf) when most of the organs have developed, thus allowing detailed analysis of organogenesis. The mutant got its name because of this pronounced body flattening, as in Japanese 'hirame' means flat fish.

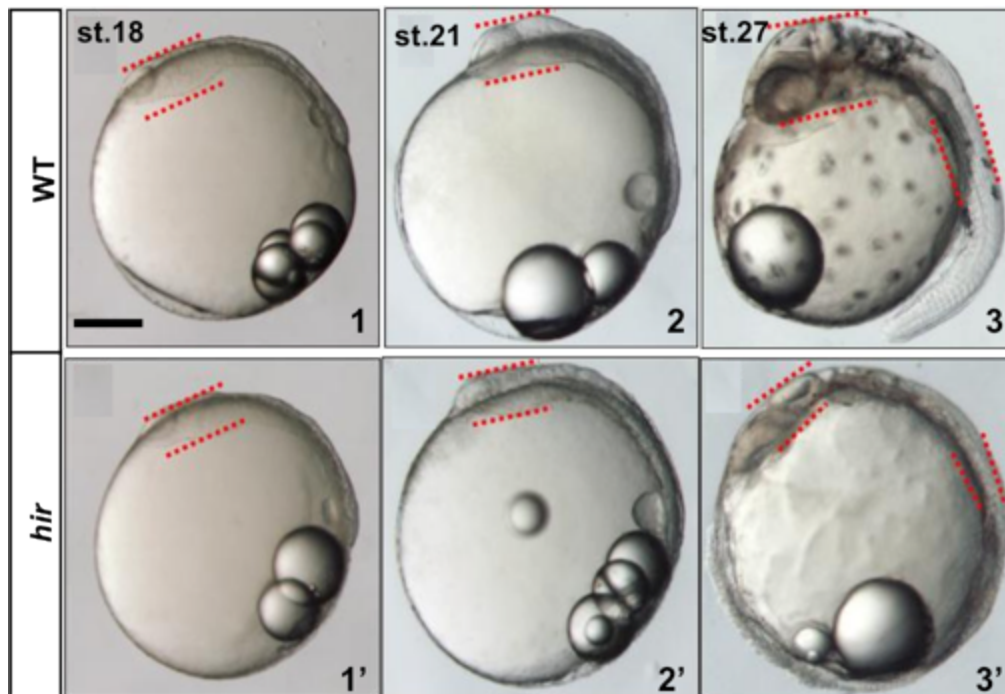


Figure 3.2 The flattened *hirame* phenotype. Lateral view of all images with anterior to the top. The *hir* mutants display a dramatically flattened body. Dotted lines indicate

the body thickness. Scale bar = 150µm. (Images were kindly provided by Dr. Makoto Furutani-Seiki.)

3.1.2 Role of YAP during embryogenesis

The functional variety of YAP has begun to be unraveled *in vivo*. In particular, there is a poverty of information regarding its function during early vertebrate development. Mice lacking YAP exhibit severe developmental defects that result in early lethality (Morin-Kensicki *et al.*, 2006).

YAP-null mouse embryos exhibited developmental malformations beginning at E7.5 with smaller embryo body and a profound separation between the hypoblast and the epiblast. Properly formed amnion and chorion were also found missing at this stage (Morin-Kensicki *et al.*, 2006). By E8.5, the YAP-null embryos demonstrated a much short and wider body axis with the improperly folded anterior epithelium, caudal dysgenesis and failure of chorioallantoic fusion (Morin-Kensicki *et al.*, 2006). E9.5 embryos exhibited defects in ventral closure and turning, a disorganised anterior neurepithelium, a bulbous allantois, and a ruffled yolk sac. These data suggest that YAP is required for the yolk sac vasculogenesis, chorioallantoic attachment, and embryonic axis elongation during development (Morin-Kensicki *et al.*, 2006).

Since YAP knockout mice failed to progress normally through early development, in part due to nutritional deficiencies, therefore other vertebrate model organisms which develop externally could better characterise the role of YAP during embryogenesis. Since YAP homologs have been found in zebrafish (*yap1*; Jiang *et al.*, 2009), and *Xenopus* (Gee *et al.*, 2011), loss-of-function study of YAP was therefore performed by various research groups. YAP morpholino (MO)-mediated loss-of-function in both *Xenopus* and zebrafish led to incomplete epiboly at gastrulation and impaired anterior-posterior (A-P) axis elongation (Gee *et al.*, 2011). Apart from defective A-P axis, YAP knockout zebrafish also demonstrated small heads with smaller eyes (Jiang *et al.*, 2009; Hu *et al.*, 2013; Loh *et al.*, 2014), severely delayed cardiogenesis and hematopoiesis, disrupted somitogenesis (Hu *et al.*, 2013), comprised neurogenesis, abnormal craniofacial development (Jiang *et al.*,

2009), and impaired lateral line system (Loh *et al.*, 2014). Reduction of YAP in zebrafish causes increased apoptosis as well as decreased proliferation (Jiang *et al.*, 2009; Hu *et al.*, 2013).

Recent studies have shown that YAP also plays a role in neuronal differentiation (Asaoka, *et al.*, 2014; Zhang *et al.*, 2012). Inhibition of YAP by RNA interference (RNAi) reduces proliferation and increases differentiation in postnatal mouse retina cells (Zhang *et al.*, 2012). It was later shown that YAP's TEAD-binding domain, two WW domains, and transcription activation domain contribute to normal retinal development during zebrafish retinogenesis (Asaoka, *et al.*, 2014).

3.1.3 Medaka epiboly

Epiboly is the first cell migration process that occurs from blastula to gastrula stages in fish (Iwamatsu, 2004). During epiboly, a number of dividing cells at the animal pole (blastodermal cells) migrate toward vegetal pole, expanding over the yolk sphere to cover the entire surface eventually. In medaka embryos, epiboly begins at st.12 (10.33 hpf). By st.13 (13 hpf), the early gastrula stage is reached; the blastoderm starts to expand with cells covering about 1/4 of the yolk sphere (Iwamatsu, 2004). At st.14 (15 hpf), epiboly proceeds further and blastoderm covers about 1/3 of the yolk sphere. The germ ring is well-defined and the embryonic shield advances in size. (Iwamatsu, 2004). The blastoderm at st.15 (17.5 hpf, mid gastrula stage) covers about half of the yolk sphere. When the blastoderm reaches two thirds of the yolk sphere (st.16, 21 hpf), the embryonic shield becomes narrow and the neural keel is more clearly visible (Iwamatsu, 2004). By the time the yolk sphere is nearly covered by the blastoderm (st.18, 26 hpf) excepting a small vegetal area, the embryonic shield develops to form the embryo (Iwamatsu, 2004). Complete blastopore closure is at st.19, when neurulation is complete and the embryo develops two somites (27.5 hpf, Iwamatsu, 2004). Medaka epiboly is summarised in Fig. 3.3.

3.1.4 Aims

The YAP mutant of medaka fish, *hirame* (*hir*), was identified in a genome-wide screen looking for mutations affecting organogenesis in medaka (Furutani-Seiki *et al.*, 2004). It exhibits defective hypoblast convergence and dislocated tissues including lens and heart (Watanabe *et al.*, 2004), however, a more detail analysis underlying *hir* phenotype is needed to provide more insight into how YAP functions during embryogenesis.

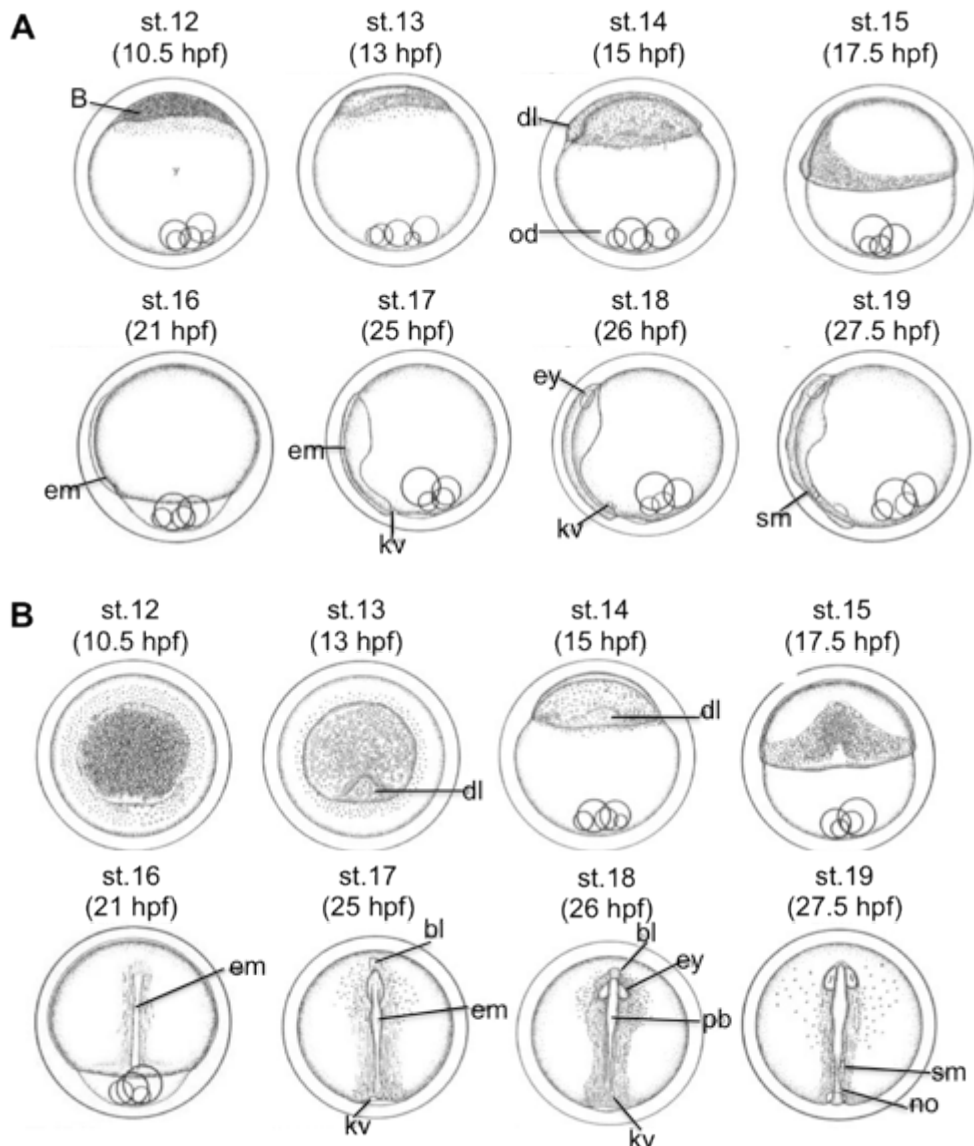


Figure 3.3. Schematic of gastrulation in medaka. A, Lateral views of the embryo during gastrulation depicting how the blastoderm spreads over the yolk. **B,** Animal pole views (st.12-13) followed by dorsal views of developing medaka embryos. B, blastoderm; dl, dorsal lip; em, embryo; ey, optic (eye) vesicle; kv, Kupffer's vesicle; no, notochord; od, oil droplets; pb, protobrain; sm, somite; Adapted from Iwamatsu (2004).

3.2 Results

3.2.1 Yes-associated protein (YAP) is mutated in *hirame* mutants

Positional cloning identified a non-sense point mutation of ¹⁶⁴Leu (TTG to TAG) in the WW1 domain of Yes-associated protein (YAP) in *hir* mutants (Porazinski *et al.*, 2015). A detailed spatio-temporal expression of *YAP* gene in both WT embryos and *hir* mutants was first analysed at a series of stages: st.10 (6.5 hpf, early blastula stage, about 1000 cells), st.18 (26 hpf, late neurula stage), st.20 (31.5 hpf), st.22 (38 hpf), st.24 (44 hpf) and st.26 (54 hpf).

In situ hybridisation analysis showed that *YAP* mRNA expression in WT embryos was ubiquitous, but dynamic throughout development (Fig. 3.4 A, 1-6). However, from st.20 (31.5 hpf) onwards, the expression of *YAP* in *hir* mutants was significantly reduced (Fig. 3.4 A, 3'-6'). And this correlated with the results from RT-PCR analysis of *YAP* mRNA (Fig. 3.4 B). *YAP* transcripts were also ubiquitously presented in WT embryos throughout all the developmental stages examined. As it is impossible to tell the difference between WT and *hir* embryos at early developmental stages (<st.15, 17.5 hpf), genotyping of all individual embryos at st.10 was carried out before RT-PCR analysis. A clear band was present at st.10 (6.5 hpf) in *hir* mutants presumably because of the presence of maternal *YAP* mRNA, but was strongly reduced after st.20 (31.5 hpf) when zygotic gene expression onset (Fig. 3.4 B).

In situ hybridisation of *YAP* was observed simultaneously with the development of many tissues/organs, including brain, eyes, branchial arches, ear and notochord in WT embryos (Fig. 3.4 A, 1-6), whereas in *hir* mutants, this expression fashion was not observed (Fig. 3.4 A, 4'-6').

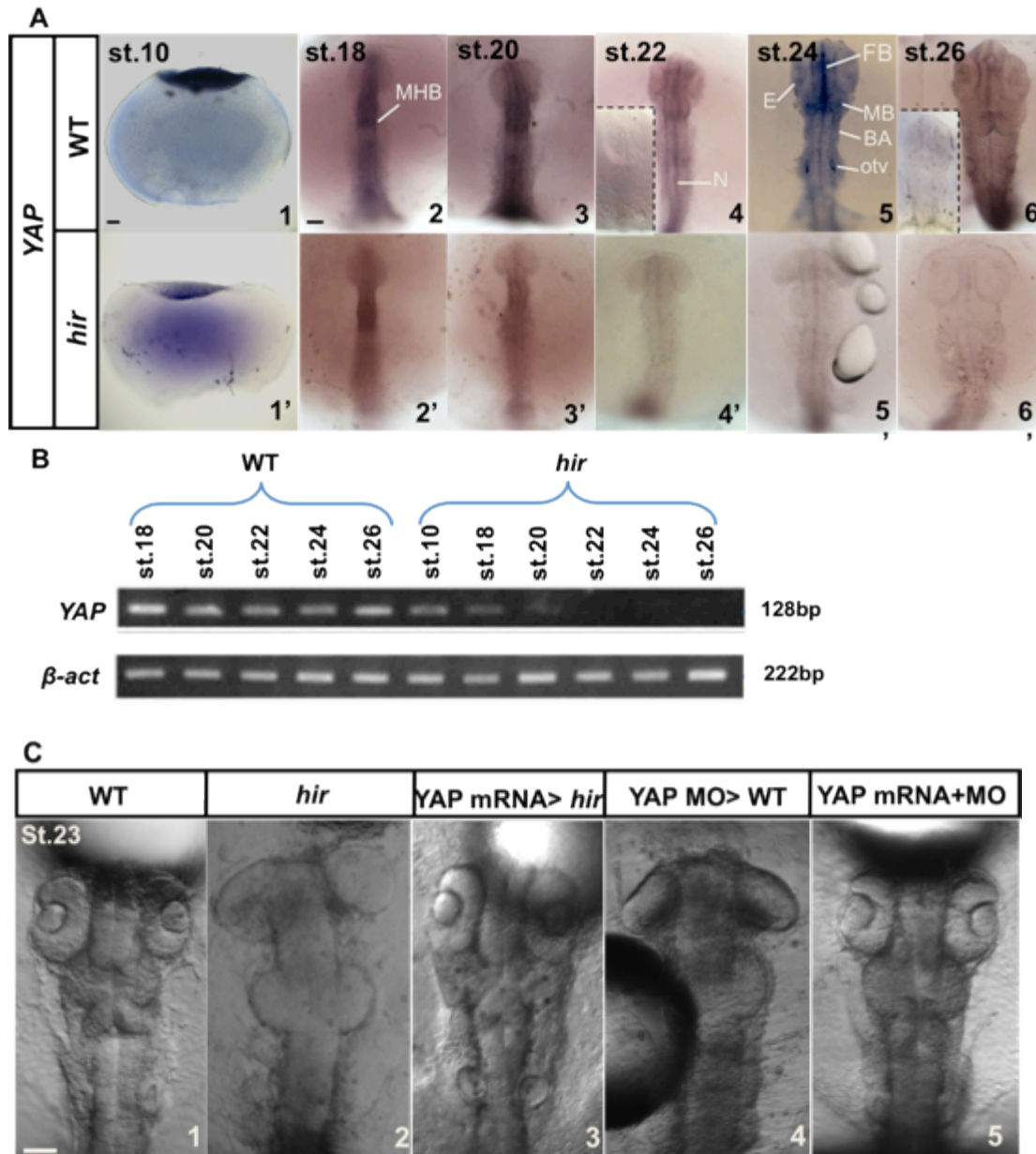


Figure 3.4 YAP is mutated in *hirame* mutant. Stages are indicated top left. **A**, Spatio-temporal expression pattern of *YAP* during medaka embryogenesis. 1-6, 1'-6' Dorsal views. Inserts in 4 & 6 are two examples of *YAP* sense probe stained WT embryos at st.22 (38 hpf) and st.26 (54 hpf) respectively as a control. **B**, RT-PCR analysis of *YAP* mRNA during embryogenesis. β -actin as control. **C**, 1-5 Dorsal view. 1, WT embryo; 2, *hir* mutant; 3, *hir* mutant injected with normal *YAP* mRNA, 4, *YAP* MO knock-down in WT embryo; 5, co-injection of *YAP* MO with *YAP* mRNA into WT. A, anterior; BA, branchial arches; E, eye; FB, forebrain; MB, midbrain; MHB, midbrain hindbrain boundary; N, notochord; otv, otic vesicle; P, posterior. Scale bar = 40 μ m. Panel B in collaboration with Shoji Hata. Panels D and E in collaboration with Sean Porzinski.

In order to confirm the relation between YAP mutation and the *hir* phenotype, two independent approaches were carried out: 1) injection of YAP morpholino oligonucleotide (MO) into WT embryos mimicked the *hir* phenotype (Fig. 3.4 C, 4); and 2) ubiquitous expression of *YAP* mRNA in *hir* mutants rescued the phenotype (Fig. 3.4 C, 3). YAP MO injected WT embryos were rescued by co-injection of YAP mRNA (Fig. 3.4 C, 5).

Two types of oligonucleotide, translation blocking (TB) and splicing blocking (SB) MOs were used to confirm the specificity of *YAP* MO knockdown. The phenotype was judged by brain thickness and heart migration. Injected embryos were checked at st.25 (50 hpf) for a flattened body and heart dislocation as summarised in Table 3.1. Both *YAP* TB MO and *YAP* SB MO injection caused the *hir*-like phenotype (flattened body and dislocated heart). Higher doses of the two MOs was more efficient at knocking down *YAP* mRNA. *YAP* TB MO worked better compared to *YAP* SB MO.

Morpholino	Host	Amount of MOs (ng)	Total survived	Normal (%)	Flat body (%)	Heart dislocation (%)
YAP TB MO	WT	4	34	0	91	85
	WT	2	43	28	53	42
YAP SB MO	WT	5	36	11	89	0
	WT	2.5	39	64	36	0
Control MO	WT	5	28	100	0	0

Table 3.1 Phenotype of medaka YAP MO injected embryos. Injected embryos were examined at st.25 (50 hpf) for a flattened body and heart dislocation.

3.2.2 *hirame* mutants exhibit a slow epiboly phenotype

The *hir* mutant has early and late phenotypes depending on the tissue/organ examined. The earliest *hir* phenotype that can be identified is slow epiboly (Fig. 3.5 A, B), as *hir* demonstrates defective hypoblast convergence (Watanabe *et al.*, 2004) and significantly delayed blastopore closure. Epiboly therefore was examined between WT embryos and *hir* mutants during gastrulation. In this set of experiment, live images were taken at multiple time points during development, and whole-mount *in situ* hybridization of dorsal markers no tail (*ntl*) was also performed, as it labels the blastoderm margin.

Four different groups of embryos were examined: 1) WT; 2) *hir* mutants; 3) maternal YAP KD *hir* mutants (mYAP KD *hir*) generated by TB MO-injection into *hir* embryos causing an even more severe epiboly phenotype; and 4) YAP mRNA injected *hir* embryos, to demonstrate that injection of YAP mRNA into *hir* mutants can rescue the phenotype.

At st.15 (17.5 hpf), all reached the 60%-epiboly stage, except mYAP KD *hir* embryos, which developed to about 53%-epiboly stage. At st.16 (21 hpf), WT and YAP mRNA injected *hir* embryos reached almost 80% epiboly, while *hir* mutants were at 76% epiboly and mYAP KD *hir* mutants were even slower, and had just reached 63%-epiboly stage. At st.19 (27.5 hpf), WT and YAP mRNA injected *hir* embryos had already completed epiboly. The *hir* mutants, however, were at 95%-epiboly stage and mYAP KD *hir* mutants only reached 81%-epiboly stage, and the blastopore closure was severely delayed (Fig. 3.5 C).

During gastrulation, WT embryos as well as YAP mRNA injected *hir* embryos completed epiboly by st.19 (27.5 hpf). However, it took quite some time for both *hir* and mYAP KD *hir* mutants to finish this process, suggesting impaired epiboly during gastrulation.

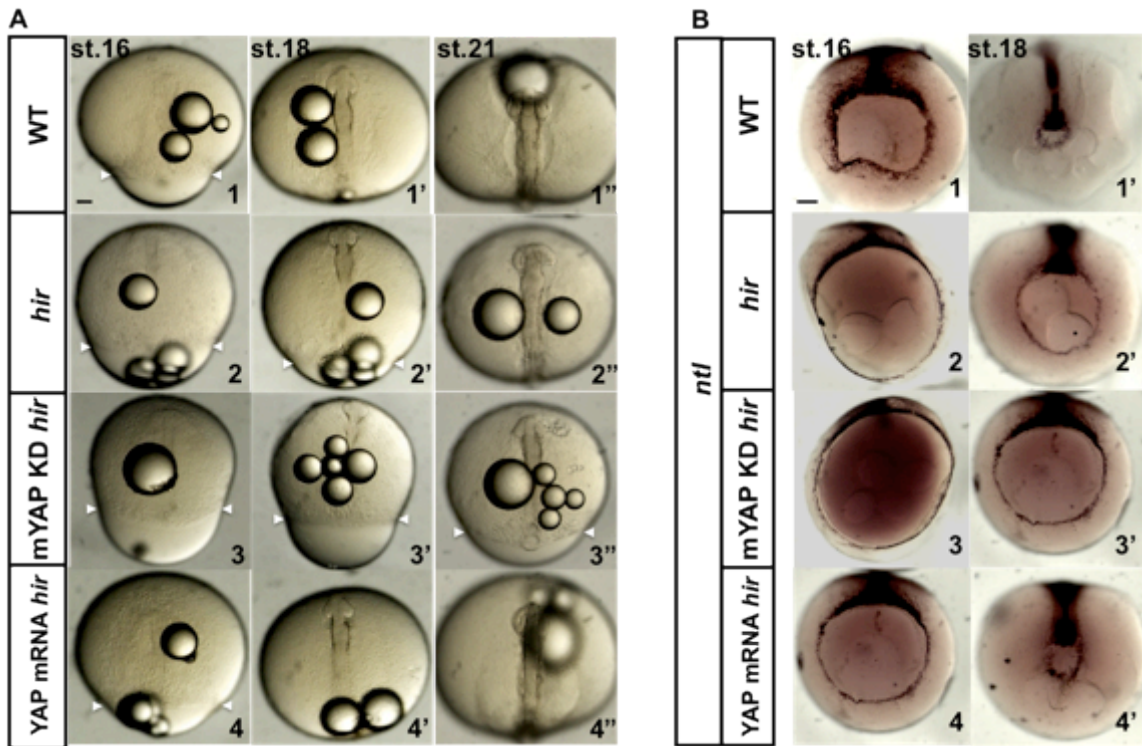


Figure 3.5 *hirame* mutants exhibit slow epiboly. Stages are indicated top left. **A**, 1-4, 1'-4', 1''-4'', dorsal views of live WT embryos, *hir* mutants, mYAP KD *hir* embryos and YAP mRNA injected *hir* embryos. White arrowheads indicate the blastoderm margin. **B**, Whole-mount *in situ* hybridization of *ntl* at st.16 and st.18. (1-4,1'-4') Vegetal view. Scale bars = 50 μ m. Epiboly quantified (%) in **C**.

At st.15 (17.5 hpf), WT= $59 \pm 3.34\%$ (n=16), *hir* = $59 \pm 4\%$ (n=14), mYAP KD *hir* = $53 \pm 3.45\%$ (n=12), YAP mRNA *hir* = $62 \pm 3.61\%$ (n=17).

At st.16 (21 hpf), WT= $80 \pm 4.47\%$ (n=38), *hir* = $76 \pm 4.99\%$ (n=25), mYAP KD *hir* = $63 \pm 4.8\%$ (n=25), YAP mRNA *hir* = $78 \pm 4.5\%$ (n=39).

At st.17 (25 hpf), WT= $94 \pm 2.84\%$ (n=32), *hir* = $84 \pm 4.46\%$ (n=25), mYAP KD *hir* = $72 \pm 5.21\%$ (n=24), YAP mRNA *hir* = $96 \pm 2.45\%$ (n=22).

At st.18 (26 hpf), WT= $98 \pm 2.17\%$ (n=32), *hir* = $90 \pm 5.11\%$ (n=17), mYAP KD *hir* = $76 \pm 4.79\%$ (n=24), YAP mRNA *hir* = $98 \pm 1.33\%$ (n=22).

At st.19 (27.5 hpf), WT= $100 \pm 0.69\%$ (n=38), *hir* = $95 \pm 3.96\%$ (n=25), mYAP KD *hir* = $81 \pm 5.31\%$ (n=25), YAP mRNA *hir* = $99 \pm 0.88\%$ (n=39).

At st.20 (31.5 hpf), WT= 100% (n=38), *hir* = $98 \pm 2.64\%$ (n=7), mYAP KD *hir* = $86 \pm 5\%$ (n=22), YAP mRNA *hir* = 100% (n=39).

At st.21 (34 hpf), WT= 100% (n=38), *hir* = 100% (n=25), mYAP KD *hir* = $97 \pm 4.23\%$ (n=20), YAP mRNA *hir* = 100% (n=39).

* = highly significant difference between WT and *hir* means, i.e. $P \leq 0.001$, t-test.

** = highly significant difference between WT and mYAP KD *hir* means, i.e. $P \leq 0.0005$, t-test.

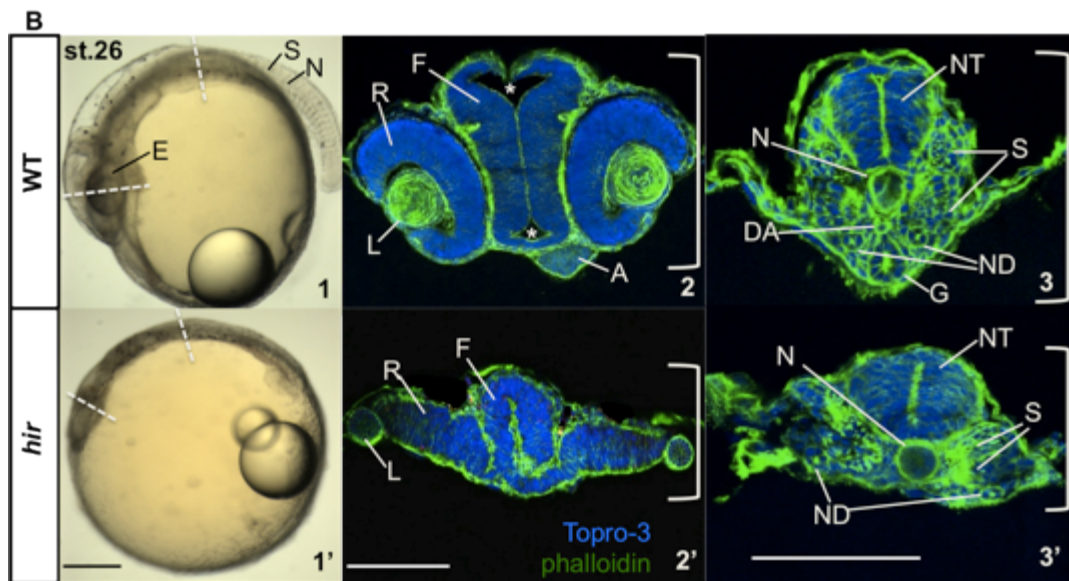
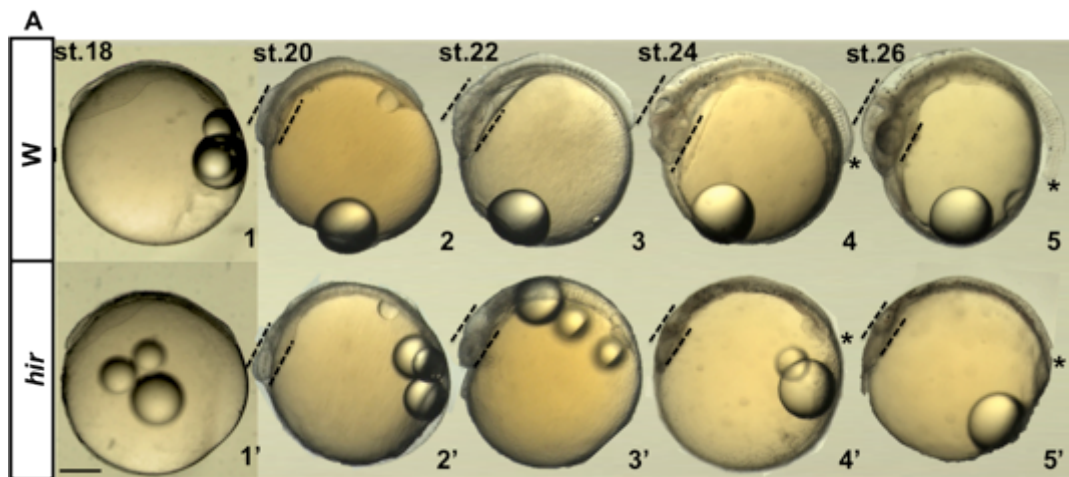
3.2.3 Organs/tissues are found collapsed and misaligned in *hirame* mutants

The most striking later phenotype of *hir* mutant is a pronounced flattened body (Fig. 3.6 A, B). During medaka embryogenesis, the thickness of WT embryo body increased, especially in the brain region (Fig. 3.6 A, 1-5), whereas this growth trend ceased in *hir* embryo at st.22 (38 hpf, Fig.3.6 A, 3'). Instead of gaining thickness, the *hir* embryo body became even thinner in the later developmental stages (Fig. 3.6 A, 4', 5'). From st.24 (44 hpf) onwards, *hir* mutant also displayed a notable shortened body axis (Fig. 3.6 A, 4-5, 4'-5').

Histological analysis revealed that major tissues/organs, including brain, retina, neural tube, and somites were flattened in *hir* mutant, and were therefore, not properly aligned. The strongest alteration was observed in the forebrain region. While the lens invaginated into the retina in WT embryos, the lenses were found dislocated in *hir* mutants (Fig. 3.6 B, 2'). Lumen formation in forebrain was also impaired compared to WT embryo (Fig. 3.6 B, 2, 2').

Some structures such as dorsal aorta and gut were also missing in the mutant (Fig. 3.6 B, 3, 3').

The two transgenic lines, *fli::EGFP* (Fig.3.6 C, 2, 2') and *cmhc2::EGFP* (Fig.3.6 C, 3, 3'), showed that the heart primordia and Cuvierian ducts (CDs) were not formed properly in *hir* mutants. While the heart formed beneath the forebrain in WT embryo at st.26 (54 hpf), cardia bifida, whereby cardiac progenitors fail to migrate and fuse at the midline, were observed in the *hir* mutant (Fig.3.6 C, 3, 3'). The main blood vessel, Cuvier's duct was fully formed in WT embryos by st.26 (54 hpf), circulating blood from the heart to the body, however the CD remained truncated in the *hir* mutant (Fig.3.6 C, 2, 2').



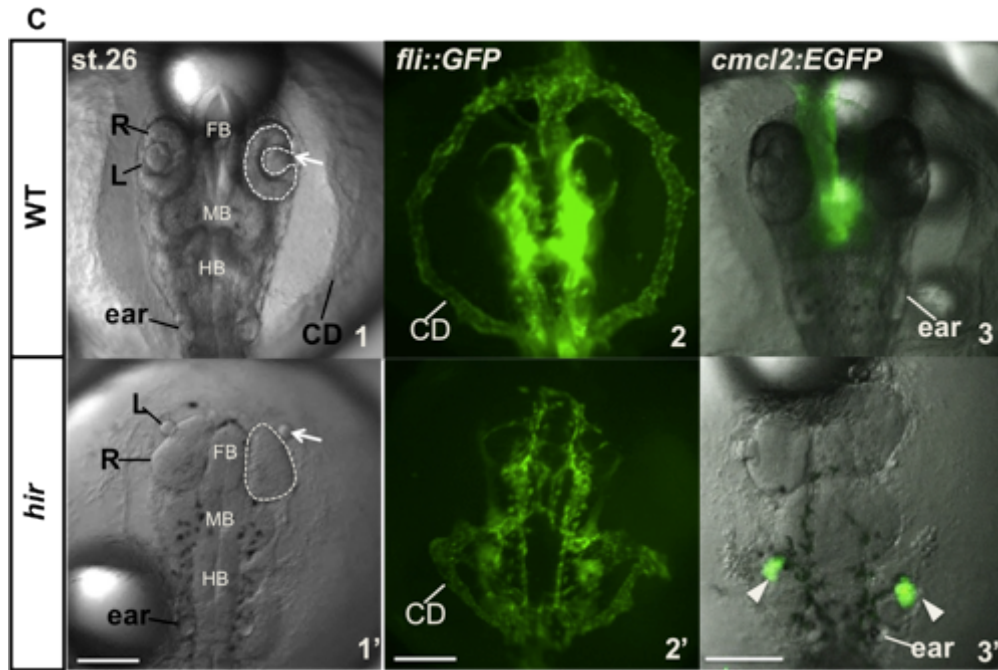


Figure 3.6 Organ collapse and misalignment in *hirame* mutants. Stages are indicated top left. **A**, 1-5,1'-5', Lateral views of live WT embryos and *hir* mutants from st.18 (26 hpf) to st.26 (54 hpf). Black dashed lines indicate the thickness of brain. Asterisks indicate the tips of the tails. **B**, Transverse sections at st.26 (54 hpf) at the planes shown in 1, 1'. Embryos were fixed and stained with phalloidin (green, F-actin) and TO-PRO-3 (blue, nucleus). White Brackets highlight the thickness of the embryos. Asterisks indicate the lumens in WT forebrain. **C**, Dorsal views of live st.26 (54 hpf) *fli::EGFP* (2, 2') or *cmcl2::EGFP* (3, 3') transgenic embryos expressing EGFP in endothelial progenitor cells and heart, respectively. Truncated Cuvier's duct (2') and unfused heart primordia next to the ear (3' arrowheads) in *hir* mutants. Retinas encircled by white dash lines and arrows indicate the position of lenses. A, atrium; CD, Cuvier's duct; DA, dorsal aorta; E, eye; FB, forebrain; G, gut; HB, hindbrain; L, lens; MB, midbrain; N, notochord; ND, nephric duct; NT, neural tube; R, retina; S, somites. Scale bars= 100μm.

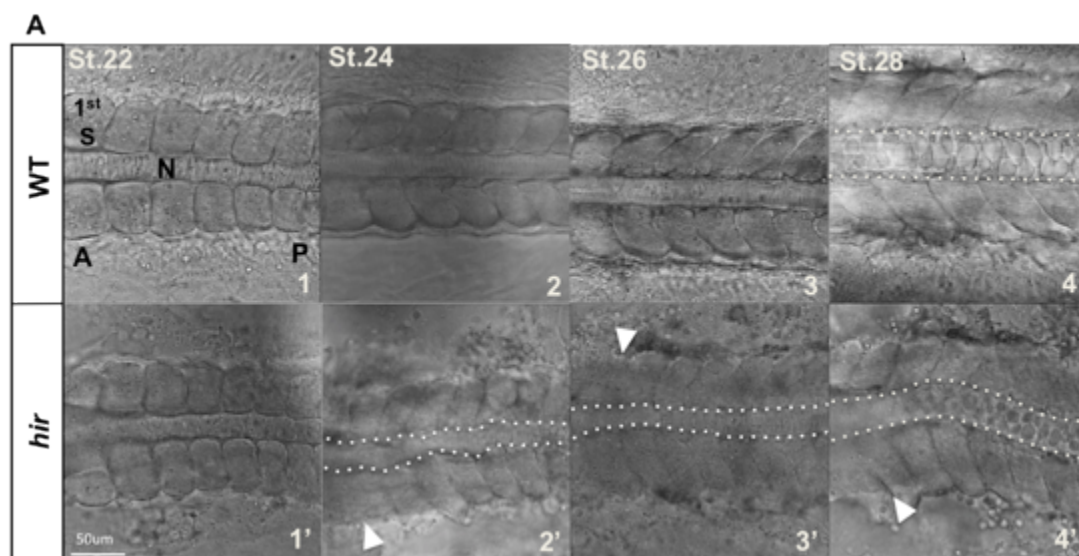
3.2.4 Somitogenesis is disturbed in *hirame* mutants.

In the *hir* mutant somites and notochord were also affected from st.24 (44 hpf) onwards. In WT embryos, the paired somites formed symmetrically along the notochord during morphogenesis (Fig. 3.7 A, 1-4). However, in *hir* mutants, despite the asymmetric somites, the notochord became curved (Fig. 3.7 A, 2'-4', dotted lines) and the segmental boundaries were less clear compared to WT embryos (Fig. 3.7 A, 2'-4' arrowheads).

Analysis of the periodic gene expression patterns of paraxial protocadherin (*papc*) and *myoD* in presomitic and somitic mesoderm by in situ hybridisation confirmed that anterior-posterior (A-P) patterning of embryonic axis formation was not affected in *hir* mutants.

Papc is a presomitic mesoderm (PSM) marker, from where somites derived. *In situ* hybridisation of *papc* revealed normal segmentation expression in the primordial somites in both WT and *hir* embryos, but the pattern was slightly disrupted in the mutants (Fig. 3.7 B, 1-3, 1'-3'). A broadened presomitic domain was presented in *hir* mutants (Fig. 3.7 B, 1'-3', red brackets).

Expression of *myoD* in lateral presomitic cells were normal in both WT and *hir* embryos from st.20 (31.5 hpf) to st.24 (44hpf, Fig. 3.7 B, 4-5, 4'-5'). From st.26 (54 hpf) onwards, striped expression of *myoD* was disrupted in the anterior part in *hir* mutants, but was segmental normally posteriorly (Fig. 3.7 B, 6', 6', arrowheads). Transverse sections of *myoD*-stained embryos showed gradually collapsing somites as well as the neural tubes (Fig. 3.7 C, 2-4, 2'-4').



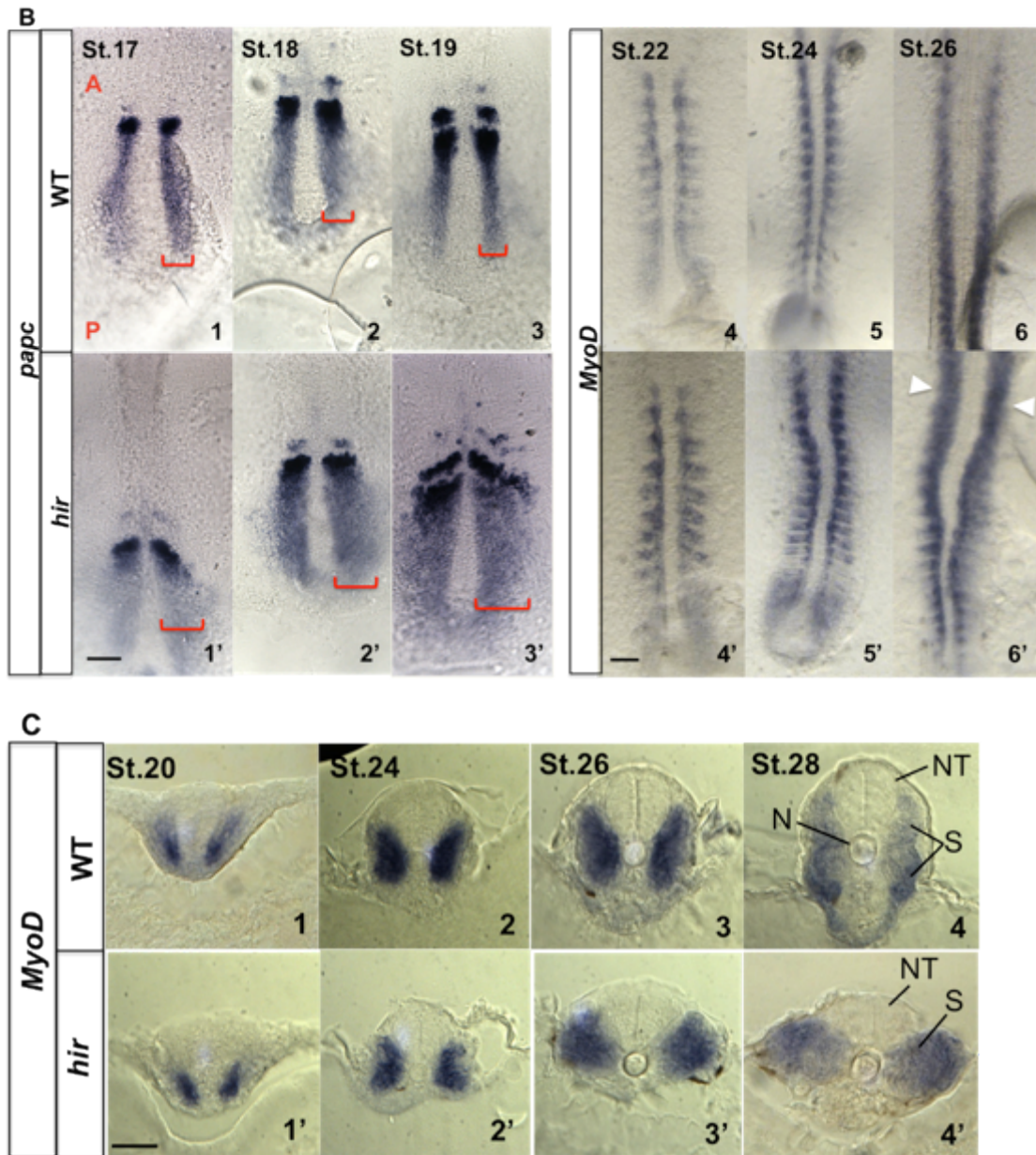
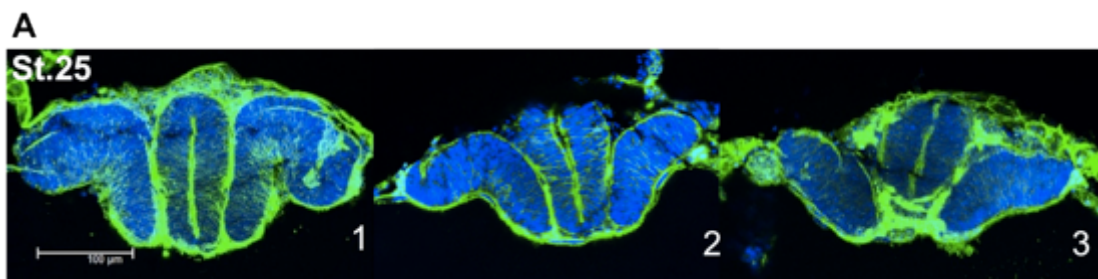


Figure. 3.7 Somitogenesis is disrupted in *hirame* mutants but expression of the *papc* and *MyoD* somite marker genes is essentially unaltered. Stages are indicated top left. **A**, 1-4, 1'-4', Dorsal views of live embryos from st.22 (38 hpf) to st.28 (64 hpf) in somite region. White dotted lines outline the notochord; white arrowheads indicate the unclear somite boundaries. **B**, Dorsal views of the trunk regions showing *papc* and *myoD* expressions during somitogenesis. Red brackets indicate the width of the presomitic mesoderm; white arrowheads indicate unclear anterior part of somites. **C**, Transverse sections of *in situ* hybridization of *MyoD* expressed embryos from st.20 (31.5 hpf) to st.28 (64 hpf). A, anterior; N, notochord; NT, neural tubes; P, posterior; S, somite. Scale bars = 50µm.

3.2.5 *hirame* mutant is hyper sensitive to external forces

Histological analysis of *hir* mutants showed variation in the manner of body flattening, i.e. perpendicularly or sideways (Fig. 3.8 A, 1-3). They didn't collapse in the same fashion. This led me to question whether this was due to the instability of *hir* mutant to maintain its body shape against external forces, such as gravity. Thus, the gravitational experiment was designed and performed to test this hypothesis.

Early stage embryos (st.17, 25 hpf), before collapsing started, were embedded in soft agarose in three orientations, left side down, perpendicular and right side down (Fig 3.8B, 1-3). The results revealed that *hir* embryos collapsed towards the direction of gravity during development, i.e. if embedded left side down, the embryo fell towards left (Fig. 3.8B, 1, 1"). The ventricle angle θ (Fig. 3.8B, 3") was measured. The average in *hir* mutants was $17.3 \pm 10.7^\circ$ (n=14; Fig. 2b) compared to $5.6 \pm 3.3^\circ$ (n=26, $p < 0.01$) in WT (Fig. 3.8D). Even the ventricular zone (arrowheads) in WT embryo was curved in the direction of gravity compared to the straight dotted line (Fig. 3.8B, 1', 3'). Embryos embedded perpendicularly exhibited uniform dorso-ventral compression (Fig. 3.8B, 2', 2"). 64% of *hir* mutants were found affected by the gravitational force, while only 19% of WT embryos had tendency to curve towards direction of gravity (Fig 3.8 C). These data suggested that flattening of mutant embryos was due to inability to withstand external forces (i.e. gravity).



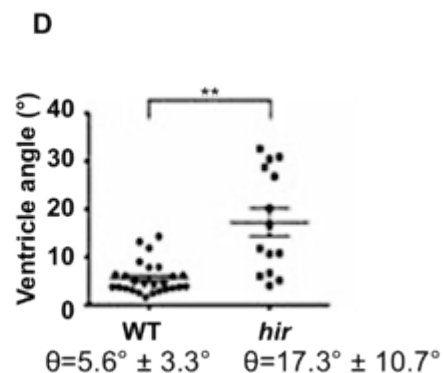
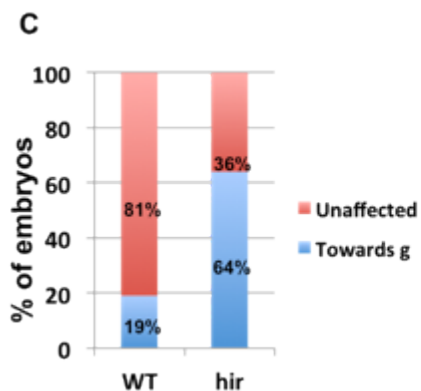
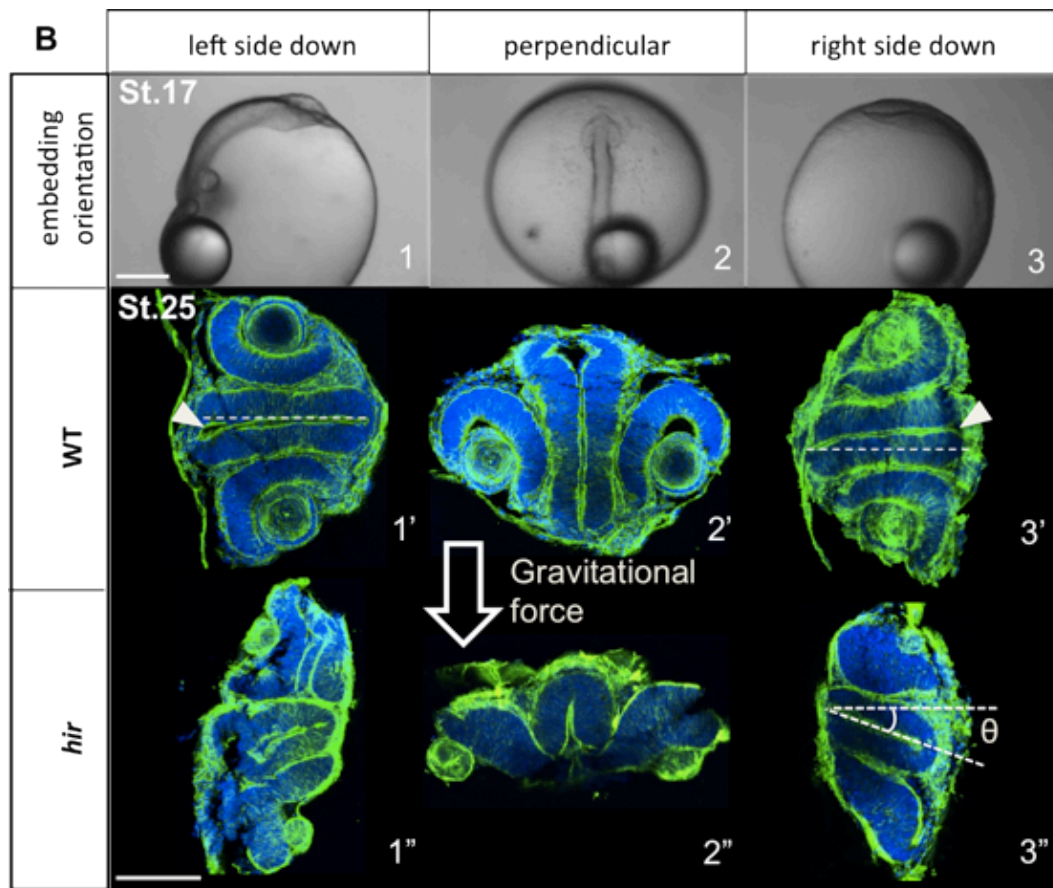


Figure 3.8 *hirame* mutant is hyposensitive to external forces. Stages are indicated top left. **A**, Transverse sections of three different *hir* embryos showing variation of body collapsing. **B**, Gravitational experiment. Live embryos were embedded in soft agarose at early neurulation (st.17, 25 hpf) kept left side down (1), perpendicular to the dish (2) and right side down (3) until st.25 (50 hpf). After fixation, embryos were stained with phalloidin (green, F-actin) and TO-PRO-3 (blue, nucleus). θ is angle that the tangent along the brain ventricle (dotted line in 3'') makes with horizontal solid line. **C**, Static analysis of WT and *hir* embryos affected by gravitational force. Mutants (n=11, 64%) showed a bigger tendency to be affected by the gravity compared with WT embryos (n=27, 19%). **D**, Static analysis of ventricle

angles θ . Mutant embryos ($n=14$, $\theta = 17.3^\circ \pm 10.7^\circ$) showed a greater degree of collapse towards gravity compared with WT embryos ($n=26$, $\theta = 5.6 \pm 3.3^\circ$) ** $P < 0.01$, t-test. Statistical analysis (C and D) in collaboration with Sean Porazinski. Scale bars= 100 μ m.

3.2.6 Pigmentation is affected in *hirame* mutants

Differentiating choroid of the eyes begin to darken due to melanization at st.26 (54 hpf, Iwamatsu, 2004, Fig.3.9 A 1). Pigmentation of the retina advanced with more melanophores forming in WT embryos at st.28 (64 hpf, Fig.3.9A 2). By st.32 (95 hpf), pigmentation of the melanophores in the choroid proceeded as a dark network in the eye (Fig.3.9A 3). Surprisingly, the pigmentation of the retina was completely lost in *hir* mutants (Fig.3.9A 1'-3').

Sox 10, one of Sox family members, has been implicated in the induction and development of the neural crest-derived pigment cells (Aoki *et al.*, 2003); therefore *in situ* hybridisation was performed to determine the spatial expression pattern of *Sox10* in *hir* mutants. At st.21 (34 hpf), *Sox10* expression was detected at the lateral edges of embryo bodies, where neural crest cells formed, in both WT embryos and *hir* mutants, although the staining appeared much weaker in the mutant (Fig.3.9B 1, 1'). From st.23 (41 hpf) onwards, *Sox10* expression was observed in the cranial neural crest of the pharyngeal arches with a strong accumulation in the otic vesicles (Fig.3.9B 2-4). However, *hir* mutants showed reduced *Sox10* expression in these regions (Fig.3.9B 2'-4').

Furthermore, unlike WT embryos, melanocytes were mainly restricted within the embryo bodies at later developmental stages (>st.28, 60 hpf) (Fig.3.9 A 2-3), ectopic melanocytes were observed outside embryo bodies in *hir* mutants (Fig.3.9A 2'-3' arrows).

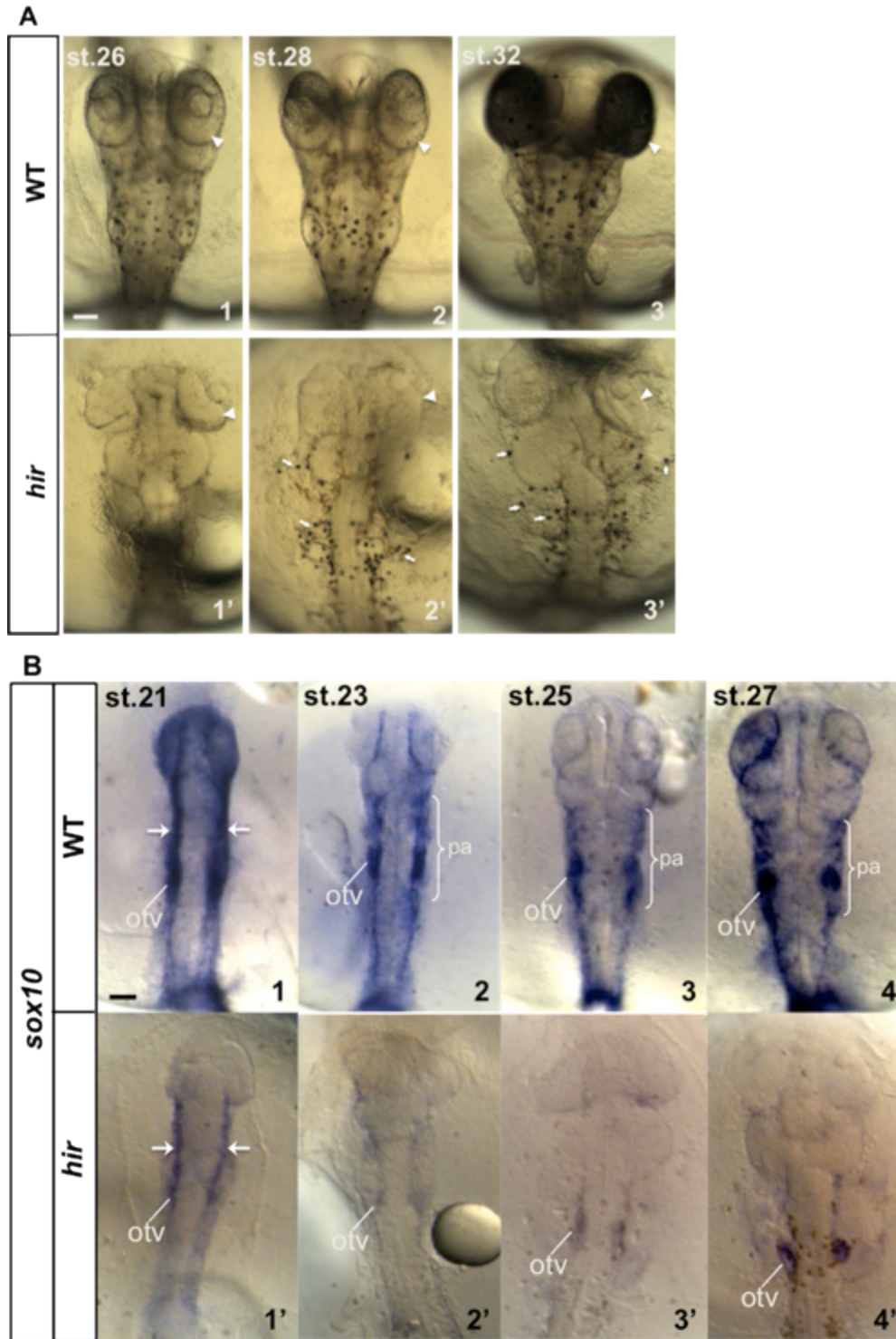


Figure 3.9 Pigmentation is affected in *hirame* mutants. A, Dorsal views of embryos at stage indicated top left. Arrowheads indicate retinas; arrows indicated ectopic melanophores in *hir* mutants. The pigmentation of retina did not occur in *hir* mutants. **B**, Expression of *Sox10* is disrupted in *hir* mutants. Dorsal views of whole-mount *in situ* hybridisation of *Sox10*. Arrows indicated the *Sox10* expression is restricted to the neural crest-forming region. All images anterior to the top. otv, otic vesicle; pa, pharyngeal arches. Scale bar = 40 μ m.

3.2.7 Cell proliferation defects do not underlie the *hirame* phenotype

Since YAP is known for regulating organ size by controlling cell proliferation and apoptosis (Dong J, *et al.*, 2007), cell proliferation and cell death assay was carried out. Whole-mount antibody staining of phosphohistone H3 (PH3, a proliferation marker) and TUNEL assay (to detect apoptotic programmed cell death) were performed at various developmental stages (from st.20 to st.28). In *hir* embryos, apoptosis peaked at st.22 (38 hpf), st.26 (54 hpf) and st.28 (64 hpf, Fig.3.10A & B), much more significant than that in WT embryos, while the cell proliferation rate remained comparable to WT embryos (Fig.3.10C). Interestingly, TAZ (the mammalian paralogue of YAP) knockdown medaka embryos (injection of 0.6ng of translation-blocking morpholino) showed strong reduction in cell proliferation (Fig.3.10 A & C). The results suggest that in medaka, YAP and TAZ have more distinct functions.

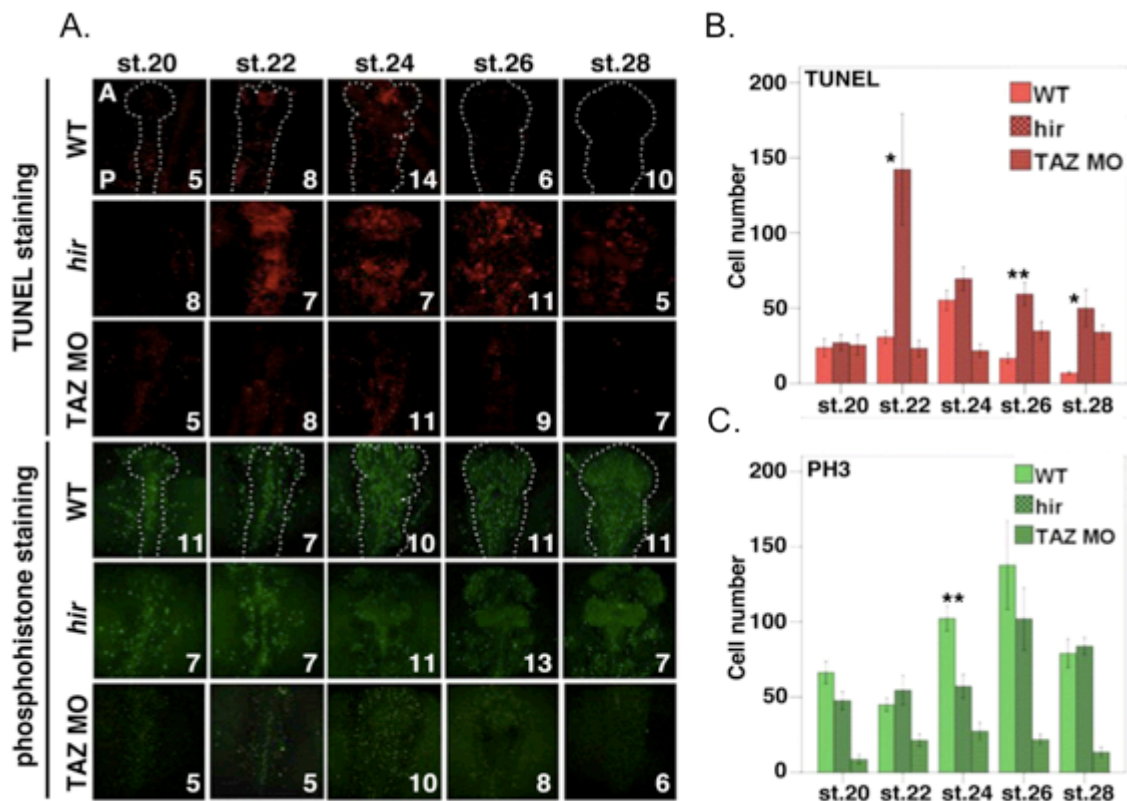


Figure 3.10 Cell proliferation defects do not contribute to the *hirame* phenotype.

A, Whole-mount antibody staining for cell death (TUNEL, red) and cell proliferation (phosphohistone, PH3, green) at various developmental stages in WT embryos, *hir* mutants and TAZ morpholino (MO) injected WT embryos. Dorsal view of all images. A: anterior; P: posterior. White dotted lines outline the embryo bodies. Embryo

numbers are shown in white at bottom right of each image and also apply to the graphs. **B & C**, TUNEL for cell death and phosphohistone H3 (PH3) antibody staining for cell proliferation. Stained cells in the neural tube were counted. Error bars indicate \pm SEM. Statistical significance between WT and mutant groups was tested using two-tailed t-tests (* = $p < 0.05$, ** = $p < 0.01$). Panels B and C in collaboration with Sean Porazinski.

3.3 Discussion

3.3.1 Medaka YAP mutant, *hirame*, exhibits a unique flattened phenotype

YAP-depleted zebrafish showed severe delays in gastrulation, cardiogenesis and hematopoiesis, reduction in brain size including small head and smaller eyes, sign of ventralisation, disruption of somitogenesis and neural crest-derived craniofacial cartilage together with increased apoptosis and reduced cell proliferation (Jiang *et al.*, 2009, Hu *et al.*, 2013). YAP-null mice embryos also exhibited smaller embryo body with defects in yolk sac vasculogenesis and embryonic axis elongation during development (Morin-Kensicki *et al.*, 2006). YAP loss-of-function in *Xenopus* resulted in incomplete epiboly and impaired axis formation (probably due to delayed germ layer specific genes expression, Gee, *et al.*, 2011).

The *hir* mutant embryos also exhibited slow epiboly and it was more pronounced in the maternal YAP KD *hir* mutants (Fig 3.5 A, B, C). Patterning along anterior-posterior (A-P) axis was not affected at early stage in *hir* mutants, but a shortened body axis was observed from st.24 (44 hpf) onwards (Fig.3.6 A). Defects in the Cuvierian ducts (CDs), somitogenesis and neural cells derivatives (melanocytes) were observed. These results were similar to the findings from YAP morpholino-mediated loss-of-function analysis in *Xenopus* and zebrafish (Gee *et al.*, 2011; Hu J, *et al.*, 2013).

Notably, none of the other animal models showed an extremely flattened body, thus making *hir*, the medaka YAP mutant, a useful tool to study how 3D tissues and organs are generated and how they align to give rise to the global body shape. Meanwhile, it also suggests that YAP might have a key role in generating 3D tissue/organ *in vivo*.

3.3.2 Four major traits underlie the *hirame* mutant phenotype including tissue collapse, tissue mislocation/misalignment, absence of essential organs and cell migration defects

The body flattening phenotype of the *hir* mutant was probably associated with the four kinds of defects. First, many tissues became collapsed in the *hir* mutant (Fig 3.6 B). The retinas of *hir* mutant were not constricted basally to

form the optic cup at st.26 (54 hpf); but instead, they opened up and became flattened (Fig 3.6 B 2'). The neural tube and the somite were also found collapsed (Fig 3.6 B 3'; Fig.3.7 C, 3'-4'). The second defect was the misalignment of adjacent tissues such as the lens and the retina. As the optic cup didn't form in *hir* mutant, the lens failed to invaginate into the retina (Fig.3.6 B, 2', C, 1'), dislocated lenses were found in most cases of *hir* mutants. Third, some structures including dorsal aorta, gut (Fig 3.6 B, 3, 3') and brain ventricles (Fig.3.6 2, 2') were found missing in the mutants. This could be due to the formation of such structures did not occur at all; or at a later stage, these structures "disappeared" owing to obsessive apoptosis or missing developmental cues from adjacent tissues. Although the cause was not fully investigated here, it would be worthwhile undertaking further investigation. Cell apoptosis assay at early developmental stage when gut initiation starts can be examined; expression of gut specific markers could also be checked in the mutants during later developmental stages. Finally, impaired cell movements were noticed during embryogenesis. Restricted cell migration was observed during heart development (Fig 3.6 C, 3') as well as the formation of Cuvier's duct (Fig.3.6 C, 2'). A broadened presomitic domain (Fig 3.7 B, 1'-3') and the slow epiboly (Fig.3.5 A, B) found in *hir* mutant also indicated the defective cell movement.

3.3.3 YAP is required to maintain 3D body shape against external forces.

Histological analysis of 2 dpf *hir* mutants revealed tissue collapse in various directions, i.e. perpendicularly or sideways (Fig.3.8 A). And the results from the gravity experiments (Fig.3.8 C) are consistent with the fact that *hir* embryos are less able to withstand external forces (i.e. gravity). This was an interesting finding, as there is no animal model that directly showed how the body is shaped by withstanding external forces. Although *in vitro* study has suggested that 3D organogenesis depends on generation of force, transmission of force via tissues and response from tissues and extracellular matrix (ECM) to force (Mammoto T & Ingber D.E, 2010), little is known about how these dynamic processes are regulated genetically to generate 3D organ or body shape *in vivo*. Recent study has demonstrated a new role of YAP in

mechanotransduction as a sensor and mediator for mechanical cues (Dupont S, *et al.*, 2011). However, the study was also based on cell culture models.

3.3.4 YAP is required for neural crest development and retinal pigment epithelium formation

Neural crest cells are multipotent and migratory cells that only found in vertebrate embryos (Noisa & Raivio, 2014). Many cell types derived from neural crest cells, including peripheral neurons, glia, pigment cells (melanocytes) of the skin, craniofacial cartilage etc. (Noisa & Raivio, 2014). *Sox10*, one of the genes involved in the formation of neural crest, is expressed in neural crest cells and later in glial lineage (Britsch *et al.*, 2001). The expression of *Sox10* was significantly reduced in *hir* mutants throughout the stages examined (Fig.3.9B). Abnormal migration of melanocytes in the mutant was observed at later developmental stages (>st.28, 64 hpf) (Fig.3.9A 2'-3', white arrows). These results suggest that YAP is required for the development of the neural crest cells and their derivatives. This was supported by similar findings reported in zebrafish and *Xenopus*, as the YAP-depleted zebrafish showed defects in neural crest-derived craniofacial cartilage formation (Jiang *et al.*, 2009), and YAP gain-of-function in *Xenopus* (Gee, *et al.*, 2011) expanded the neural plate progenitors and neural plate border zone, while inhibiting the expression of later markers of neural plate border zone derived tissue such as neural crest, pre-placodal ectoderm and hatching gland.

During neurulation, both the lens placode and the optic vesicle invaginate. The lens placode invaginates to form the lens pit while the optic vesicle invaginates to form the optic cups from where the neural retina and retinal pigmented epithelium (RPE) derived (Cvekl and Piatigorsky, 1996). RPE is the only type of pigment cells that is not derived from the neural crest (Tryon *et al.*, 2011). Pigmentation of the retina also did not occur in *hir* mutants (Fig.3.9 A 1'-3'). This could be due to the pigmentation defects in RPE, or the complete lost of RPE. Morphological analysis at later stages (>st.28, 64 hpf) will be useful to identify which scenario is true. Expression of RPE specific markers should also be checked in the mutants.

3.3.5 YAP and TAZ divides functions in medaka and cell proliferation defects do not underlie the *hirame* phenotype

YAP is known to control organ size by accelerating cell proliferation and antagonizing cell death (Dong J, *et al.*, 2007). Unlike the finding from YAP-depleted zebrafish, cell proliferation rate in *hir* mutants remained similar to WT, while apoptosis increased from st.22 (38 hpf) to st.28 (64 hpf) after body collapse (Fig.3.10A-C). Apoptosis of WT embryos peaked at st.24 (44 hpf), and a high incidence of cell death was found in the brain region (Fig.3.10 A), this could be due to the formation of brain ventricles. The *hir* phenotype was not caused by cell proliferation defects. Though cell apoptosis was significantly increased in *hir* mutants at several stages of development, there are however, no *hir*-like mutants in the literature whose phenotype was attributable to cell death.

We questioned why cell proliferation remained close to WT embryos in *hir* mutants. TAZ (the mammalian paralogue of YAP) knockdown medaka embryos showed strongly suppressed proliferation (Fig.3.10 A&C) and the embryos became early embryonic lethal. These data suggest that cell proliferation in medaka is mainly regulated by TAZ, while YAP plays more of an anti-apoptotic/cell survival role.

3.3.6 Summary

YAP has been previously reported as a master gene in regulating organ size by antagonizing apoptosis and promoting cell proliferation. When overexpressed in mouse livers, YAP has the ability to increase liver size dramatically (Dong J, *et al.*, 2007). The YAP knock-out mice are embryonic lethal by E8.5 due to perturbation in yolk sac vascularization and placenta formation (Morin-kensicki *et al.*, 2006), and this restricts a study of YAP function *in vivo* during embryogenesis. Unlike YAP knock-out mice, which are early embryonically lethal, *hir* mutants can progress organogenesis and survive till just before hatching (6 days post-fertilization (dpf)), thus allowing a detailed analysis of embryogenesis as well as organogenesis.

The medaka YAP mutant, *hirame*, has a flattened body in which major epithelial organs collapse and are not properly aligned. Besides missing several structures and having defective cell migration, *hir* mutant is also hypersensitive to external forces. Furthermore, in medaka cell proliferation is mainly regulated by TAZ, allowing the identification of non-cell proliferation dependent YAP mutant phenotypes such as altered 3D body shape. Taken together, these features made *hir* mutant an ideal *in vivo* model to study how YAP affects 3D body shaping.

Chapter 4: Analysis of sensory organ formation in *hirame* mutants.

4.1 Introduction

4.1.1 Overview of sensory placodes

Ectodermal placodes develop from transient thickenings of the embryonic head ectoderm. Sensory placodes are thought to derive from the pre-placodal region (PPR) where all cells are multipotential. They are specialised neurogenic epithelia surrounding the central nervous system (CNS) (Streit, 2008). Sensory placodes include the adeno-hypophyseal, olfactory, lens, trigeminal, profundal, otic, epibranchial and lateral line placodes (Park and Saint-Jeannet, 2010). Initiation of cranial placodes formation occurs quickly after gastrulation when a pre-placodal field of naive ectoderm is established at the border between the anterior neural plate (ANP) and future epidermis (Park and Saint-Jeannet, 2010). Placodes do not only receive signals from surroundings structures, but are also in turn sending signals back, once specified (Streit, 2008). For instance, the olfactory placode is necessary for the normal forebrain morphogenesis; the lens is required for the normal development of the adjacent structure, the retina; and chondrogenesis is induced by the otic epithelia (Park and Saint-Jeannet, 2010). Different cranial placodes undergo morphogenesis differently to give rise to different sense organs. For example, the olfactory, lens and otic placodes invaginate to give rise to the nose, lens and ear respectively, while lateral line placode delaminates to form the lateral line system (Schlosser, 2006; see Fig.4.1).

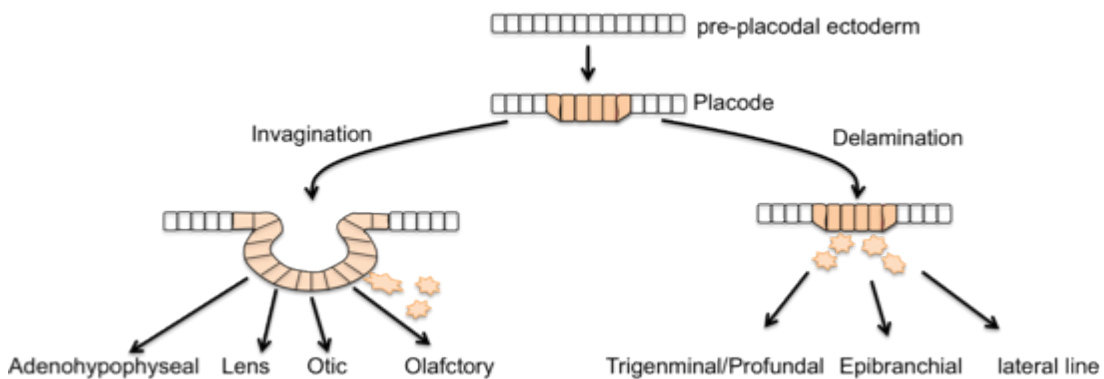


Figure 4.1 Schematic view of morphogenetic processes associated with the development of the early cranial placodes. All cranial placodes develop from a thickening of the pre-placodal ectoderm. Invagination of the placodal epithelium forms the adeno-hypophysis, olfactory epithelium of the nose, lens, and inner ear. In

these placodes, apart from the lens placode, cells will also delaminate to give rise to sensory neurons and secretory cells. Delamination of cells from the placodal epithelium forms the lateral line, epibranchial, trigeminal and profundal placodes (Adapted from Schlosser, 2006).

Three placodes contribute to sense organs: the olfactory, lens and otic. The most anterior of these is the olfactory placode, which develops next to the forebrain. The olfactory placode retains a group of stem cells, which form various differentiated cell types (Schwob, 2002). It also contains secretory cells as well as primary sensory cells. Posterior to the olfactory placode lies the lens placode. It develops adjacent to the future retina and forms the crystalline lens of the eye, comprises lens fiber cells and lens epithelial cells (Lang, 2004). The lens is the only non-neurogenic sensory placode though it is generated from the same territory as the neurogenic placodes (Streit, 2008). The otic placode develops next to the hindbrain and give rise to the entire inner ear and neuron precursors (Ohyama *et al.*, 2007). Formation of medaka sensory placodes is summarized in Figure 4.2.

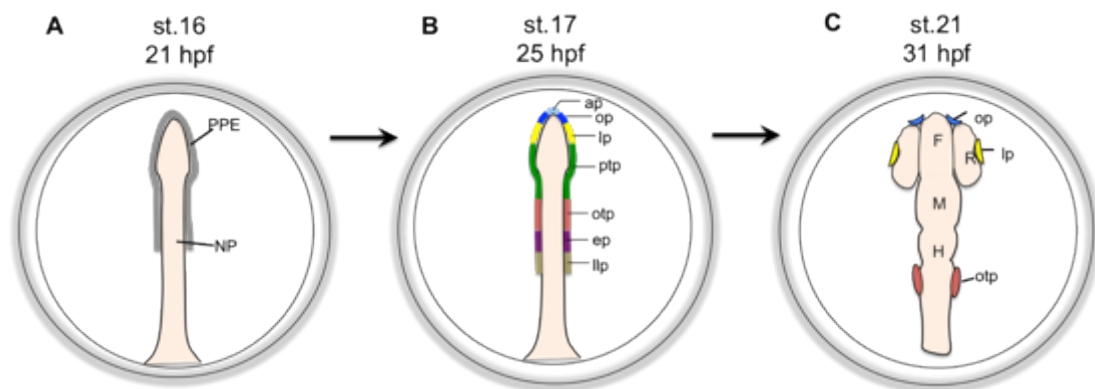


Figure 4.2 Fate map of sensory placodes in a medaka embryo. **A**, At late gastrula stage (st.16, 21 hpf) the pre-placodal ectoderm abuts the neural plate anteriorly. **B**, At early neurula stage (st.17, 25 hpf), a detailed fate map has been established. **C**, Presence of pronounced olfactory, lens and otic placode at st.21 (31 hpf). Dorsal view of all images with anterior to the top. PPE, pre-placodal ectoderm; NP, neural plate; ap, adenohypophyseal placode; op, olfactory placode; lp, lens placode; ptp, profundal and trigeminal placodes; otp, otic placode; ep, epibranchial placode; llp, lateral line placode.

4.1.2 Induction of sensory placodes

Placode induction is considered as a complex multi-step process. The olfactory placode arises from the region at the border of the anterior neural plate and induction of olfactory placode needs signals from anterior mesendoderm as well as from forebrain (Baker & Bronner-Fraser, 2001). BMP signals are also implicated in the specification of olfactory and lens placodes in the chick embryo (Sjodal *et al.*, 2007). *Fgf8* is suggested to promote specification of olfactory cells in chick embryos (Bailey *et al.*, 2006). Wnt inhibition is also required for the olfactory placode specification, while active canonical Wnt signaling is required for the otic placode (Park and Saint-Jeannet, 2008). In zebrafish, Cxcl12/Cxcr4 signaling, members from chemokines of the CXCL class and their receptors (CXCR), regulates assembly of olfactory placodal precursors into a compact cluster to form the olfactory placode (Miyasaka *et al.*, 2007).

Lens induction needs signals from both mesoderm and neural plate (Chow and Lang, 2001). *Par6* expression is essential for lens induction (Chow and Lang, 2001). Bone Morphogenetic Protein (BMP) and Fibroblast Growth Factor (FGF) signalling have been suggested to regulate some of the interactions between the optic vesicle and the future lens ectoderm to form a mature placode (Chow and Lang, 2001), however the early signals responsible for the presumptive lens region setting up remain elusive (Streit, 2004).

Induction of the otic placode depends on the signals from the cranial paraxial mesoderm underlying it and the adjacent tissues, early neural plate and hindbrain (Groves, 2003). FGF signalling is involved in the otic placode induction. Misexpression of both *Fgf3* and *Fgf8* led to an abnormal hindbrain with no otic placode presence (Maroon *et al.*, 2002). However, different members of the FGF family may be involved depending on the species (Ladher *et al.*, 2000; Maroon *et al.*, 2002).

4.1.3 Genes involved in sensory placodes development

The formation of sensory placodes including both induction and specification requires the integration and coordination of transcription factors encoded by various genes. Some of these genes are expressed to establish the pre-placodal ectoderm, while others confer placodal bias to regulate placodes development. Only those involved in the formation of olfactory, lens and otic placode will be discussed here further.

It is believed that all placodes express at least one or more members of the Pax family of paired class homeobox genes during early development (Baker & Bronner-Fraser, 2001). In zebrafish, *Pax8* together with *Pax2* are the earliest known markers of the otic placode (Pfeffer *et al.*, 1998); *Pax6* is an essential marker of the lens and olfactory placodes (Nornes *et al.*, 1998).

Two member from the distal-less gene family, *dlx3* and *dlx7*, are both expressed in late gastrula stage in zebrafish embryos in a stripe corresponding to the future neural plate border (Akimenko *et al.*, 1994). In medaka, *Dlx3*, as well as *Foxil1*, a forkhead-domain containing transcription factor, are expressed during early otic development (Hochmann *et al.*, 2007). *Dlx3* expression is also found in the prospective olfactory primordial (Hochmann *et al.*, 2007).

In zebrafish, the homeodomain transcription factor *six4.1* and the transcription cofactor *eya1* are both expressed surrounding the anterior neural keel at the end of gastrulation (Kobayashi *et al.*, 2000; Sahly *et al.*, 1999). Later expression of both genes is restricted to the olfactory, hypophyseal, otic, and lateral line placodes (Kobayashi *et al.*, 2000; Sahly *et al.*, 1999). A similar expression pattern of *Eya1* is also seen in the medaka.

Sox2 and *Sox3* are the other two molecules that have been reported to be expressed in all sensory placodes in *Xenopus*, chicks and mouse embryos (Uwanogho *et al.*, 1995; Collignon *et al.*, 1996, Penzel *et al.*, 1997; Zygare *et al.*, 1998). In medaka, *Sox3* is expressed in the presumptive placodal

ectoderm and in all placodes including the lens, as well as in the central nervous system (Köster *et al.*, 2000).

In zebrafish, expression of E-cadherin (*cdh1*) is found in the ectoderm, developing pronephros, gut, olfactory vesicle, otic vesicle, and developing brain (Babb *et al.*, 2001; Thisse *et al.*, 2005). The molecular markers used in this chapter are summarised in Table 4.1.

Gene	Description	References
Cdh1	olfactory placode; otic placode	Thisse <i>et al.</i> , 2005 Babb <i>et al.</i> , 2001
Dlx3	olfactory placode; otic placode	Hochmann <i>et al.</i> , 2007
Sox3	olfactory placode; lens placode; otic placode	Köster <i>et al.</i> , 2000
Pax2	otic placode	Hochmann <i>et al.</i> , 2007

Table 4.1 List of molecular markers used to detect the olfactory, lens and otic placode in this chapter.

4.1.4 Development of sensory organs in medaka embryo.

4.1.4.1 Olfactory system formation in medaka

Prospective olfactory placodes and olfactory placodes in medaka form at st.19 (27.5 hpf) and st.20 (31 hpf), respectively. The olfactory placodes then invaginate further to form the olfactory pits. The olfactory placode is important for the development of the forebrain as a whole (Graziadei and Monti-Graziadei, 1992). In *Xenopus*, ablation of the olfactory placodes leads to the failure of development of the forebrain (Graziadei and Monti-Graziadei, 1992).

4.1.4.2 Eye formation in medaka

The emergence of medaka optic buds can be seen at late neurula stage (st.18, 26 hpf) and after 1 hour and half, at st.19 (27.5 hpf), the optic vesicles are formed. Morphogenesis of the optic vesicles to give rise to the optic cups starts at st.21 (34 hpf) when the lens placodes can be seen apposing the optic vesicles and proceeds through st.22 (38 hpf). By st.23 (41 hpf) the formation of spherical optic lenses is complete (Iwamatsu, 2004). Sox3 expression is a

useful marker identifying lens placode (but is also present in other sensory placodes, Köster *et al.*, 2000) and δ -crystallin serves as a useful marker for later differentiated lenses (Lang, 2004). Eye development in medaka embryos can therefore serve as a useful tool to study eye induction and how coordinated growth of different components of the eye occurs.

4.1.4.3 Ear development in medaka

The formation of the otic placodes in medaka starts at st.19 (27.5 hpf) when the two prospective otic placodes can be seen posterior to the hindbrain (Iwamatsu, 2004). Otic placodes then form at st.20 (31 hpf), and the otic vesicles form at st.21 (38 hpf) when the lumen in each otic vesicle can be seen. The development of otic vesicles continues and by st.32 (101 hpf) a fully functional inner ear is formed when all the internal ear structures including the otoliths and the membranous labyrinth have completed formed (Iwamatsu, 2004). The study of zebrafish *vhnf1* mutant (*vhnf1* is involved in caudal hindbrain patterning) has shown that signals from the hindbrain control both anterior-posterior (AP) and dorsal-ventral (DV) patterning of the otic vesicle (Lecaudey *et al.*, 2007).

4.1.5 Aims

As briefly described in Chapter 3, tissues and organs including the brain, eyes, neural tube, and somites are flattened in the *hir* mutant, and are also not properly aligned. In particular, the eyes and ears in *hir* mutants both present interesting and highly visible phenotypes, particularly regarding coordinated development/growth. As sensory placodes give rise to sensory organs, the formation of sensory placodes (the olfactory, lens and otic placode) was first examined in *hir* mutants.

4.2 Results

4.2.1 Formation of sensory placodes is affected in *hirame* mutants

Sox3 transcription factor has been demonstrated as a general molecular marker that is expressed in all sensory placodes in medaka embryos (Köster *et al.*, 2000). Precisely, medaka Sox3 expression has been found in the neuroectoderm, placodes of all sensory organs, and the placode-developed tissues (Köster *et al.*, 2000).

To analyse the phenotype of developing sensory placodes in the *hir* mutant, *in situ* hybridisation with the general sensory placode marker, Sox3, was conducted. In medaka, Sox3 is expressed in the presumptive placodal ectoderm and in all placodes including the lens, as well as in the central nervous system (CNS) (Köster *et al.*, 2000). The results of Sox3 staining indicated that the expression pattern remained unaltered between WT embryos and *hir* mutants at late neurula stages (Fig. 4.3 1-2, 1'-2'), and expression of Sox3 in the central nervous system was not affected in *hir* embryos (Fig. 4.3 1-6, 1'-6'). However, from st.21 (34 hpf) onwards, certain sensory placodes, including olfactory placode and lateral line placodes were not detected (Fig. 4.3 3-6, 3'-6'). Sox3 expression in the otic placode was also altered to be apart from the hindbrain in the mutants (Fig. 4.3 4-6, 4'-6').

A thin layer of lens placode was formed closely to the nascent retina in the WT embryos at st.21 (34 hpf, Fig. 4.3). Then the lens placodes thickened up to invaginate and the spherical optic lenses were completed at st.23 (41 hpf, Fig. 4.3 3-6). Nevertheless, the lens placode was barely detected at st.21 (34 hpf) in the mutant embryo and did not initiate invagination at the later stage (Fig. 4.3 3'-6'). Furthermore, the shape of mutants' lenses was found rather flat compared with WT embryos (Fig. 4.3 4'-6').

Expression analysis of Sox3 in *hir* during embryogenesis revealed that certain sensory placodes, such as olfactory placode and lateral line placode, were missing (Fig.4.3 3'-6'), whereas lenses and otic vesicles were found mislocated throughout early differentiation stages (Fig. 4.3 4'-6'). Further

analysis using specific sensory placode markers would provide more mechanistic insights into the placode phenotype.

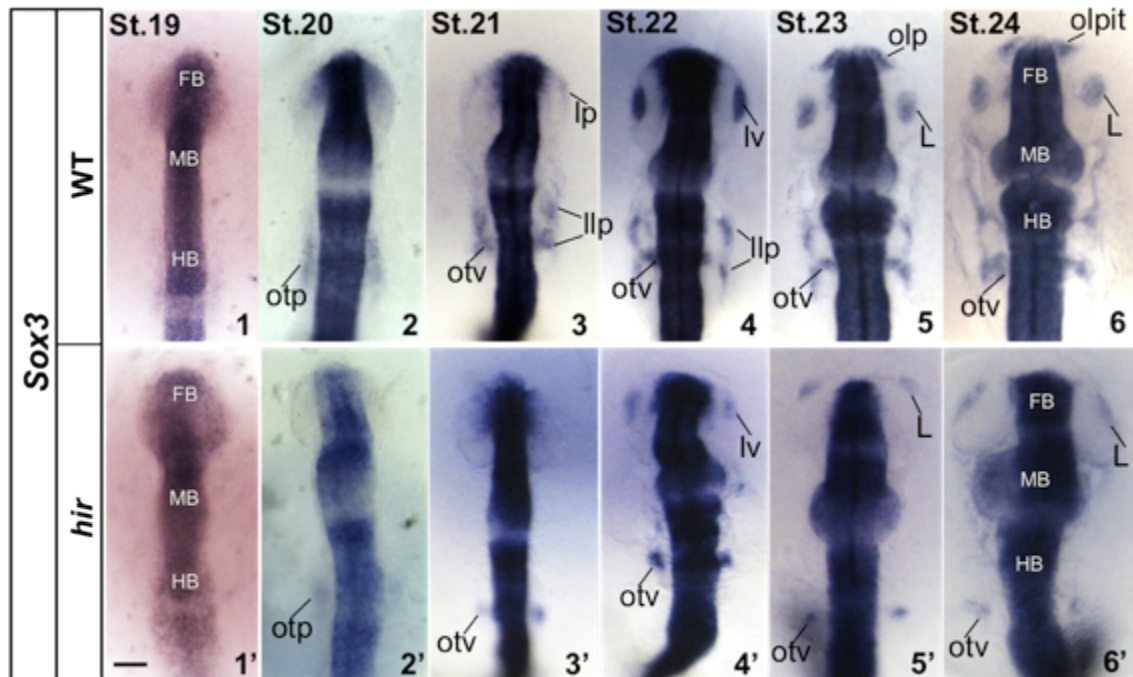


Figure 4.3 Whole-mount *in situ* hybridisation of *Sox3* showing the disrupted sensory placodes formation in *hir* mutant. Stages are indicated top left. 1-6, 1'-6', Dorsal view. Note the missing of certain sensory placodes, including lateral line, lens placode and olfactory placode in *hir* mutants from st.21 onwards. FB, forebrain; HB, hindbrain; L, lens; lp, lens placode; lv, lens vesicle; llp, lateral line placode; MB, midbrain; olp, olfactory placode; olpit, olfactory pit; otp, otic placode; otv, otic vesicle. Scale bar = 40 μ m.

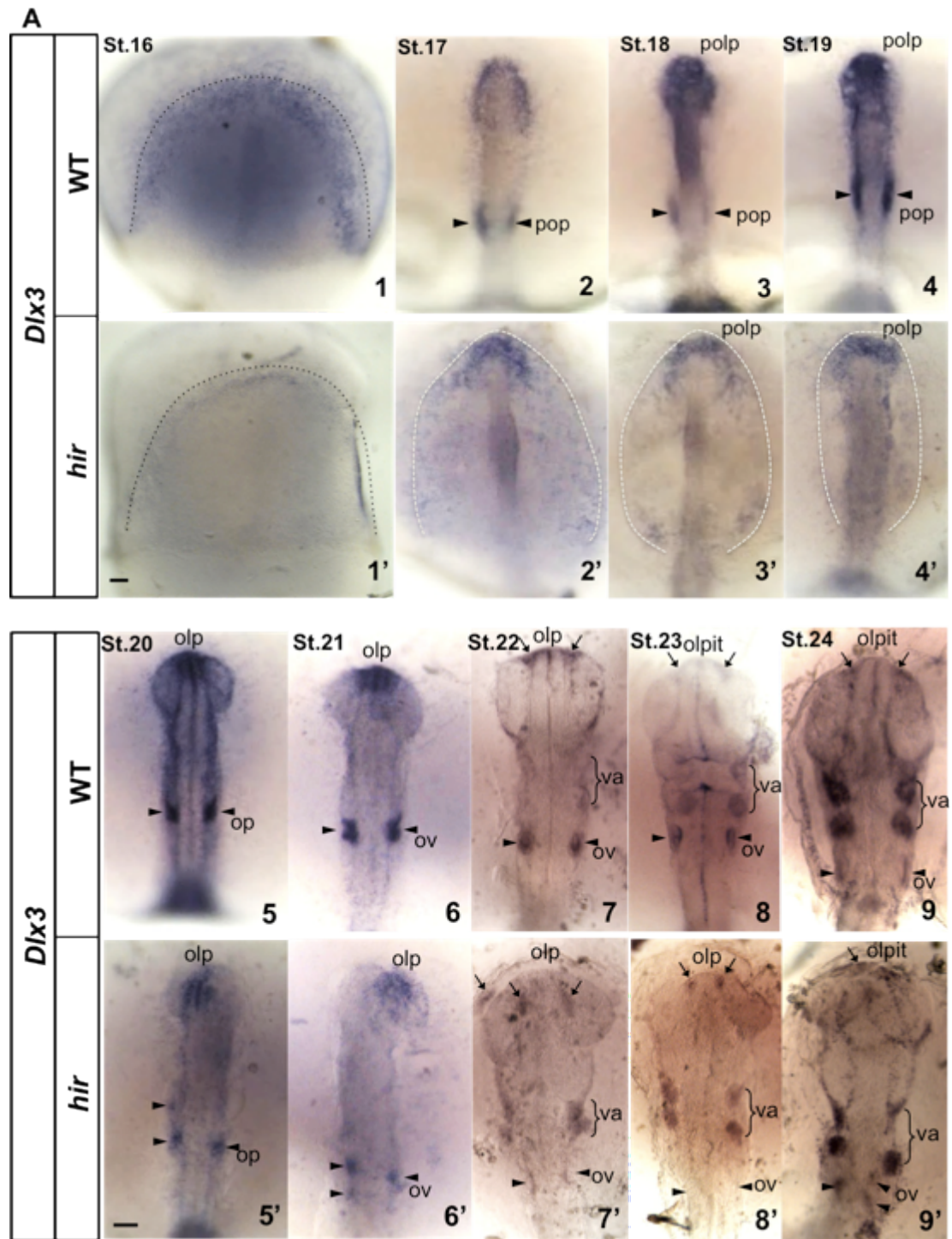
4.2.2 The olfactory placode was mislocated and invagination did not occur in *hirame* mutants

To determine whether the olfactory placode is indeed missing or mislocated in *hir* mutants, an olfactory placode specific marker was needed. *Distal-less 3* (*dlx3*), a transcription factor from the *distal-less* gene family, which is expressed specifically in the otic and olfactory placodes, was used. *Dlx3* is also one of the earliest genes expressed in the otic and olfactory primordia in zebrafish (Akimenko *et al.*, 1994). The spatial temporal expression pattern of *dlx3* in medaka embryos has also been reported (Hochmann *et al.*, 2007).

Dlx3 expression started from mid gastrula stages (st.15, 17.5 hpf) in WT embryos. During late gastrula stage (st.16, 21 hpf), a broad semicircle-shaped stripe was seen within the ectoderm alongside the neural plate in WT embryo (Fig. 4.4 A 1 dotted line), whereas in the mutant, the staining of the stripe was much weaker (Fig. 4.4 A 1' dotted line). During neurulation this stripe moved promptly towards the embryonic body and its intensity started to increase, especially in the prospective otic and olfactory placodes (Fig. 4.4 A 2-4), then the expression became even more intensive in the developing sensory placodes (Fig. 4.4 A 5-6). Ultimately, the transcripts of *Dlx3* accumulated in the presumptive sensory organs, and visceral arches in WT embryos from st.22 (38 hpf, Fig. 4.4 A 5-9). The *hir* mutant showed a delayed enclosing stripe pattern and the intensity of the *Dlx3* staining remained unaltered throughout these stages (Fig. 4.4 A 2'-6'). A much wider and broader *Dlx3* staining pattern of developing olfactory placodes was seen in *hir* mutants (Fig. 4.4 A 2'-6'). Multiple olfactory placodes were observed in the mutant (Fig. 4.4 A 7'). In addition, asymmetric visceral arches were presented in the mutant embryos (Fig. 4.4 A 7'-9').

Expression of another olfactory and otic placodes specific marker, E-cadherin (*cdh1*) was examined. The *cdh1* expression pattern was consistent with that of *sox3* and *dlx3*. The induction of olfactory placode was normal in the mutant embryo (Fig. 4.4 B 1'-3'). From stage 22 (38 hpf) onwards, the bilateral olfactory placodes appeared to be fused and mislocated in *hir* mutant embryos (n=9) (Fig. 4.4 B 4'-5').

The expression pattern of *dlx3* and *cdh1* varied among the *hir* mutants, the size and the location of the olfactory placodes were randomly altered and the placodes were found mostly anterior to or overlying with the forebrain (Fig. 4.4 A 7'-9'; B 4'-5'). These results suggest that olfactory placodes did not invaginate properly and became mislocated in *hir* mutants. .



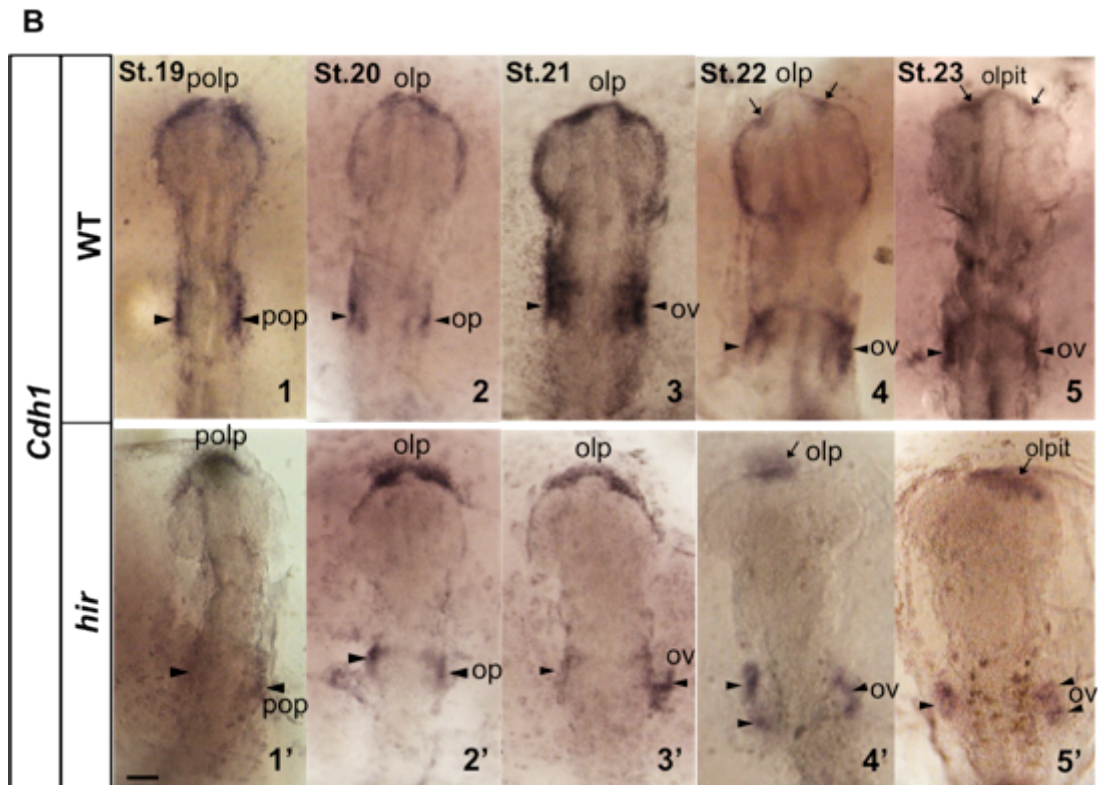


Figure. 4.4 Expression patterns of medaka olfactory and otic placodes specific markers, *dlx3* and *cdh1* during early morphogenesis in WT embryos and *hir* mutants. Stages are shown top left. Dorsal views for all embryos, anterior to the top. **A**, Expression of medaka *dlx3* gene during embryogenesis. **B**, *cdh1* expression during embryogenesis. Black dotted lines outline the inverted U-shaped *dlx3* staining pattern. White dashes outline the pre-placodal ectoderm in *hir*. Arrows indicate olfactory structures; arrowheads indicate otic structures; brackets indicate visceral arches. polp, prospective olfactory placode; olp, olfactory placode; olpit, olfactory pit; pop, prospective otic placode; op, otic placode; ov, otic vesicle; va, visceral arches. Scale bar = 40 μ m.

To reveal the process of the tissue mislocation phenotype, time-lapse microscopy analysis was performed. Olfactory placode development in both WT and *hir* embryos was visualised from st.20 (31.5 hpf) to st.23 (41 hpf). In WT embryos, prior to olfactory placode specification (st.20, 31.5 hpf), a thin layer of cells over the developing forebrain and optic vesicles, from where olfactory and lens placodes derived was observed (Fig 4.5 A 1). This layer of cells later forms distinct olfactory and lens placodes (Fig 4.5 A 2). The thickened olfactory placode then invaginate to form the olfactory pit (Fig. 4.5 A 4). In the *hir* mutant, this thin layer of cells was not found. The invagination of

olfactory placode did not occur and throughout embryogenesis the olfactory placode appeared to aggregate in front of the forebrain (Fig. 4.5 A 1'-4').

To further understand the cellular events leading to the abnormal olfactory placode formation in *hir* mutants, time-lapse confocal microscopic analysis of embryos injected with membrane EGFP and nuclear red fluorescent protein (EGFP-CAAX+H2B-RFP, MNFP) mRNAs was performed. At pre-placode stage (st.19, 27.5 hpf), the prospective olfactory placodes can be seen as a single layer of cells overlying the developing forebrain and optic vesicles in the WT embryo (Fig. 4.5 B 1). During the process of invagination (st.21- st.23, 34-41 hpf) the cells of olfactory became elongated (Fig. 4.5 B 5). Through early morphogenesis, the anterior part of the forebrain and retina appeared to change morphologically in co-ordination with invagination of the olfactory placode in the WT embryos (Fig. 4.5 B 3-5). In *hir* mutants, however, such a single layer of placodal cells was not observed. The cells in the olfactory placode appeared to gather and remained anterior to the forebrain throughout morphogenesis stages (st.19-st.23, 27.5-41 hpf) (Fig. 4.5 B 1'-5'). The changes in cell shape and forebrain morphology were also not seen.

The time-lapse analysis further supported the findings from the *in situ* hybridisation analysis; the olfactory placode was dislocated in *hir*, together with a defect in placodal cells migration. These results also suggested a role of YAP in the regulation of coordinated organ growth and morphogenesis, as the *hir* mutant embryos exhibited a defect in the morphological changes in the developing olfactory placode, forebrain and retina, which probably prevented the invagination of olfactory placode.

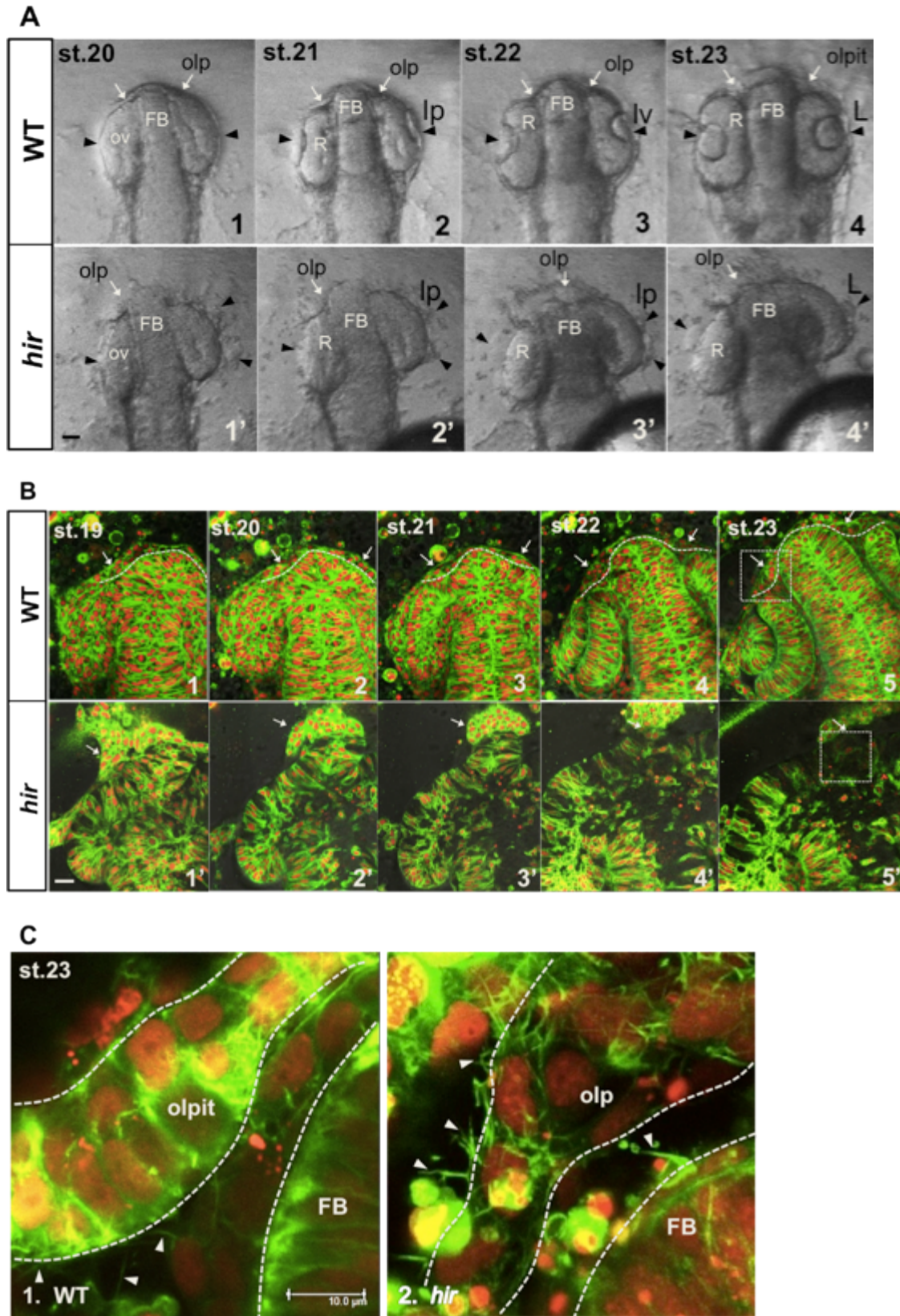


Figure. 4.5 Olfactory placode formation and later invagination is disturbed in *hir* mutants. **A**, Frames from a bright-field time-lapse movie showing WT and mutant olfactory tissue development. Stages are indicated top left. Arrows indicate olfactory

structures; arrowheads indicate lens structures. **B**, Frames from fluorescence time-lapse movie of embryos injected with membrane EGFP and nuclear red fluorescent protein (MNFP) mRNAs. White dotted lines outline the olfactory placode in the WT embryos. White arrows indicate the olfactory pit. Note the fragments of olfactory placode cells sitting on top of the *hir* forebrain. **C**, Aberrant filopodia protrusions were found in the *hir* olfactory placode. 1-2, Boxed area in B 5, 5' were magnified. White dotted lines outline the forebrain and olfactory pit in WT embryo and olfactory placode in the mutant. Arrowheads indicate the filopodia protrusions. Dorsal views for all embryos with anterior to the top. FB, forebrain; L, lens; lp, lens placode; lv, lens lv, lens vesicle; olp, olfactory placode; olpit, olfactory pit; ov, optic vesicle; R, retina. Scale bar (A, B)= 20 μ m; (C)= 10 μ m.

4.2.3 Malformation of the retina and the lens in *hirame* mutants

The process of lens placode formation and eye development was analysed by the time-lapse microscopy from st.20-23 (31.5-41 hpf, Fig. 4.5A). A thin layer of cells, from where lens placode derived, can be visualised overlying the optic vesicles in WT embryo at st.20. (31.5 hpf, Fig. 4.5A 1; Fig. 4.6 1). The lens placode thickened from st.21 (34 hpf) while the retina started to invaginate to form the optic cup. By st.23 (41 hpf), the C-shaped optic cup and spherical lens were formed in WT embryo, and the lens invaginating into the optic cup spontaneously (Fig.4.5A 5). At this stage, many fine filopodia protrusions (from the embryos injected with MNFP) were observed in between the lens and the retina, mainly from the lens side to the retina (Fig. 4.6 2 white arrowheads).

In *hir*, however, fragmented lens placodes were observed at st.20 (31.5 hpf, Fig. 4.5A 1' right side). These fragmented lens placodes were found detached from the optic vesicle (Fig. 4.6 1'). Strikingly, more filopodia protrusions were seen from the fragmented lens placodes in *hir* at st.20 (31.5 hpf). Long aberrant protrusions were mainly formed from the side of the lens placode opposite to the optic vesicle. The detached lens placode gradually reattached to the retina and formed one round lens (Fig. 4.5A 1'-4'; Fig. 4.6 2'). Unlike WT embryo, very few filopodia were found at the interface between the lens and the retina in *hir* mutants. Rather, randomized filopodia protrusions were

again seen from lens opposite to the retina (Fig. 4.6 2', white arrowheads). Furthermore, no lens invagination or retina basal constriction was observed in the mutant (Fig. 4.5A 2'-4'), the lens remained fairly oval compared to the WT embryo (Fig. 4.5A 3-4, 3'-4').

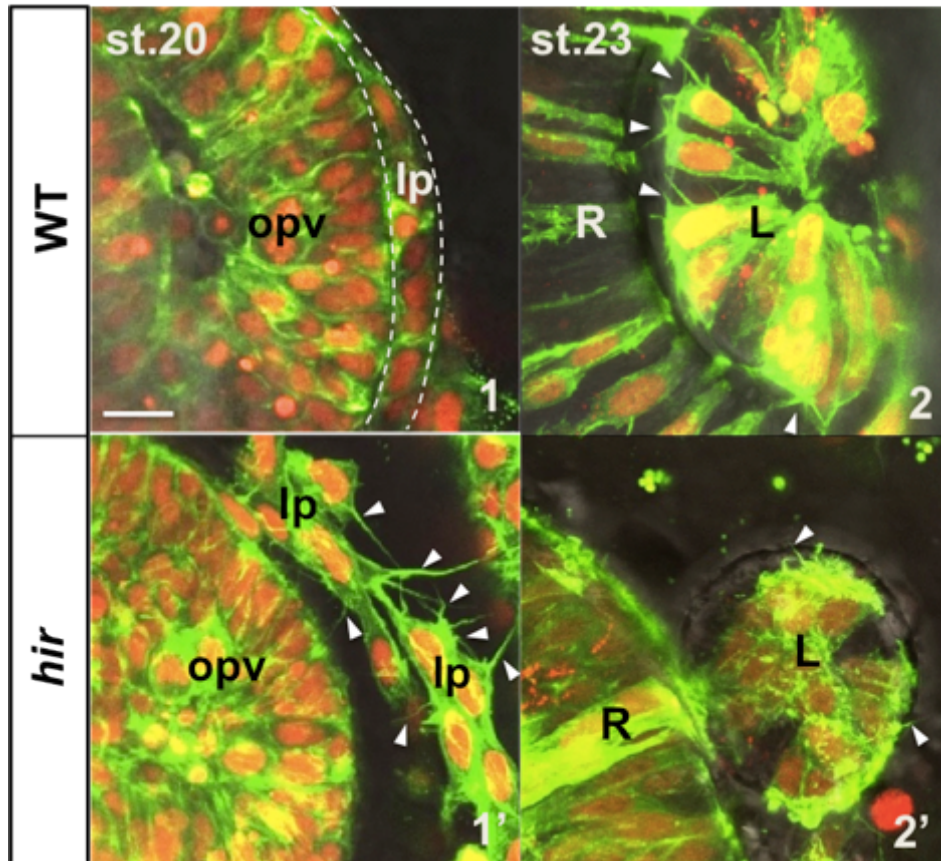


Figure 4.6 Abnormal filopodia formation can be seen between the lens and retina in *hirame* mutants. Stages are indicated top left. Dorsal view of confocal microscopy images of MNFP injected WT and *hir* embryos. Fine filopodia protrusions from both lens and retina in WT embryo (1, 2), and aberrant and randomized filopodia protrusions from the lens side in *hir* mutants (1', 2'). White arrowheads indicate filopodia protrusions. White dotted lines outline the lens placode in WT embryo. L, lens; R, retina; lp, lens placode; opv, optic vesicle. Scale bar = 10 μ m.

Immunohistochemistry (IHC) analysis revealed defective lens and retina morphological changes in *hir* mutants. Difference of the developing eyes in WT and *hir* can be seen from st.21 (34 hpf), when the disturbance can be seen at the junction where the optic cup connects to the forebrain (Fig. 4.7 1' arrow). As morphogenesis proceeding, the thickness of WT forebrain and optic cup started to increase, whereas it was unchanged or even reduced in

hir mutants (Fig. 4.7 2-3, 2'-3'). Moreover, the optic cup of *hir* detached from the forebrain and opened up from st.23 (41 hpf) onwards (Fig. 4.7 2'-3' arrows). Abundant cell death was detected by Caspase 3 antibody staining at the junction where the optic cup separated from the forebrain (Fig. 4.7 2'-3', arrows). A few apoptotic cells were seen in WT embryo at st.23 (41 hpf), this was due to the separation of the lens from the anterior margin of the developing retina (Fig. 4.7, 2).

At st.24 (44 hpf), three distinct cell types can be seen in the lens of WT embryo: 1) brick shaped anterior epithelium (Fig. 4.7, 3, white arrowhead); 2) round or ovoid shaped cells in the organising center (Fig. 4.7, 3, yellow asterisk) ; and 3) elongated fiber cells wrapping around the cells in the center (Fig. 4.7, 3, red arrowhead), and this is the indication of differentiated lens (Greiling & Clark, 2009). However, these distinctive cells were not present in *hir* lens (Fig. 4.7 3'), which led to the suspicion that the lens differentiation occurred properly in *hir*.

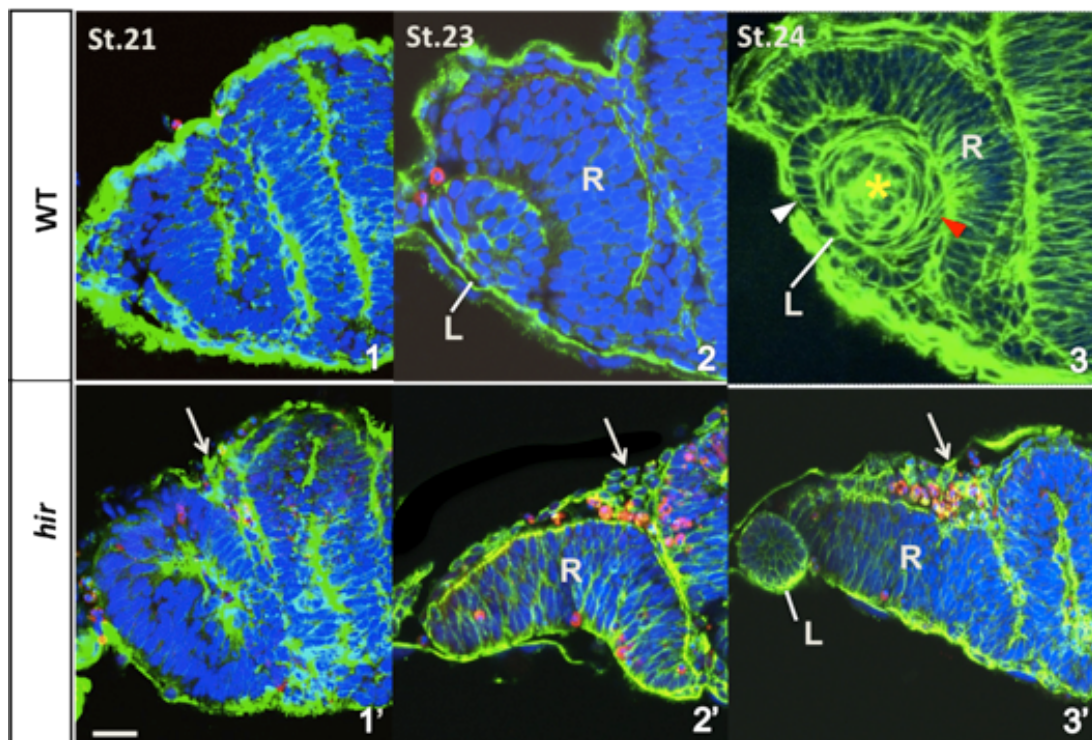


Figure 4.7. Pronounced apoptosis is detected where the optic cup detaches from the forebrain and opens up. Transverse sections of WT and *hir* mutants at the level of forebrain. Caspase 3 antibody (red, apoptosis), phalloidin (green, F-actin) and TO-PRO-3 (blue, nucleus). Arrows show the apoptotic cells at the opening of the

optic cup from the forebrain. White arrowhead indicates brick shaped anterior epithelium; yellow asterisk indicates ovoid shaped cells in the organising center and red arrowhead indicates elongated fiber cells. L, lens; R, retina. Scale bar = 20 μ m.

In order to investigate whether the *hir* lens was differentiated, a lens differentiation marker, δ -crystallin, which is specifically expressed in the lens fibers was employed, (Kondoh, 1999). Expression of δ -crystallin was detected throughout the lens differentiation stages (>st.24, 44 hpf) in *hir*. Unexpectedly, in about 43% cases (9/21 *hir* embryos), multiple differentiated lenses were present in the mutant (Fig. 4.8 2'-3', arrowheads). As these multiple lenses were found surrounding the retina, thus they were more likely due to the fragmentation rather than ectopic formation causing the mislocation.

Again these data indicate the possibility that YAP is required for the coordinated growth of the eye and the forebrain and the development of the eye in medaka embryos, since abnormal morphogenesis was observed in the *hir* lens, retina and forebrain.

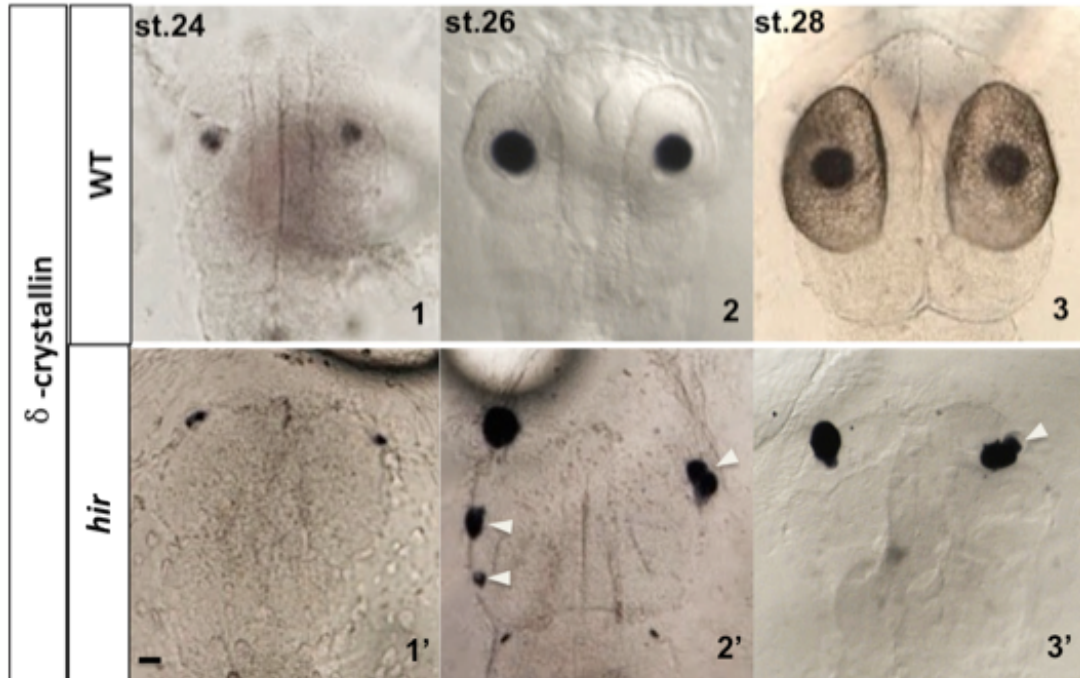


Figure 4.8 Multiple mislocated differentiated lenses are observed in *hir* embryos. Stages are indicated top left. All views are dorsal and anterior is up. δ -crystallin *in situ* staining identify multiple and fragmented lenses in *hir* embryos from st.24-28 (44-64 hpf). Arrowheads indicate the dislocated and fragmented lenses in

hir embryos. Note that smaller and less round lenses detected at st.24 (44 hpf) in *hir* embryo compared to WT embryo, suggesting that the lens differentiation might be affected in the *hir* mutants. Scale bar = 20 μ m.

4.2.4 Early ear development is disrupted in *hirame* mutants

In situ staining of *dlx3*, one of the earliest genetic markers expressed during early otic development in medaka embryos (Hochmann *et al.*, 2007) suggested the induction of otic placode was affected in *hir* mutant. While the prospective otic placodes can be seen from st.17-19 (25-27.5 hpf) in WT embryo, *dlx3* stained cells in the pre-placodal ectoderm were still migrating towards the neural plate in the mutants (Fig.4.4A 2-4, 2'-4'). Smaller and multiple otic placodes/vesicles were observed during later stages (Fig.4.4A 5'-6', 9'). The intensity of *dlx3* expression of the otic structure in *hir* embryos was much weaker compared with WT embryos (Fig.4.4A 2-9, 2'-9'). *Cdh1* expression during later stages of otic vesicles formation also confirmed the presence of multiple otic structures in *hir* (Fig.4.4B 4'-5'). *In situ* hybridisation of *Sox3* indicated the mislocation of otic placodes (Fig.4.3, 4'-6'). These data indicated the induction and formation of otic placode was affected in *hir* mutants.

The development of WT and *hir* ear was again recorded by time-lapse microscopy. The formation of otic vesicle in WT embryo can be visualised from st.21 (34 hpf) when lumenisation initialised (Fig.4.9A 2). However, almost no obvious lumen of ears can be seen until st.23 (41 hpf) in *hir* (Fig. 4.9A 4'). Transverse section of st.23 (41 hpf) *hir* embryos showed a much smaller lumen in the ear compared to WT embryo (Fig.4.9B 1-2, 1'-2'). Not only multiple otic placodes were found in the mutant embryos, but also multiple lumens (3/6 *hir* embryos) could be found in *hir* ear (Fig.4.9B 3'). All these findings implied a delayed lumenisation in *hir* mutant.

The overall morphology of *hir* ear remained rounder (Fig.4.9A 4-5, 4'-5') and the cellular arrangement within the ear also appeared perturbed (Fig.4.9 B 2', C 2'). Multiple cells were seen in the otic epithelium at an early stage (st.23, 41 hpf) and the cell shape was rather round in the mutant (Fig.4.9B 2'). At

later developing stage (st.28, 64hpf), a flattened dorsal otic epithelium can be observed in the mutant (Fig.4.9C, 3' arrows) compared to the elongated cells in WT embryo (Fig.4.9C, 3 arrow). Expression of *Pax2*, another medaka otic placode marker, was found mostly restricted to the ventro-medial wall of the ear during later stages in WT embryo (Fig.4.9C, 3). But in *hir*, the staining of *Pax2* was found mainly in the ventral side of the ear vesicles. This could be due to the collapsing of ear vesicles.

Furthermore, the coordinated growth of the hindbrain and the ear was affected in *hir* mutant. Hindbrain morphogenesis and ventricle expansion did not occur properly in *hir*. The formation of hindbrain ventricle started at st.23 (41 hpf) in WT embryo, and by st.28 (64 hpf) a wing-shaped expanded hindbrain was seen together with the invaginated ear (Fig.4.9B 1; C 1). However, the ventricle did not form in the mutant, nor did the expansion of the hindbrain or the invagination of the ears happen (Fig.4.9B 1'; C 1'). The *hir* hindbrain was rather small compared to WT and its shape remained tubal (Fig. 4.9C 1'; C 1').

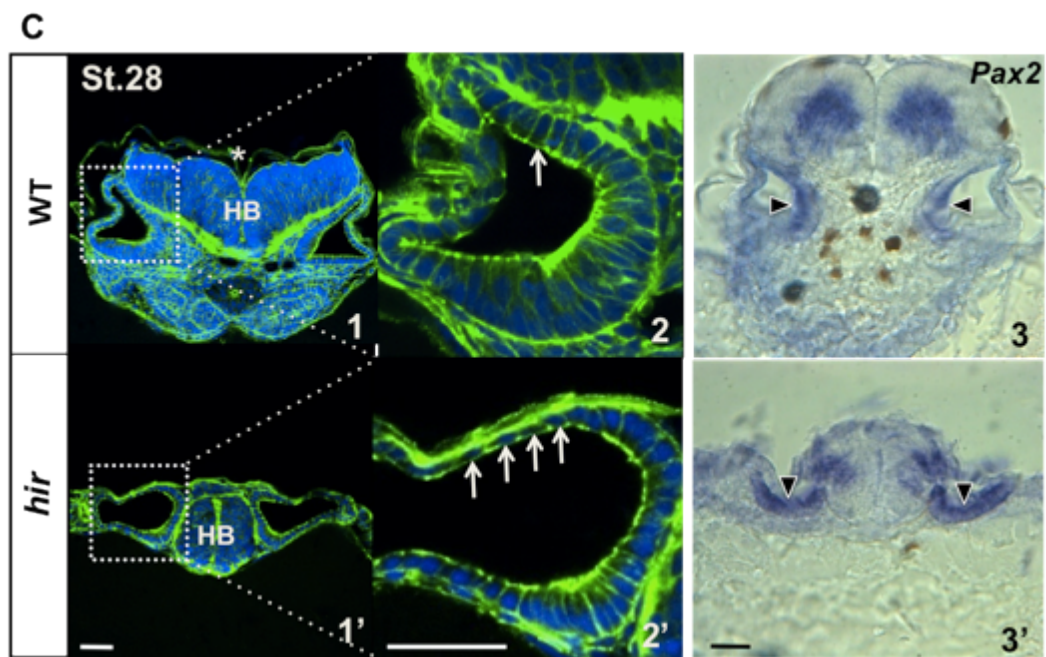
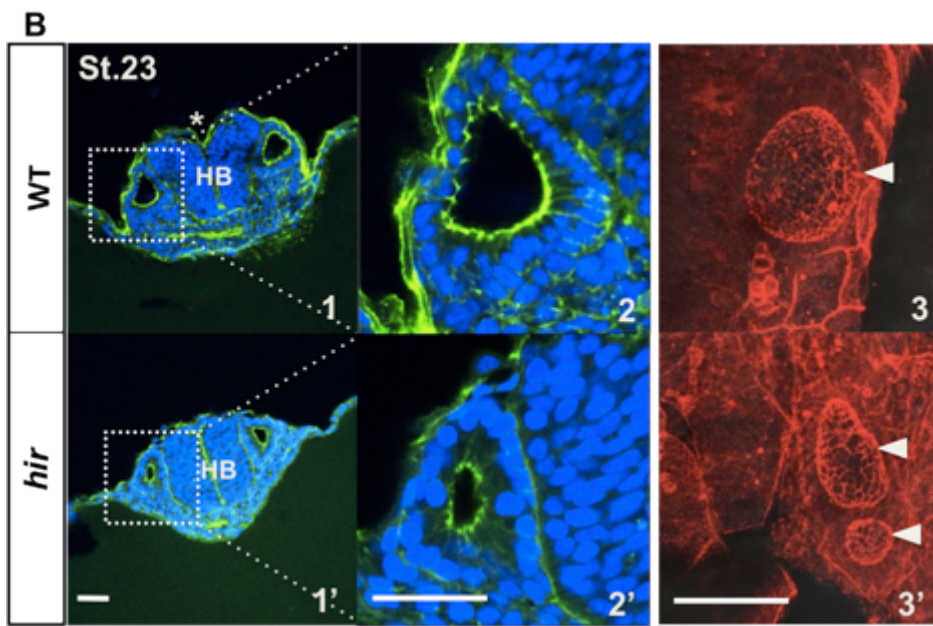
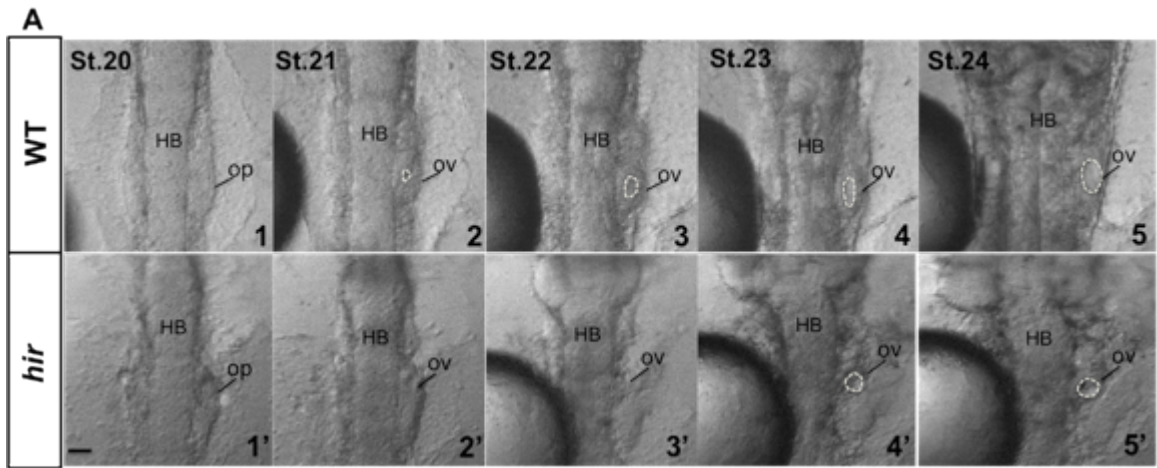


Figure. 4.9 Early ear development is disturbed in *hirame*. Stages are indicated top left. **A**, Still images from a bright-field time-lapse movie showing WT and *hir* mutant early ear development. All images are dorsal with anterior up. White dotted lines outline the lumen. **B**, Lumenisation was impaired in *hir* mutant. (1-2, 1'-2') Transverse sections stained with Phalloidin (green, F-actin) and TO-PRO-3 (blue, nucleus) showing lumen of the ear in *hir* is much smaller, suggesting a delay in the lumenisation. Dorsal is up. 2, 2' are the magnifications of 1, 1' respectively. (3, 3') Dorsal views of Phalloidin (red, F-actin) stained WT embryo and the *hir* embryo with multiple lumens appearing in the ear. White arrowheads indicate the lumen. **C**, Transverse sections of st.28 (64 hpf) WT and *hir* embryos showing that the cell alignment is affected in the ear epithelium in the mutant. (1-2, 1'-2') Embryos stained with Phalloidin (green, F-actin) and TO-PRO-3 (blue, nucleus). Arrows indicate the ear epithelium with different cell shape. Dorsal is up. 2, 2' are the magnifications of boxed areas in 1, 1' respectively. (3, 3') Transverse sections of *pax2 in situ* stained embryos. Arrowheads indicate the expression pattern of *pax2* in otic vesicles at stage 28. Asterisks indicate the sulcus of hindbrain in WT embryos. HB, hindbrain; op, otic placode; ov, otic vesicle. Scale bar = 30 μ m.

4.3 Discussion

4.3.1 The development of sensory placodes is affected in *hirame* mutants

The sensory placodes derive from the pre-placodal ectoderm at the end of gastrulation. The lens, olfactory and adeno-hypophyseal placodes originate from the anterior placodal area, while the posterior placodal area gives rise to the epibranchial, otic and lateral line placodes. Development of the olfactory, lens and otic placodes of medaka embryo were studied. The olfactory placode is the most anterior of the three and it develops with the forebrain and invaginates gradually in between the forebrain and retina in WT embryo (Fig. 4.5 A, B). Lying posterior to the olfactory placode is the lens placode. The lens placodes develop adjacent to the nascent retina and they undergo coordinated morphogenesis during embryogenesis, the WT retina constricts basally while the lens invaginates (Fig. 4.5 A, B). At a later stage of development (st.24, 44 hpf), lens cells differentiated into the two major cell types: lens epithelial cells and lens fiber cells (Fig. 4.7).

The transcription factor of *distal-less* gene family, *dlx3*, is highly expressed in the pre-placodal region at neural plate stages, and subsequently intensively expressed in olfactory and otic placodes in zebrafish (Akimenko *et al.*, 1994). Expression of *dlx3* in medaka embryos was detectable at mid gastrula stage (st.15, 17.5 hpf). Within four hours (st.16, 21 hpf), expressing cells coalesced into a semicircle-shaped stripe that around the lateral edge of the neural plate. By the end of gastrulation (st.17, 25 hpf), *dlx3* expressing cells had reached the edge of the neural plate and were accumulated in olfactory and otic placodes in WT embryos. The stripe expression of *dlx3* was seen at st.16 (21 hpf) in *hir* mutant, however, the signal was much weaker and enclosing of the stripe towards the neural plate was distinctly delayed (Fig. 4.4A). This was possibly due to the cell migration/movement defect observed earlier in epiboly in the *hir* mutant.

Expression analysis of *sox3*, a general sensory placode marker of medaka embryo, revealed defects in the development of the olfactory, lens, otic and

lateral line placodes in *hir* mutant (Fig.4.3). The lens placode was barely detected in *hir* (n=11), while in WT embryo it was formed adjacent to the nascent retina. At later developmental stages, the lens placode thickened up to invaginate and generated the spherical crystalline lens in WT, however, in *hir* mutant, the thickening of lens placode did not occur and remained rather flattened. The otic placode was detected in both WT and mutant embryos, but it appeared less adjacent to the hindbrain in *hir*. The olfactory placode that developed into olfactory pit was not observed in *hir* mutant. For further investigation, placode specific markers need to be employed.

The lateral line placodes were also found missing in *hir* mutant (Fig.4.3). However, the expression analysis of lateral line placode specific markers, such as *Prox1a*, which is expressed in the lateral line primordium (Glasgow & Tomarev, 1998), is necessary to be done in the mutant to confirm whether the induction of the lateral line placode is disrupted or it is dislocated as other sensory placodes at later stages. Evidence was shown in a zebrafish study that the development of lateral line system was affected by the morpholino-mediated knockdown of YAP in zebrafish (Loh *et al.*, 2014). The study reported that zebrafish Yap1 was highly expressed in the proliferation zones and especially in the posterior placodal area from where otic and lateral line placodes originate and it also regulates one of its downstream target, *prox1a*, which controls the differentiation of the cells in the lateral line cells (Loh *et al.*, 2014).

4.3.2 Sensory placodes do not invaginate and become mislocated with the presence of multiple placodes at later stage in *hirame* mutants

All sensory placodes originate from a thickening of the ectoderm, and the invagination of olfactory, lens, and otic placodal epithelium subsequently forms the olfactory pits, lens, and inner ear (Schlosser, 2006). In *hir* mutants, the placodes of these sensory organs were mislocated; multiple placodes/vesicles were also observed in *hir* mutants. Besides, nascent sensory epithelia did not invaginate.

Time-lapse microscopy analyses revealed randomly mislocated sensory placodes and a loss of invagination during development (st.20-24, 31.5-44 hpf) (Fig. 4.3, 4.4, 4.5 and 4.9). The lens placodes were fragmented and dislocated in *hir* mutants during early lens formation at st.20 (31.5 hpf) (Fig. 4.5A and 4.6). The olfactory and otic placodes were also dislocated in the *hir* mutants (Fig. 4.3 and 4.5A), and the invagination of adjacent neural epithelia did not occur (Fig. 4.5 and 4.9). The coordinated invagination of the olfactory pit into the forebrain, presumptive lens into the retina and the otic vesicle into the hindbrain failed in *hir* mutants. The morphological changes in the forebrain, retina and hindbrain during embryogenesis were also aberrant in *hir* mutants (Fig. 4.5, 4.7 and 4.9). In the mutant, the forebrain did not extend anteriorly nor the invagination of the retina occurred, and the ventricle in the hindbrain did not form,

The time-lapse and *in situ* hybridisation analysis showed multiple lenses and otic vesicles in *hir* mutants. In the case of the eye, multiple fragmented lens placodes, which are detached from the nascent retina, were seen at early stage and then re-joined later before rounding up and loosely adjacent to the retina (Fig.4.5A). Further analysis of *in situ* hybridisation of δ -crystallin in *hir* mutants showed the presence of smaller multiple differentiated lenses at later developmental stages (st.26-28, 54-64 hpf). As these multiple lenses were found surrounding the retina, they were more likely due to the fragmentation of early lens placodes rather than ectopic formation. Interestingly, the medaka *eyeless* (*el*) mutant, which lacks eyes completely is due to the failure of evagination of optic vesicles (Winkler *et al.*, 2000). The mutation is caused by an intronic insertion in the *Rx3* gene and *Rx3* activity is necessary for optic vesicle evagination and optic vesicle proliferation (Loosli *et al.*, 2001). The evagination of optic vesicles was affected in *hir* mutants (Fig.4.5 A-B), thus it will be worth checking whether the *Rx3* expression level is altered in the mutants.

In the case of the ear, *in situ* hybridisation staining of *dlx3* showed the delayed otic placode induction with the presence of multiple placodes in *hir* mutants (Fig.4.4). Interestingly, multiple lumens were also found in the mutant ear at

later stages (Fig.4.9B). Analogous to the lens placode, it is likely that fragmenting otic placodes might result in multiple lumens. Alternatively, expression of genes involved in lumen formation might be altered in *hir* mutants. Zebrafish *tcf2* (*vhnf1*) mutants, the mutants associated with the human disease MODY5 (maturity-onset diabetes of the young, type V) and familial GCKD (glomerulocystic kidney disease) develop multiple lumens in the intestine (Bagnat *et al.*, 2007). These mutants have patterning defects in gut primordia, pronephores and hindbrain, which then lead to the malformation of the liver, the pancreas, the pronephores and the otic vesicles (Lecaudey *et al.*, 2007; Sun & Hopkins 2001). The otic vesicles of *vhnf1* mutants appear much smaller in size (Lecaudey *et al.*, 2007). It is worth examining if mRNA and protein level of *vhnf1* is altered in *hir* mutants. Third possibility could be the mislocalisation of tight junctions (TJs) regulatory proteins and polarity proteins in the lumen of the mutant. Inhibition of TJs regulatory proteins and defects in polarity proteins also lead to multiple-lumen phenotypes *in vivo* (Schlüter & Margolis, 2009).

MNFP time-lapse data showed a problem with the attachment and spreading of olfactory placode cells during the olfactory bulb development in the *hir* mutant. The olfactory placode appeared loosely attached to the forebrain at early developmental stage and then failed to split into the bilateral placodes (Fig.4.4B and 4.5). This suggests that the loss of YAP may cause detachment of olfactory placode from the forebrain leading failure of further olfactory placode invagination into forebrain.

4.3.3 Filopodia formation between the sensory placodes and adjacent tissues is affected in *hirame* mutants

Filopodia are thin, finger-like membrane protrusions that help cells to sense their surrounding microenvironment (Mattila, *et al.*, 2008). The lens-retina inter-epithelia filopodia that provides physical tethers to coordinate the invagination of lens and retina (Chauhan *et al.*, 2009) were not observed in *hir* mutants (Fig. 4.6). In WT E9.5-10.5 mouse embryos, filopodia are formed at the interface between the lens and retina. *Cdc42* mutant mouse embryos exhibit strongly reduced filopodia protrusions associated with defective

invagination of the lens and retina. The filopodia protrusions mainly form from the presumptive lens, but some retinal originated filopodia are also observed at early developmental stage (E9.5) (Chauhan *et al.*, 2009).

Filopodia were only formed in-between the lens and the retina, mainly from the lens side in WT embryos. However in *hir* mutants, filopodia toward the retina were strongly attenuated. When the lens placode cells were detaching from the nascent retina, filopodia protrusions were not limited between the lens and retina but all the circumference of the fragmented lens placode. They were formed from the surface of the lens projecting away from the nascent retina. These findings suggest that lens cells of *hir* mutants are able to form filopodia, but somehow fail to project towards the right direction. This could be due to the dislocated lens is searching for the retina as cells use filopodia to sense their surroundings, however in this scenario, filopodia protrusions are expected to be formed around the circumference of the lens, which is not the case in *hir* mutants. The second explanation could be that the orientation of *hir* lens has changed completely, for example, the apical and basal sides of the lens have been flipped over and this can be tested by examining the localisation of the some apical markers such as aPKC and ZO-1 with fixed embryos; or injecting ASIP/PAR-3:EGFP mRNA (von Trotha *et al.*, 2006), which is also localised to the apical membrane of cells, into embryos to check the localisation.

As shown by Chauhan *et al.* (2009) the formation of lens-retina inter-epithelia filopodia requires Cdc42-signalling that regulates F-actin polymerisation. Therefore, F-actin overpolymerisation might lead to aberrant filopodia between the lens and the retina. F-actin overpolymerisation might also lead to formation of randomly projected filopodia. A similar aberrant filopodia phenotype was also observed in between the olfactory placode and the forebrain, although it remains to be investigated whether filopodia exist between the otic vesicle and hindbrain in both WT and *hir* mutants, and if so, whether aberrant filopodia protrusion could be also observed in the mutant.

4.3.4 Coordinated tissue/organ growth is affected in *hirame* mutants.

Although the appearance of multiple tissues appears to form at the right developmental time, they do not develop in a coordinated manner. In WT embryos, the noses, eyes and ears undergo coordinated morphogenesis. The olfactory pit invaginates into the forebrain along with the elongation of the forebrain. Coordinated invagination of the presumptive lens and nascent retina build the overall structure of the eye. Invagination of the optic vesicle leads to the formation of the lens vesicle and neural retina (Chow & Lang, 2001). And during ear morphogenesis, the otic vesicles invaginate into the hindbrain while the hindbrain expands laterally with the formation of brain ventricle. Coordinated morphogenesis is important for the apposing tissues comprising several organs. It is found that in zebrafish the signals from the hindbrain control the otic vesicle arrangement (Lecaudey *et al.*, 2007). The zebrafish telencephalon originates from the cells adjacent and medial to olfactory placode field (Whitlock & Westerfield, 2000). However, these morphogenetic changes do not happen in *hir* mutants, thus probably result in the failure of the invagination of the olfactory pit, lens placode and otic vesicle and the dislocation of these placode/vesicle from their adjacent tissues.

Taken together, these data suggest that YAP plays a crucial role for early sensory placodes formation and the coordinated tissue/organ morphogenesis at later stage during development. Loss of YAP leads to the dislocation of sensory tissues and aberrant inter-epithelia filopodia formation. The extracellular matrix (ECM) (Rozario & Desimone, 2011) and mechanical forces (Mammoto & Ingber, 2010) are critical for embryological morphogenesis and tissue patterning, thus it is important to check whether ECM components and mechanical forces are affected in the *hir* mutant.

Chapter 5: Yap is required for Fibronectin (FN) fibril assembly.

5.1 Introduction

5.1.1 Extracellular matrix (ECM) and Fibronectin (FN)

Extracellular matrix (ECM) is a dynamic meshwork that provides the physical microenvironment for cells. The assembly of ECM affects cell behaviours in many ways including cell migration during embryogenesis wound healing as well as tissue morphogenesis (Singh, *et al.*, 2010). The ECM also serves as a scaffold for the generation of 3D tissues (Daley *et al.*, 2008; Yamada and Cukierman, 2007).

Fibronectin (FN) matrix and the basement membrane are two major ECM networks (Schwarzbauer, *et al.*, 1999). FN is a modular protein that consists of three repeating units (types I, II, and III; Fig5.1A). FN has high-affinity binding domains for other components of the ECM including heparan, collagen and fibrin and a binding domain for specific cell membrane receptors (Buck and Horwitz, 1987; Fig5.1A).

FN has both a soluble form, which exists in blood plasma and an insoluble fibrillar form, which contributes to the ECM (Hynes, 1990). The organisation of soluble FN into fibrillar network is through direct interaction with cell membrane receptors, integrin (Hynes, 1990). The translocation of alpha5 beta1 integrin ($\alpha_5\beta_1$ integrins) transmits cytoskeleton-generated tension into extracellular FN molecules, which leads to the initiation of FN fibrillogenesis (Pankov *et al.*, 2000). The N-terminal 70-kDa region of FN protein is essential for the binding of FN to the cell membrane receptors (Fig.5.1. A; Magnusson & Mosher, 1998).

The assembly of FN matrix is a cell-mediated multi-step process. Firstly, the globular form of FN dimer binds to integrin receptors at the cell surface. Cytoskeletal proteins are then recruited by integrins and connect to actin. This increases cell tension to induce the conformational changes of FNs. The FN dimer is then pulled to expose the FN-binding sites to interact with other FN dimers. Finally, clustering of integrins and the exposure of cryptic FN binding sites leads to further FN-FN interactions, which subsequently cause further FN conformational changes and results in FN fibril formation and assembly (Fig.5.1 B; Singh, *et al.*, 2010).

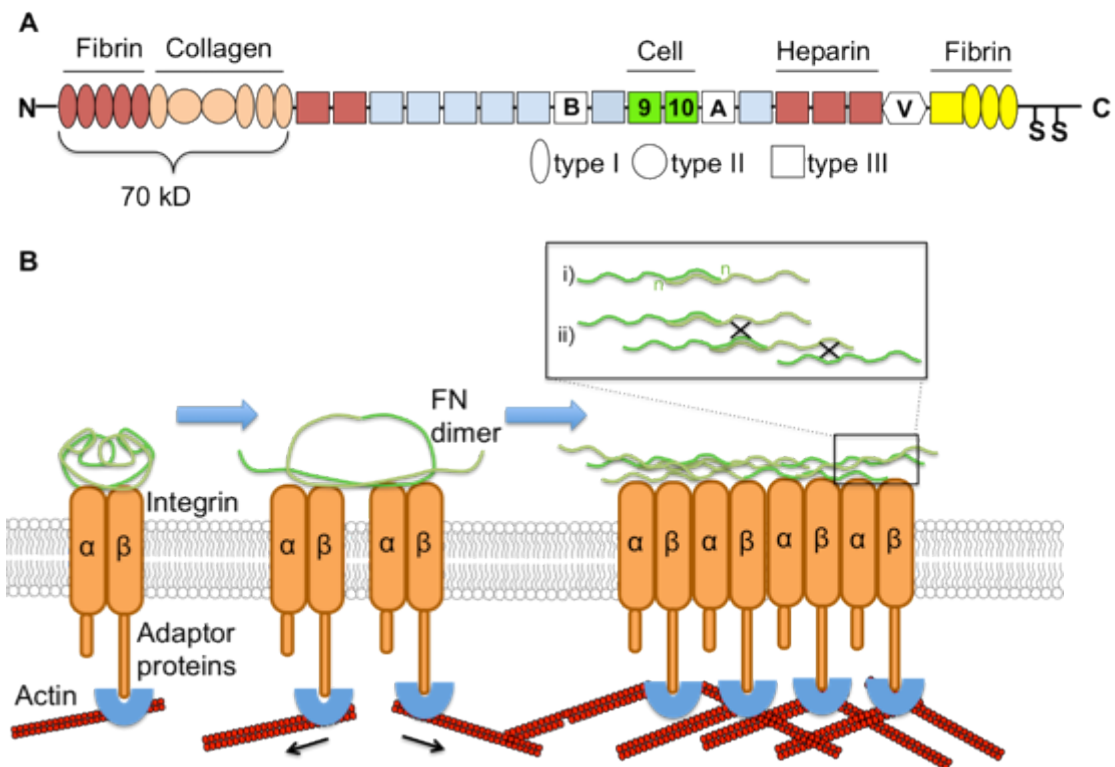


Figure 5.1 Schematic views of modular structure of Fibronectin (FN) and the process of FN matrix assembly. A, The modular structure of FN. (A) FN consists 12 type I modules (ovals), 2 type II modules (circles) and 15–17 type III modules (squares). Variably spliced extradomain A and extradomain B modules and variable sequence (V) are in white. Binding domains for fibrin, collagen, cells and heparin are highlighted with different colours; dimer forms via cysteine pairing at the C-terminus (SS). Sites of FN–FN interaction include the assembly domain in I1–5 as well as III1–2 and III12 – 14 (red). Bracket indicates the 70 kDa N-terminal fragment (Modified from Mao & Schwarzbauer, 2005). **B,** Stepwise process of FN matrix assembly. The soluble form of FN (bright and dark green) binds to α and β integrin receptors (orange). In this form, the FN cannot be assembled. Intracellular proteins such as talin and vinculin (blue) are recruited to the cytoplasmic domains of integrins connecting them to the cytoskeleton actin (red). These connections increase contractility of the cell (black arrows) causing conformational changes in the extracellular bound FN. Increasing of cell contractility pulls the FN dimer to expose the FN-binding sites that bind with other FNs. The inset box highlights interactions between single subunits of FN dimers where N is the N-terminus. (i) N-terminal mediated end-to-end interactions between FN dimers. (ii) FN matrix assembly is also mediated by the lateral association of fibrils (black crosses). Modified from Singh, *et al.* 2010.

5.1.2 The role of Fibronectin (FN) during morphogenesis

Loss-of-function studies of FN *in vivo* have been investigated in mouse, zebrafish, chick and *Xenopus*. FN loss-of-function phenotypes based on multiple animals systems including *cardia bifida* (where two separate hearts form laterally to the midline), defects in mesoderm specification, axis elongation, neural tube morphogenesis, myocardial precursor migration, yolk sac vasculature and embryonic lethal in mice embryos at E10.5 (George *et al.*, 1993; Georges-Labouesse *et al.*, 1996; Davidson *et al.*, 2006; Trinh and Stainier, 2004; Linask and Lash, 1988a; Linask and Lash, 1988b). Inhibition of FN/integrin interactions and matrix assembly in *Xenopus* leads to a failure of radial intercalation movements, which are necessary for blastocoel roof (BCR) thinning and epiboly during gastrulation (Marsden & DeSimone, 2001). Blocking FN fibril assembly can also lead to defective oriented cell division (Rozario *et al.*, 2009).

5.1.2.1 FN in heart formation

The role of Fibronectin (FN) in heart formation has been investigated in mice, chick and zebrafish. In the zebrafish *natter* (*nat*) mutant, a null mutation in the *fn1* gene, *cardia bifida* has been observed due to the failure of myocardial precursor migration (Trinh & Stainier, 2004). FN is deposited at the midline between the endoderm and endocardial precursors and laterally surrounds the myocardial precursors. Deposition of FN in the midline is necessary for the migration of myocardial precursors. The formation of adherens junctions between myocardial precursors is affected in the *nat* mutant (Trinh & Stainier, 2004). Other defects such as presence of pericardial edema (Trinh & Stainier, 2004) and a flattened hindbrain (due to the reduction in hindbrain ventricle size; Lowery *et al.*, 2010) are also observed in the *nat* mutant. Furthermore, in the *nat* mutant, apical and junctional markers α PKC and ZO-1 are found mislocated, and the organization of the myocardial precursors into polarised epithelia was disrupted (Trinh and Stainier, 2004). Low dose antisense morpholino knockdown of FN also leads to *cardia bifida* (Matsui *et al.*, 2007).

FN null mouse mutants die around E10.5 (George *et al.*, 1993). It exhibits shortened anterior-posterior body axes, defects in mesodermally derived

tissues, abnormal neural tubes formation, absence of notochord and somites, deformed heart and embryonic vessels, and impaired formation of the yolk sac, extraembryonic vasculature (George *et al.*, 1993).

When incubated in the FN-depleted medium, *cardia bifida* was also seen in chick embryos (Linask and Lash, 1988a). All these findings suggest that FN plays a crucial role in directing myocardial precursors migrating to the embryonic midline.

5.1.2.2 FN in vascular morphogenesis

In the mouse FN null mutant embryos, while the derivation and development of primitive red blood cells are normal, blood vessels do not develop. Endothelial cells, which form the blood vessels are present but are not assembled into dorsal aortae, suggesting the requirement of FN in vasculogenesis, but not erythropoiesis (George *et al.*, 1993). Later the study done by George EL *et al.*, (1997) showed that in the less severe FN null mutant (C57/BL6 background), formation of dorsal aortae is normal; however, the dorsal aortae and the heart appear collapsed and separated from the adjacent tissues, suggesting defects in lumen formation in the vessels. Collapsed blood vessel lumens could potentially be due to defective endothelial cell polarity since *in vitro* experiments using three-dimensional culture systems showed that endothelial lumen formation involves polarised movements of vacuoles followed by their fusion and requires the Cdc42-Par3-Par6-PKC ζ polarity complex (Koh *et al.*, 2008).

5.1.3 Formation of the Cuvierian ducts (CDs) and heart in medaka embryos

The first organ system to develop in the vertebrate embryo is the circulatory system, as it is required for delivery nutrients and oxygen to as well as the removal of metabolic waste from other tissues/organs, to ensure the continuing growth of the embryo (Marcelo *et al.*, 2013). Vasculogenesis, the emergence of primordial endothelial cells and blood vessels, gives rise to the heart and the vascular plexus in the embryo (Patan, 2004). The primary vascular plexus is formed from the mesodermal derived endothelial cells

(Marcelo *et al.*, 2013). Many key molecular regulators involving in vasculogenesis have been reported including vascular endothelial growth factor (VEGF), fibroblast growth factor 2(FGF2), bone morpho-genetic protein 4 (BMP4), vascular endothelial growth factor (VEGF), fibronectin (FN), N-cadherin, Integrins and *etc* (Marcelo *et al.*, 2013; Rupp & Little, 2001).

Overall morphological observations of developing medaka embryos including the formation of CDs and heart have been reported by Iwamatsu (2004). However detailed analysis of the mechanisms underlying these developmental events has not been well investigated. By using two transgenic medaka fish lines, *cmhc2:EGFP* (expressing EGFP in heart) and *fli::EGFP* (expressing GFP in the endothelial progenitors cells which form the CDs), it is possible to gain a better understanding of how the heart and CDs develop in the embryo at the single-cell level in a living embryo. Thus, these two transgenic lines are useful models for studying the defective vasculogenesis related human diseases.

The paired CDs in medaka consist of the anterior and posterior cardinal veins through which blood cells flow from the head and return from the trunk respectively (Iwamatsu, 2004). Endothelial progenitors of the CDs can be first observed on the surface of the medaka embryo's yolk at around st.18 (26 hpf) using the *fli::EGFP* transgenic fish. The forming CDs are initially observed at round st.20 (31.5 hpf). Two streams of endothelial cells that form the CDs can be seen at st.21 (34 hpf) with the anterior stream close to the hindbrain and the posterior stream near the otic placodes. The medaka CDs become easily distinguishable on the surface of the yolk from st.22 (38 hpf), and yet incomplete along the vitello-caudal vein by the time when then heart begins beating at st.24 (44 hpf). By st.25 (50 hpf), when the blood circulation starts in medaka, the CDs and carotid artery are connected by the optic plexus (Iwamatsu, 2004). The process of CDs development is summarised in Fig. 5.2. These common cardinal veins are used for yolk absorption to provide nutrients during medaka embryogenesis (Fujita *et al.*, 2006).

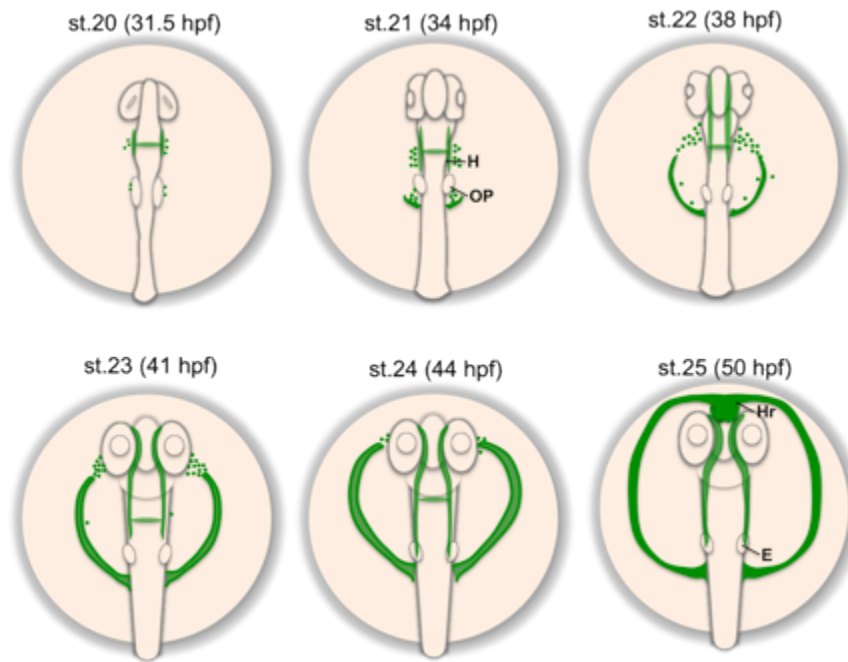


Figure 5.2 Schematic summarising Cuvierian ducts (CDs) formation in medaka embryos. At st.20 (31.5 hpf) the two endothelial cell populations (green) that give rise to CDs can be seen. By st.21 (34 hpf) the posterior population of cells extends laterally and anteriorly and by st.22 (38 hpf) meets the anterior population of cells. By st.24 (44 hpf, heart beating stage) the CDs formed a complete circuit. This vessel structure continues to increase in size and migrate anteriorly and at st.25 (50 hpf) the heart is located anteriorly of the head. H, hindbrain; op. otic placode; Hr, heart; E, ear.

In medaka, heart morphogenesis (Fig. 5.3) involves the migration of two bilateral populations of cardiac precursors (mesodermal derived endothelial cells), towards the embryonic midline. The bilateral cardiac precursors can be first identified at around st.19 (27.5 hpf) using *cmcl2:EGFP* transgenic fish. The two populations then migrate towards the embryonic midline and the heart anlage can be seen beneath the head between the midbrain and hindbrain at st.22 (38 hpf). At st.23 (41 hpf), the straight-tubed heart is formed underneath the posterior end of the nascent retina. The tubular heart elongates along the anterior-posterior plane and reaches the anterior end of the forebrain by st.24 (44 hpf), meanwhile the beating of heart starts (Iwamatsu, 2004).

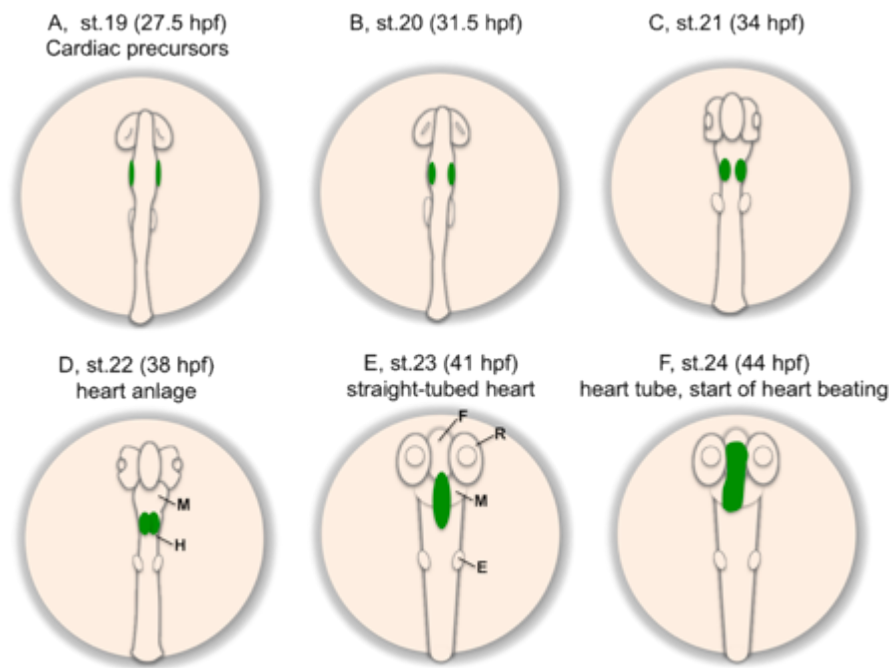


Figure 5.3 Medaka embryo heart development. A scheme-drawing showing the steps of heart development in medaka embryo. By st.19 (27.5 hpf), cardiac precursors (originated from the anterior lateral plate mesoderm) are organised in two bilateral sheets (green) (A). The two populations of cardiac precursor cells migrate towards the midline and fuse to form the heart anlage (B-E). The tubular heart then elongates along the anterior-posterior axis (F). Heart beating starts at st.24 (44 hpf). E, ear; F, forebrain; H, hindbrain; M, midbrain; R, retina.

5.1.4 FN and somitogenesis

It has been reported that FN is necessary for initial somite boundary formation and later maintenance (Julich *et al.*, 2005; Koshida *et al.*, 2005). FN enriches at each somite boundary after the formation of the morphological boundary. This accumulation at somite boundaries is Integrin α_5 -dependent (Koshida *et al.*, 2005). In the *fn* knock-down embryos, somite boundary cells are also round and a randomised position of centrosomes was observed in the *fn* morphants (Koshida *et al.*, 2005). Further zebrafish study by Snow, *et al.*, 2008 showed that muscle fiber in *fn1+3* knock-down embryos are less organised and the fiber lengths in the fast and slow-twitch muscle are uncoupled. During later developmental stages, *fn* knockdown affects anterior somite formation and/or maintenance, however, both patterning and somite boundary formation in posterior somites remain relatively normally (Snow, *et*

al., 2008). Jülich *et al.*, 2009 showed that in zebrafish, Eph/Ephrin signalling regulates the proper spatiotemporal deposition of fibronectin matrix during somitogenesis via clusters of $\alpha 5\beta 1$ integrins along cell boundaries and de-represses integrin trans-inhibitory signals.

5.1.5 Aims

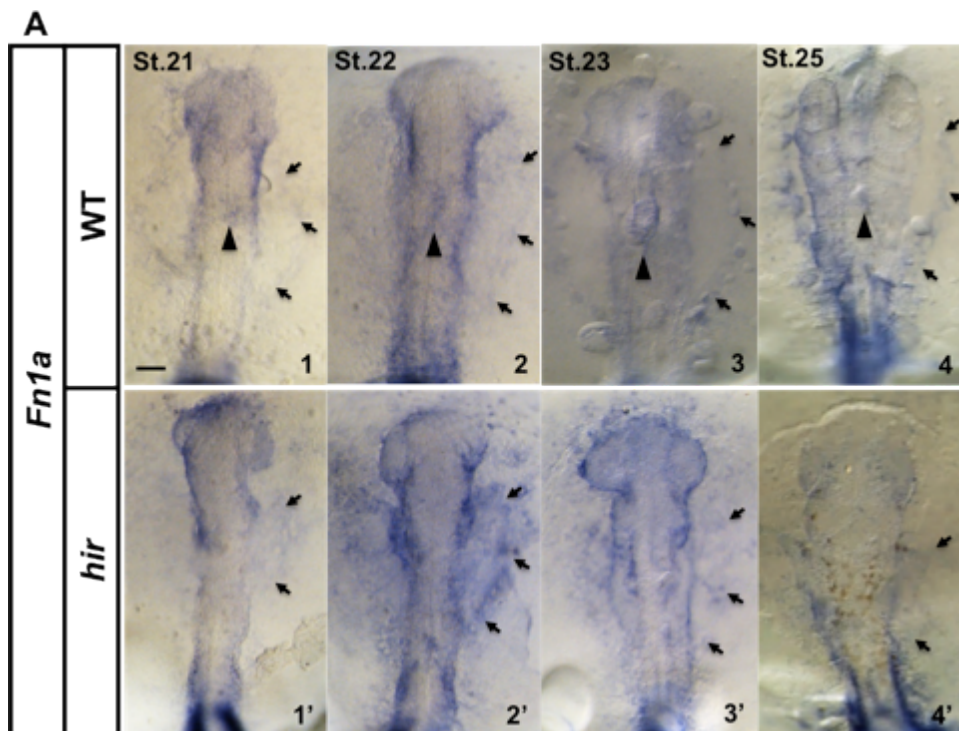
Coordinated tissue/organ growth is affected in *hirame* mutants as outlined in previous chapters. The extracellular matrix (ECM) and mechanical forces are critical for embryological morphogenesis and tissue patterning, therefore it is important to check whether ECM components and mechanical forces are affected in the *hir* mutant. Since fibronectin (FN), a protein organised into a fibrillar network through direct interactions with cell surface receptors, and an abundant and ubiquitous component of ECM, activity and assembly of FN were examined.

5.2 Results

5.2.1 Abnormal Fibronectin (FN) localisation is observed during heart and Cuvierian ducts (CDs) formation in *hirame* mutants

Since FN is required for the heart formation and vasculogenesis *in vivo* (George *et al.*, 1993; Trinh & Stainier, 2004), FN expression was investigated in *hir* mutants. Whole-mount *in situ* hybridisation (ISH) of *Fn1a* and *Fn1b* and whole-mount FN1a+b immunohistochemistry (IHC) were performed.

Fn1a transcripts were detected in the tail bud, somites and the CDs (Fig.5.4A arrows). At early stages (st.21-22; 34-38 hpf), *Fn1a* transcripts were enriched at the lateral sides of the embryo bodies where the endothelial progenitor cells derived from (Fig.5.4A 1-2, 1'-2'). The transcripts of *Fn1a* along the lateral sides then started to fade after st.23 (41 hpf) (Fig.5.4A 3-4, 3'-4'). Deposition of FN transcripts was seen in the midline in WT embryos (Fig.5.4A 1-4, black arrow heads).



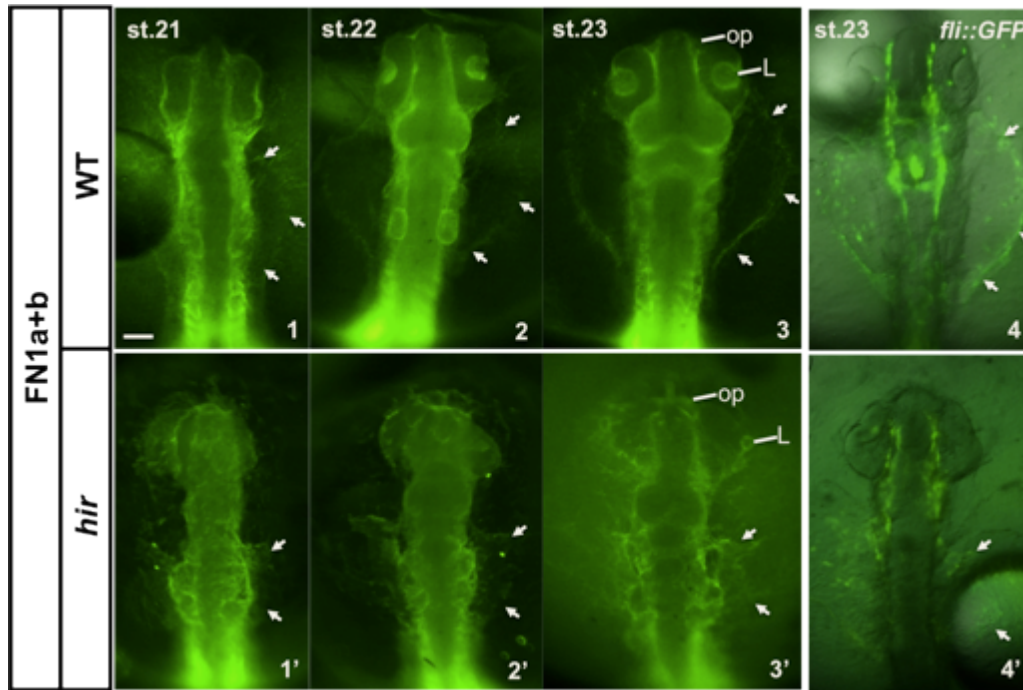
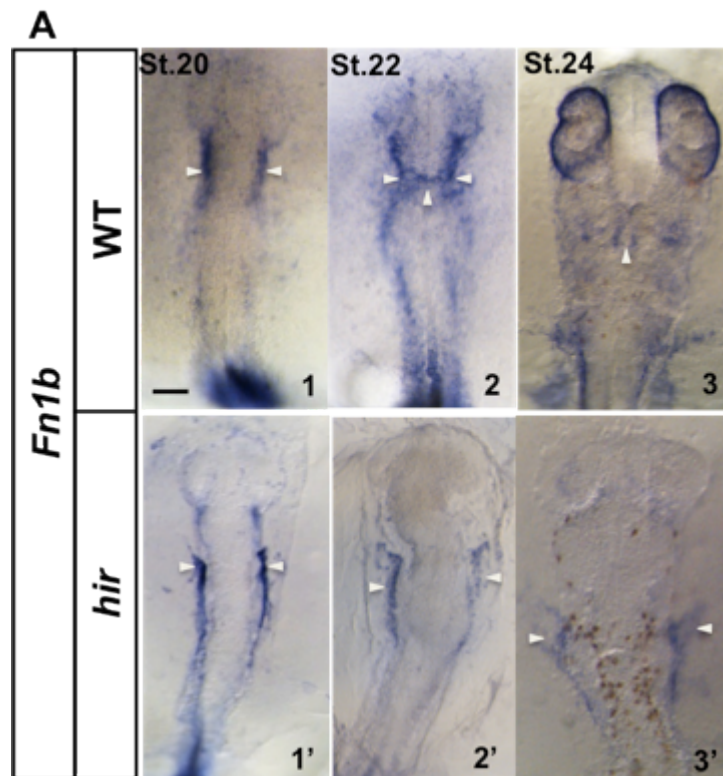


Figure 5.4 Aberrant fibronectin deposition is observed during the formation of Cuvierian ducts (CDs) in *hirame* mutants. A, Expression pattern of *Fn1a* during medaka embryogenesis. Stages are indicated top left. Dorsal views of all images. Arrowheads indicate the FN deposition in the midline; arrows indicate the FN deposition in CDs. **B,** (1-3, 1'-3') Dorsal views of whole-mount FN1a+b antibody stained (green) embryos at stages indicated top left. FN1a+b staining is seen surrounded epithelial tissues/organs such as lenses, olfactory pits and CD. L, lens; op, olfactory pit. (4, 4') Dorsal views of st.23 (41 hpf) medaka Tg(*fli::EGFP*) embryos that express EGFP in endothelial cells. Arrows indicate the developing Cuvier's duct. Scale bar = 40 μ m.

Fn1b transcripts was detected in the notochord and somite, and enriched along the lateral sides of the embryo bodies from where the cardiac precursors derived (Fig.5.5A 1, 1' arrowheads). At st.22 (38 hpf), the *Fn1b* transcripts were also seen in the midline where the cardiac precursors fused in WT embryos. At st.24 (41 hpf), the lateral expression of *Fn1b* was reduced but accumulated in the midline where the heart tube formed (Fig.5.5A 3). In order to examine whether the localisation of FN1a+b IHC correlated with the developing heart, different optical sections of CDs were made. Again accumulation of FN transcripts was seen along the lateral side of embryo body at st.20 (31.5 hpf) (Fig.5.5B1, 1'). At st.22 (34hpf), the distribution "bridge" like FN transcripts was detected at the midline (Fig.5.5B 2) and a

strong deposition of FN transcripts was observed in the position correlated to the ventricular myocytes at st.24 (44hpf) (Fig.5.5B 3-4). However, neither mRNA *Fn1b* expression nor the localisation of FN1a+b antibody was seen in the midline in the *hir* mutants, instead, strong accumulation of FN was remained alongside laterally of the embryo bodies (Fig.5.5A 1'-3'; Fig.5.5B 1'-3'). At st.24 (hpf), the FN signal was increased bilaterally where the two population of cardiac precursors were trapped in the *hir* mutant (Fig.5.5B 3'-4').

Similar results were also observed by the whole-mount FN1a+b protein staining (Fig.5.4B). FN was mainly localised around epithelial tissues/organs such as ears and lenses, the boundary of somites, and the CDs (Fig.5.4B; Fig.5.5 B). FN staining was also observed in the endothelial cells that form the CDs laterally to the embryo bodies in *hir* mutants, however, the FN deposition in the midline of the body was reduced (Fig.5.4A 1'-4'). The localisation of FN correlated with the developing CDs in both WT and *hir* mutants (Fig.5.4B 3-4, 3'-4').



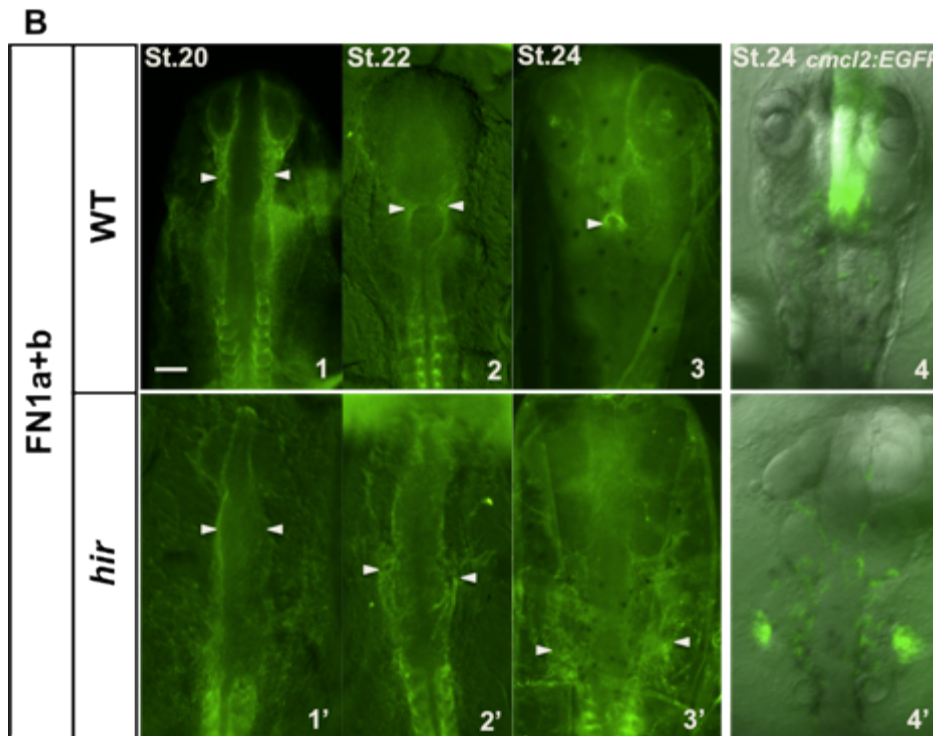


Figure 5.5 Aberrant Fibronectin deposition is observed during the heart formation in *hirame* mutants. **A**, Expression pattern of *Fn1b* during medaka embryogenesis. Stages are indicated top left. Dorsal views of all images. **B**, (1-3, 1'-3') Dorsal views of whole-mount FN1a+b antibody stained (green) embryos at stages indicated top left. FN1a+b staining is observed surrounding epithelial tissues/organs such as cardiac precursors and the boundary of smoites. (4, 4') Dorsal views of st.24 (44 hpf) medaka Tg(*cmcl2::EGFP*) embryos that express EGFP in cardiac progenitor cells. Arrowheads indicate the developing heart in the embryos. Scale bar = 40 μ m.

5.2.2 *hirame* mutants exhibit aberrant Fibronectin (FN) assembly

FN mediated integrin signaling involves assembly of FN fibrils. Since whole-mount immunohistochemistry (IHC) identified aberrant FN assembly in *hir* mutants, detailed analysis of FN assembly was carried out during development.

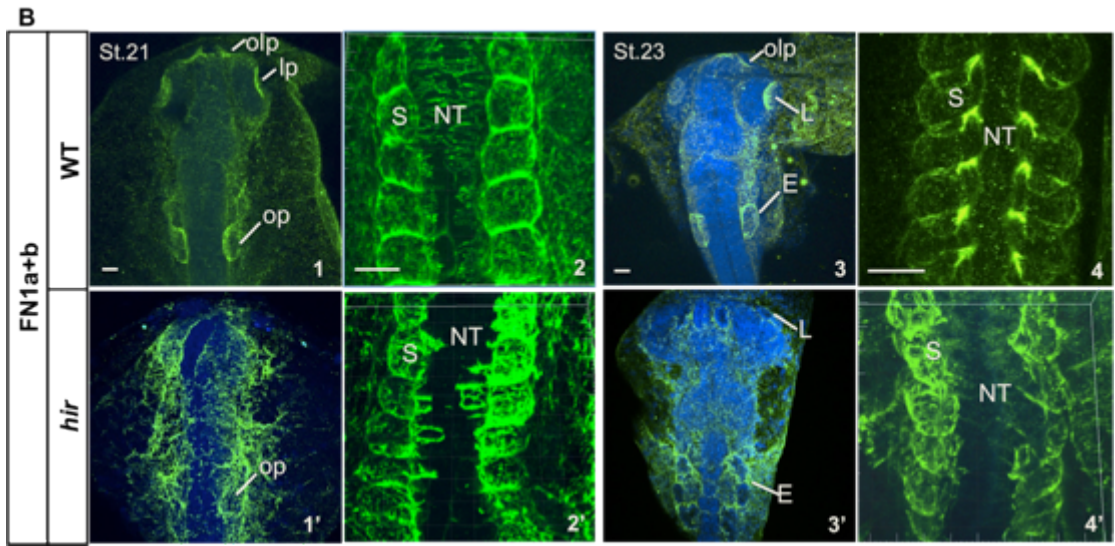
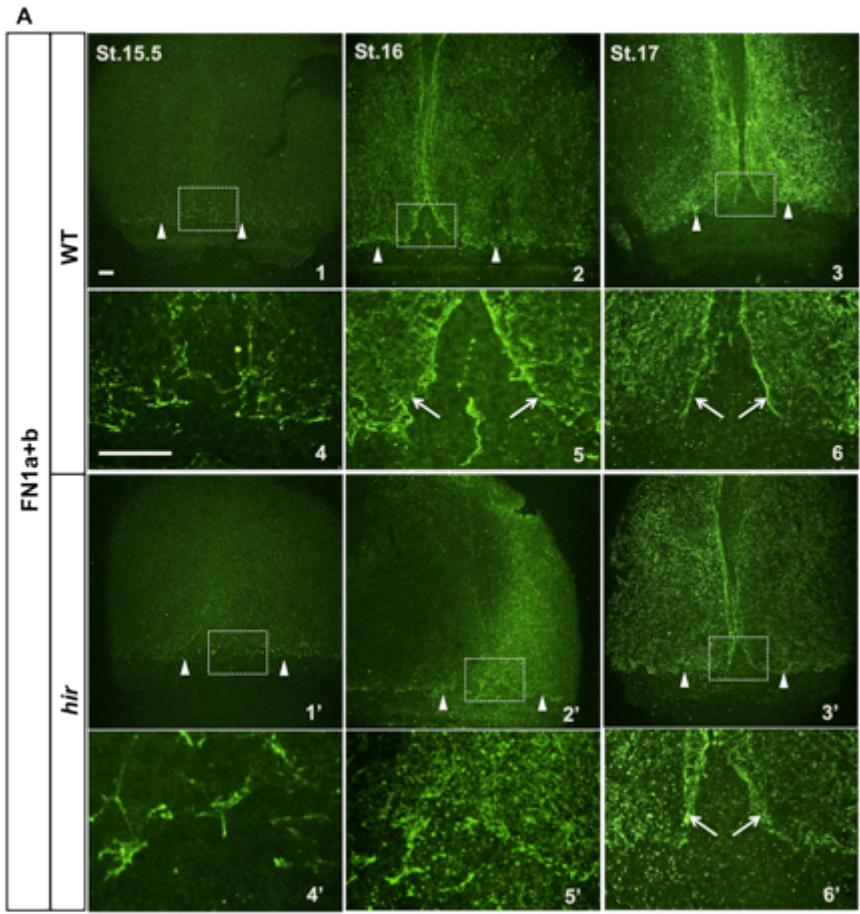
FN fibrils could be detected as early as mid-gastrulation stage. At st.15.5 (19 hpf), FN fibrils were observed at the edge of epiboly in WT embryos (Fig.5.6A 1, 4). In *hir* mutants (Fig.5.6A 1', 4') normal FN fibrils were strongly reduced and instead longer and thicker FN fibrils were observed. During epiboly, FN fibrils became denser in blastoderm and enriched at the edge of blastoderm and at the boundary of embryonic shield in WT embryos (Fig.5.6A 2-3, 2'-3').

In *hir* mutant embryos many punctated FN and occasionally long FN fibrils were observed but such enrichment of FN fibrils could not be seen at st.16 (Fig.5.6A 2'-3', 5'-6').

During organogenesis, strong FN deposition could be seen at the interspace between the lens placode/lens and nascent retina (Fig.5.6B 1, 3 and Fig.5.8B 1, 2), the olfactory placode and the forebrain (Fig.5.6B 1,3), the boundary of somites and surrounding the ear (Fig.5.6B 2, 4). Fine mesh-like FN fibrils were also observed covering the WT neural tube at st.21 (34 hpf) (Fig.5.6B 2). Strikingly, very aberrant FN fibrils were observed in *hir* mutants (Fig.5.6B 1'-4'). The strong localisation of FN at the interspace between the lens and retina, the olfactory and forebrain was lost in the mutant (Fig.5.6B 1', 3'). FN fibrils became strongly aberrant at somite boundaries and surrounding ears (Fig.5.6B 1'-4'). Almost no fine FN fibrils were observed covering the neural tube in *hir* mutant at st.21 (34 hpf), instead, thicker and longer FN fibrils were distributed sparsely (Fig.5.6B 2').

Since FN assembly depends on actomyosin contraction (Rossier *et al.*, 2010), F-actin formation was analysed by phalloidin staining. Abnormal and irregular F-actin (phalloidin staining) was observed in the *hir* mutant by 3D rendering (Fig.5.6C 2, 2'). Cells in the epithelial enveloping layer (EVL) had pronounced F-actin localisation at the cell boundaries in both WT embryo and *hir* mutant (Fig.5.6C 1, 2). While periderm cells in WT embryos were elongated, those in the *hir* mutant were irregular and less elongated (Fig.5.6C 1, 2). Frontal optical sections showed strong disorganised F-actin localisation in EVL cells in the *hir* mutant (compare Fig.5.6C 1' and 2'). In the WT embryo, periderm cells elongated and tightly covered the ear, whereas in the *hir* mutant periderm cells were loosely hanging covering the ear (Fig.5.6C 1', 2').

Although the FN assembly was affected in *hir* mutants, the total FN protein levels remained comparable to the WT embryo as indicated by Immuno blotting analysis performed at earlier (st.17, 25 hpf) and later (st.23, 41 hpf) stages of development (Fig.5.6D). This further supports the notion that FN assembly rather than its production is affected in *hir* mutants.



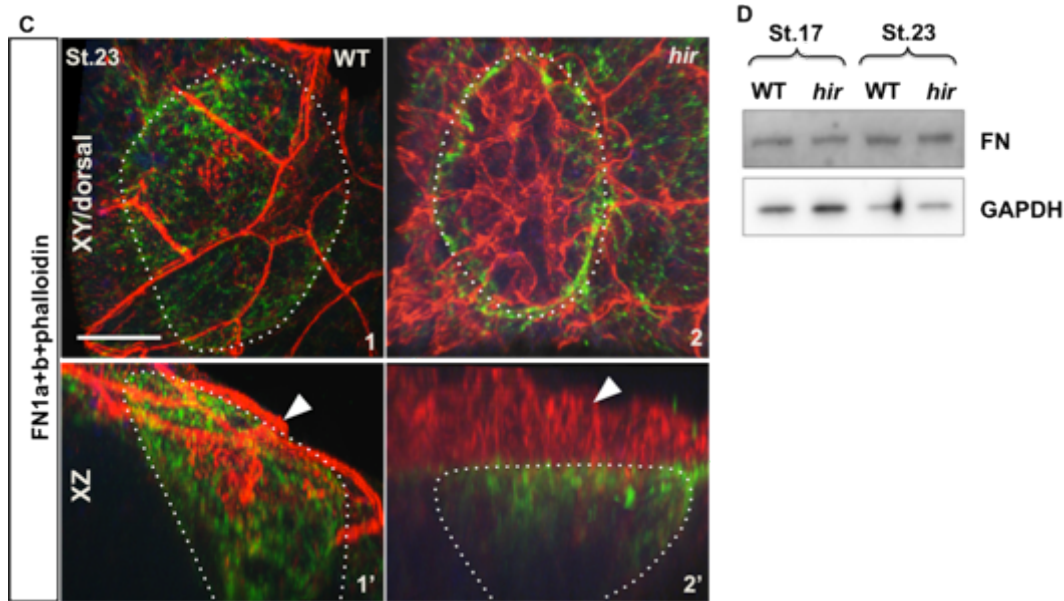


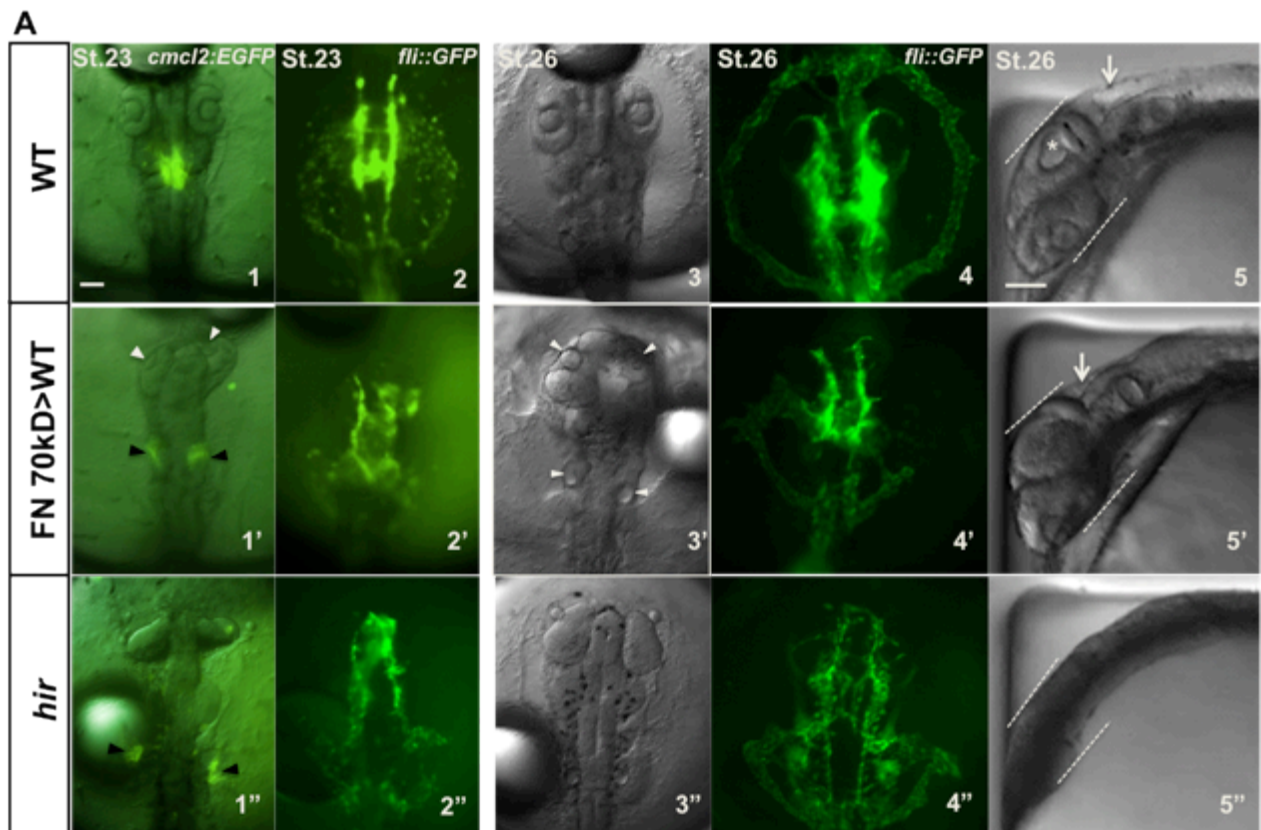
Figure 5.6 Fibronectin fibril assembly is disrupted in *hirame* mutants. **A**, Dorsal views of whole-mount FN1a+b antibody stained (green) embryos at stages indicated top left. Arrowheads indicate the edge of blastoderm. Arrows indicate the boundary of embryonic shield (body). (4-6, 4'-6') show magnified views of boxes in (1-3, 1'-3') respectively. **B**, Dorsal views of whole-mount FN1a+b antibody stained (green) embryos. Stages are indicated top left. Blue staining is nuclear Topro3. E, ear; L, lens; lp, lens placode, NT, neural tube; op, otic placode; olp, olfactory placode; R, retina; S, somite. **C**, (1-1') Dorsal views of FN (green) and phalloidin (red, F-actin) double stained embryos at st.23 (41 hpf). (2-3') XZ (frontal optical section) views show the abnormal distribution of F-actin (arrowheads) in the *hir* mutant. Dotted lines outline the ear. Arrowheads indicate the strong F-actin localisation in the periderm. **D**, Immuno-blotting shows comparable FN protein levels between WT embryos and *hir* mutants. Data was kindly provided by Dr. Shoji Hata. Scale bar (A, B)= 40 μm ; (C)= 50 μm .

5.2.3 Fibronectin (FN) assembly defects result in tissue dislocation but not flattening of tissues

Since FN plays important roles for tissue morphogenesis and cell migration and normal FN fibrils were strongly reduced in *hir* mutants, whether inhibition of FN assembly in WT embryos can lead to *hir* phenotype was examined. mRNA encoding N-terminal 70kDa fragments of medaka FN (FN 70kD), which act in a dominant negative manner to block FN assembly was injected into WT embryos at 1-cell stage (1 hpf). Injection of 70kD FN mRNA into WT

embryos mimicked most of the *hir* phenotypes including the dislocation of lenses and ears (Fig.5.7A 1', 3'), the truncated Cuvierian ducts (CDs) (Fig.5.7A 2', 4'), *cardia bifida* (Fig.5.7A 1' black arrowheads), but not the flattening of tissues (Fig.5.7A 5'5''; Fig.5.7B; Fig.5.7C).

70kD FN mRNA injected WT embryos also caused brain deformation such as missing one side of the eye (Fig.5.7B 2'), very disorganised brain tissue alignment (Fig.5.7B 1'), missing of the midbrain ventricle (Fig.5.7A 5, 5') and reduced dorsoventral height of the hindbrain ventricle (Fig.5.7A 5, 5' arrow), similar defects observed in FN1 medaka mutants (unpublished results). The lumen formation in the ear and gut was affected in FN 70kD injected WT embryos (Fig.5.7C). Both the ear lumen and the gut lumen appeared much bigger and less round (Fig.5.7C 1').



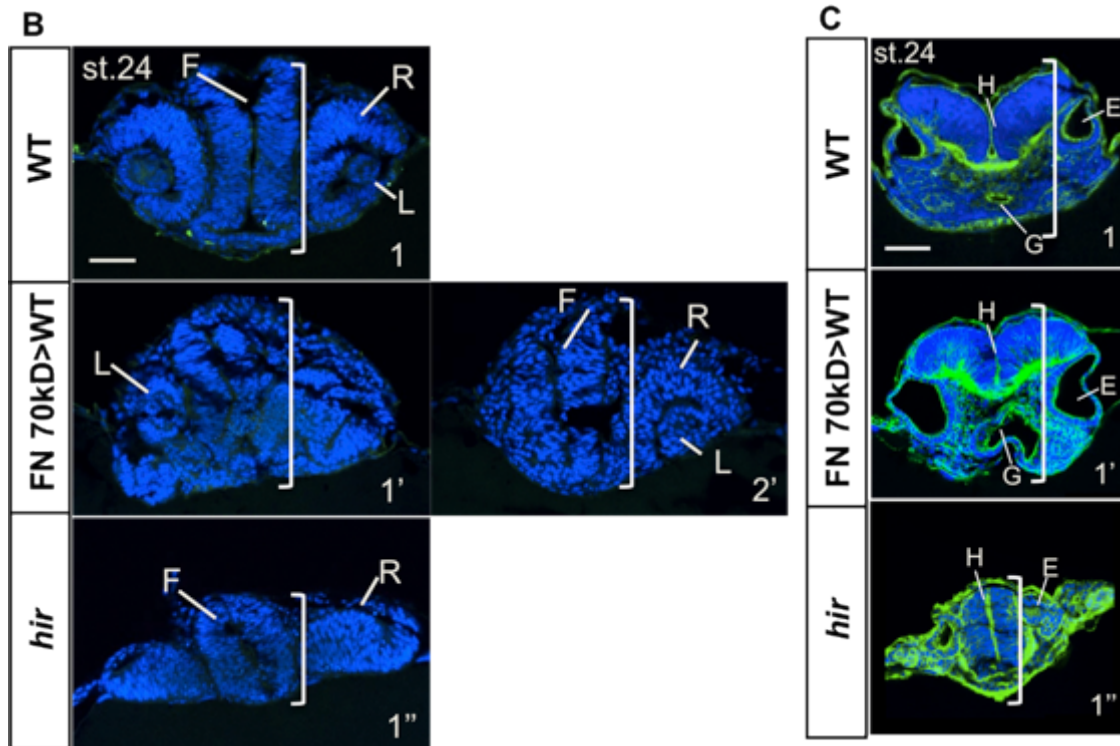


Figure 5.7 Blockage of FN assembly caused tissue dislocation but not flattening of tissues. Stages are indicated top left. **A**, 70kD FN mRNA injection in WT embryos mimicked the defects seen in the CDs and heart of *hir* mutants. Dorsal views of live Tg(*cmhc2:EGFP*) (1-1"), Tg(*flii:EGFP*) (2-2", 4-4") transgenic embryos expressing EGFP in heart and endothelial precursors respectively. Dorsal views (3-3") and lateral views (5-5") of live embryos at st.26 (54 hpf). Dotted lines indicate the thickness of the brain. Arrows indicate the hindbrain ventricle. Black arrowheads indicate the *cardia bifida*. Asterisk shows the midbrain ventricle. **B**, 70kD FN mRNA injected WT embryos showed strongly disorganised brain morphology. Transverse sections of st.24 (44 hpf) WT, *hir* and FN 70kD injected WT embryos at forebrain level stained with TO-PRO-3 (blue, nucleus). R, forebrain; L, lens; R, retina. **C**, Transverse sections of st.24 (44 hpf) WT, *hir* and 70kD FN mRNA injected WT embryos at the hindbrain level stained with phalloidin (green, F-actin) and TO-PRO-3 (blue, nucleus). E, ear; H, hindbrain; G, gut. Brackets indicate the thickness of the brain. Scale bar = 50 μm.

Whole-mount FN antibody staining confirmed the blockage of FN assembly in the FN 70kD injected WT embryos (Fig.5.8A 3). At st.17 (25 hpf), unlike WT embryo (Fig.5.8A 1) only FN puncta were observed in 70kD FN mRNA injected embryos (Fig.5.8A 3), and this persisted throughout the development

at stage examined. FN fibrils network in *hir* mutant appeared less tight (Fig5.8A inserts in 1 and 2).

At st.22 (38hpf) when lens placode invaginates into the retina, fine FN fibrils were observed at the interspace between the lens and retina in WT embryo (Fig.5.8B 1). In the FN 70kD injected WT embryo, globular FN puncta were confirmed between the lens and retina (Fig.5.8B 3) as a result of blockage of FN assembly. The *hir* mutant had reduced normal FN fibrils but instead punctated FN as well as thicker and longer FN fibrils at the interspace between the lens and retina (Fig.5.8B 2).

These results suggest that FN assembly defects was sufficient to cause tissue dislocation but not tissue flattening. Consequently, we wanted to question what causes tissue flattening in *hir* mutants.

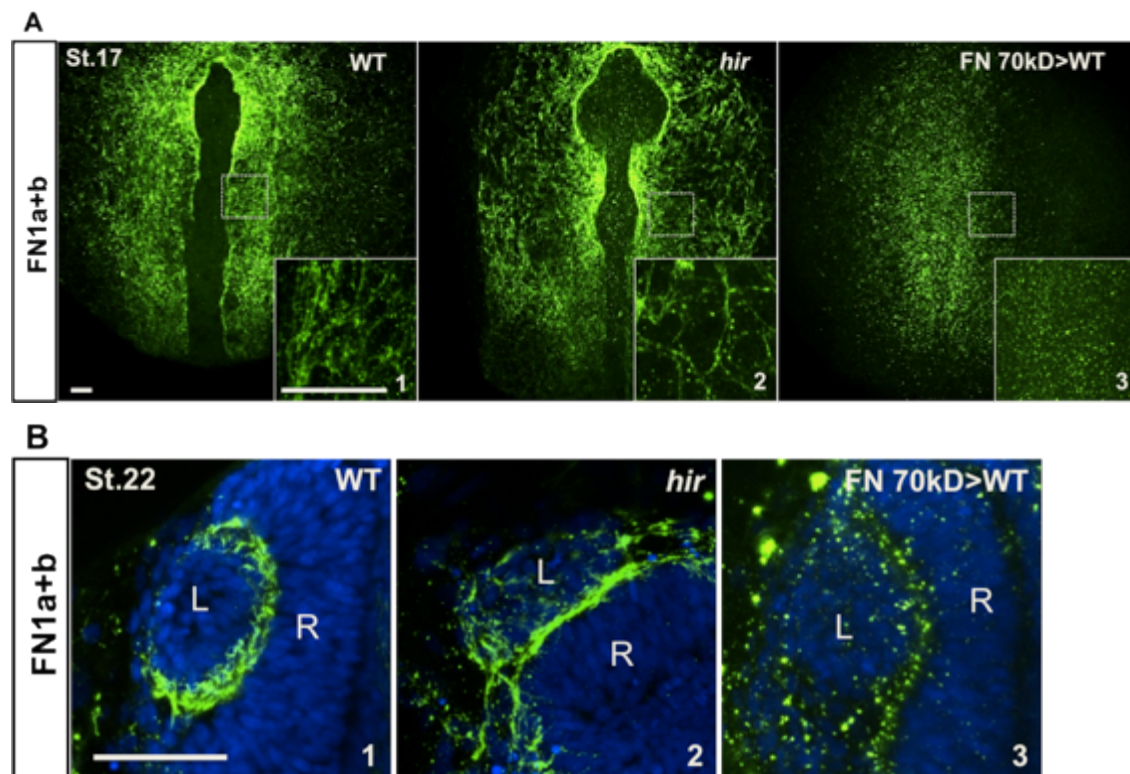


Figure 5.8 Fibronectin assembly is completely blocked in FN 70kD injected WT embryos. All views are dorsal with anterior up. Stages are indicated top left. **A**, Whole-mount FN antibody (green) staining confirms the blockage of FN assembly in FN 70kD injected WT embryos. Insets show magnifications of boxed regions. **B**, FN antibody staining (green) of corresponding st.22 (38 hpf) embryos in the region of the eye shows aberrant FN fibrillogenesis in *hir* (panel 2) and a loss of FN fibrils in FN

70kD injected WT embryos (panel 3). Blue staining is nuclear Topro3. L, lens; R, retina. Scale bar = 40 μ m.

5.2.4 Tissue polarity seems unaffected in *hirame* mutants while oriented cell division is affected

FN is essential for cell polarity during heart morphogenesis in zebrafish (Trinh and Stainier, 2004). In the absence of FN, components of tight junction and adherens junction complexes are downregulated and dislocalised. The importance of fibrillar Fibronectin (FN) to maintain cell polarity via oriented cell division has been shown in *Xenopus* (Rozario *et al.*, 2009). Randomised cell division plane in the blastocoel roof (BCR) was also observed when FN fibril assembly was blocked in *Xenopus* (Marsden & DeSimone, 2001). Since FN fibril assembly is affected in *hir* mutants, cell polarity and the oriented cell division needed to be assessed to test whether cell adhesion defects and/or change of cell division plane could lead to the tissue flattening.

The localisation of three cell adhesion proteins including atypical protein kinase C (aPKC) (adherens junctions), zonula occluden-1 (ZO1) (tight junction), and pan-cadherin in *hir* mutants were analysed by immunohistochemistry (IHC). Localisation of these proteins was found at the apical side of tissues (forebrain and retina) in both WT embryos and *hir* mutants at st.23 (41 hpf) (Fig.5.9 1-3, 1'-3').

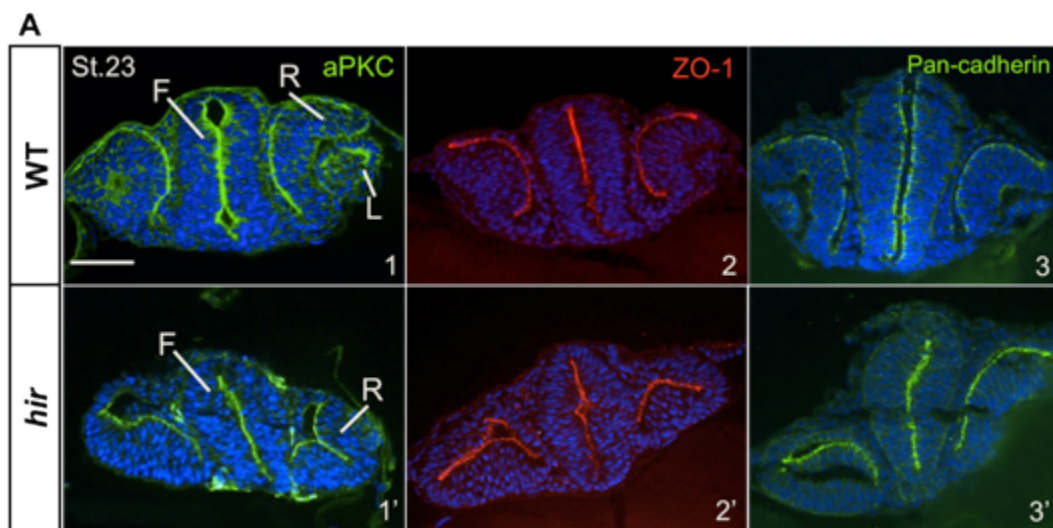


Figure 5.9 Apical protein expressions remain largely normal in *hir* mutants. IHC of junction proteins aPKC (1, 1'), ZO-1 (2, 2') and pan-cadherin (3, 3') in WT embryos

and *hir* mutants at st.23 (41 hpf). Transverse sections of all images. F, forebrain; L, lens; R, retina. Scale bar = 50 μ m

Oriented cell division plane was examined in the lens placodes at st.21 (34 hpf), when the lens placodes starts to round up. MNFP injected embryos were used to visualise cell membrane and nucleus. Since it has been shown that dividing cells often rotate as mitosis proceeds prior to telophase (Tibber *et al.*, 2004), the division angle was measured for cells in telophase. The lens placode-retina boundary (PRB) was used here as a reference plane against which the division angle of lens cells was measured. In WT embryos, the division happening in lens placodes both parallel (Fig.5.10A 1) and perpendicular (Fig.5.10A 2) relative to the PRB was observed, whereas only parallel division angle was observed in *hir* mutants (Fig.5.10A 1' and Fig.5.10B). Similar disturbed oriented cell division was seen in other epithelial tissues including retina, ear and neural tube (Sean Porazinski, unpublished results).

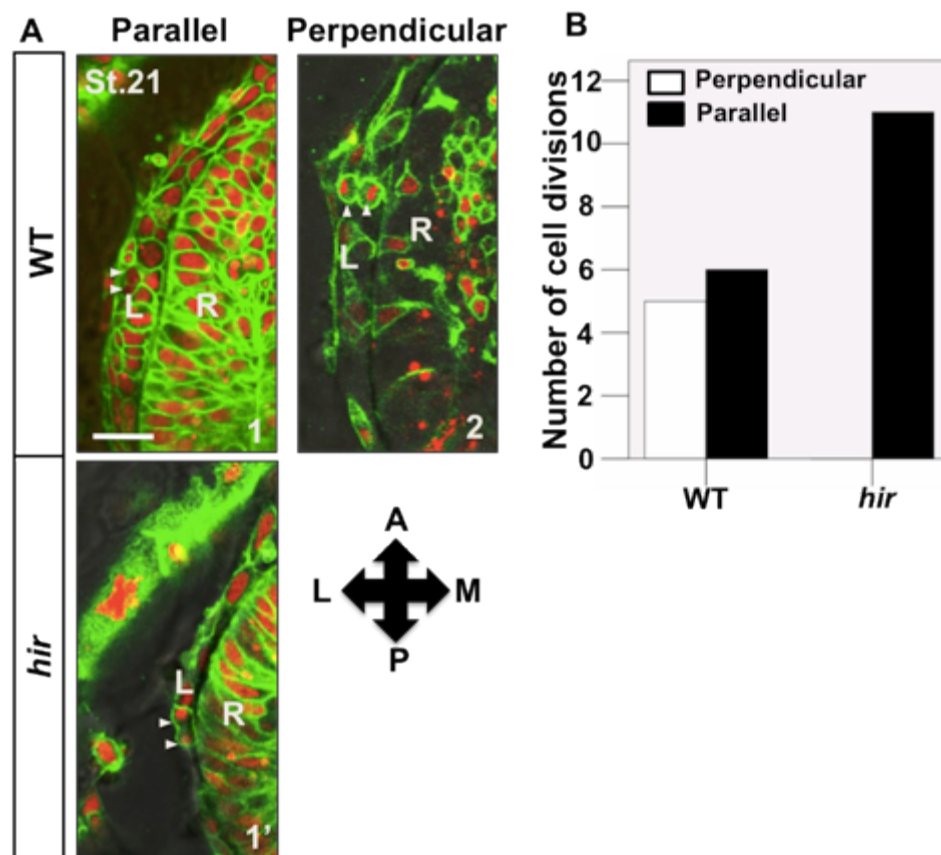


Figure 5.10 Oriented cell division is affected in the *hirame* lens placode. A, Frames from confocal time-lapse imaging. Dorsal views of all images. In the WT lens

placode neuroepithelial (NE) cells divide both parallel and perpendicularly to the retina margin whereas only parallel division is observed in *hir* mutant. Arrowheads indicate dividing cells in MNFP labelled embryos. L: lens; R: retina. **B**, Quantification of NE cell division in the lens placode of WT embryo and *hir* mutant at st.21 (34 hpf). Numbers of embryos are shown in parentheses. 11 dividing cells were analysed in both WT embryos (n=3) and *hir* mutants (n=7). A: anterior; P: posterior; M: medial; L: lateral. Scale bar =10µm. Panels A and B in collaboration with Sean Porazinski.

5.2.5 Fibronectin-integrin signaling is affected in *hirame* mutants

FN fibril assembly is initiated by FN-integrin interactions when FN binds to integrin receptors (Marsden & DeSimone, 2001). As FN fibrillisation defects were observed in *hir* mutants, whether FN-integrin signaling is affected in *hir* mutants was examined.

Since Integrin $\alpha_5\beta_1$ (*itg\alpha_5\beta_1*) is the major receptor responsible for initial FN matrix assembly (Pankov *et al.*, 2000), integrin- β_1 (*itg-\beta_1*) was examined in the mutant by immunohistochemistry (IHC) staining sections of the localisation of integrin protein. Localisation of *itg-\beta_1* was seen on the basal side of presumptive lens in WT embryos at st.21 (34 hpf) (Fig.5.11A 1 arrowheads). Later, during invagination of lens, strong accumulation of *itg-\beta_1* was seen between the lens and retina in WT embryos (Fig.5.11A 2, 3 arrowheads) and the interspace between the retina and forebrain (Fig.5.11A 2, 3, arrows) at st.23-24 (41-44 hpf). Similar FN localisation was also observed in WT embryos (Fig.5.11C 1-3). Strong accumulation of *itg-\beta_1* was seen in the lens of WT embryos by *in situ* hybridisation (Fig.5.11B 2-3).

In *hir* mutants, however, *itg-\beta_1* localisation was much reduced at st.21 (34 hpf) (Fig.5.11A 1' and Fig.5.11B 1'), though weak localisation was seen on reattached lens at st.24 (44 hpf) (arrowheads, Fig.5.11A 3' and Fig.5.11B 3'). The localisation of FN was also reduced at the interspace between epithelial tissues (compare Fig.5.11C 1-3 and 1'-3') and during invagination of lens (st.23-24, 41-44 hpf), only weak localisation was observed at the lens (Fig.5.11C 3' arrowheads).

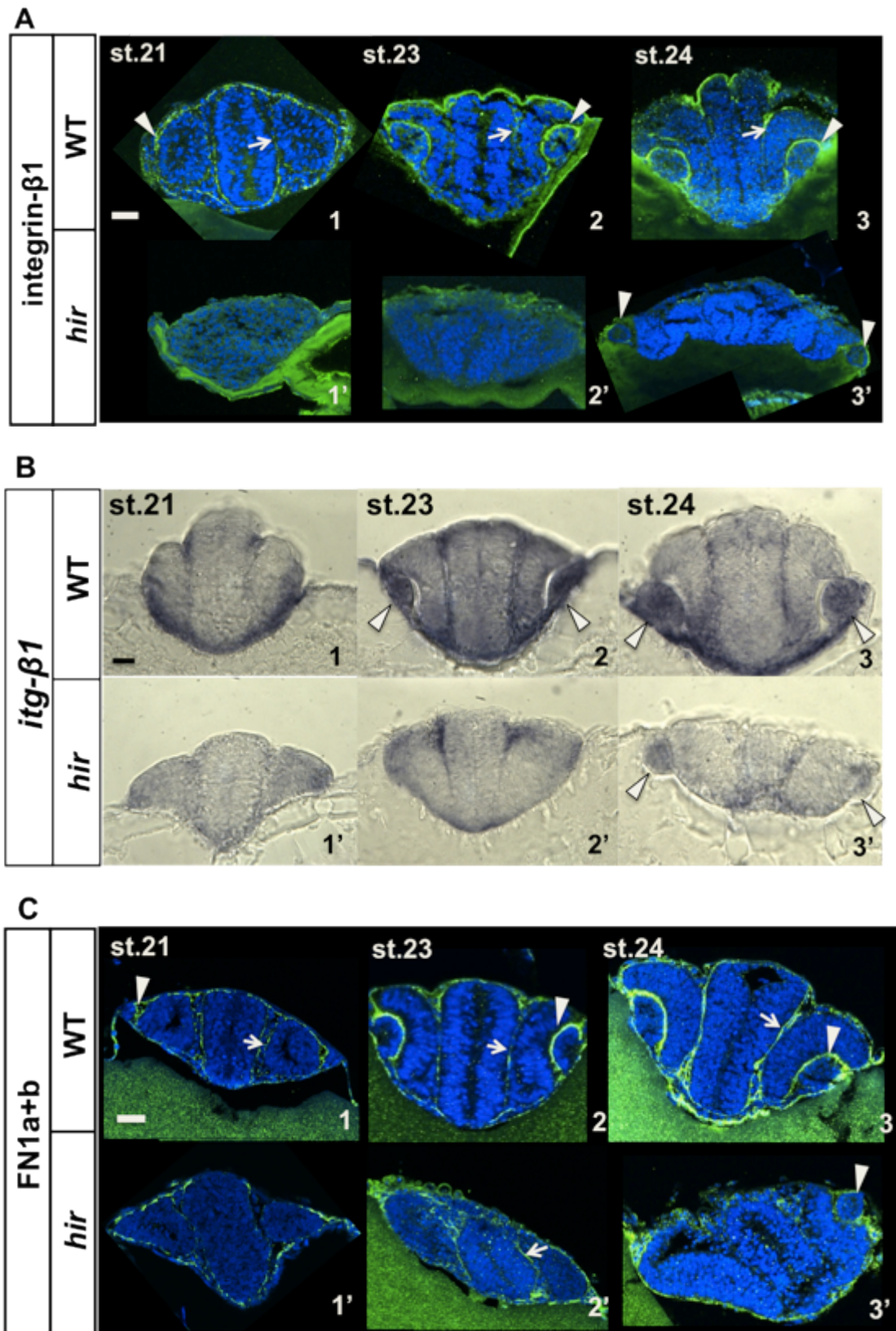
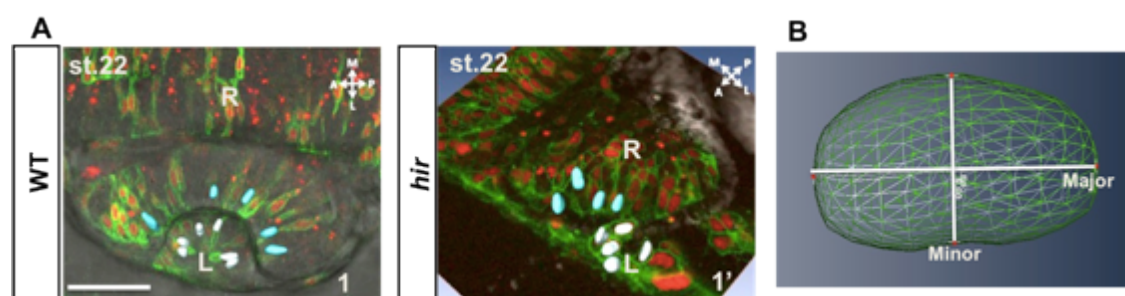


Figure 5.11 Fibronectin-integrin signalling is disrupted in *hirame* mutants. **A**, Transverse sections of Integrin- β_1 (*itg- β_1*) antibody stained (green) embryos at stage indicated top left. *Itg- β_1* between the lens and retina (arrowheads) and the retina and

forebrain (arrows) is reduced in *hir* mutants. **B**, Transverse sections through forebrain area. Expression of *itg-β₁* is strongly localised in lenses (arrowheads) of WT embryos. **C**, FN1 antibody staining (green) of WT embryos and *hir* mutants at stages indicated top left. Arrows show the localisation of FN in between the retina and forebrain while the arrowheads show the localisation of FN in between the lens and retina. Blue staining is nuclear Topro3. Scale bars = 30µm.

5.2.6 Tissue tension appears reduced in *hirame* mutants

Tissue tension has been known to be required for the assembly of FN fibrils (Dzamba BJ, *et al.*, 2009), especially for the exposure of the FN-binding sites (Zhong, G, *et a.*, 1998). Since nucleus shape is known to correlate with tissue tension (Sims JR, *et al.*, 1992), nucleus shape was examined in *hir* mutants from st.20-22 (31.5-38 hpf). 3D rendering of nucleus shape was performed based on confocal real-time imaging data, as demonstrated in Fig.5.12A. The nuclei appeared to be rounder in both lens and retina of *hir* mutants (Fig.5.12A 1, 1'). Quantification analysis of nucleus shape was carried out. Both the longest (major) and shortest (minor) axes of one cell were measured, as shown in Fig.5.12B. The mean ratio of the longest and shortest axes was calculated. The rounder the nucleus is, the closer the ratio to 1. In WT embryos, the nuclei elongated along development (Fig.5.12C), suggesting an increase in the tissue tension. In *hir* mutants, such elongation of nucleus can barely be seen (Fig.5.12C), suggesting that tissue tension might be reduced in *hir* mutants. Similar tissue tension reduction was also observed in the neural tube of the mutant (Porazinski *et al.*, unpublished data).



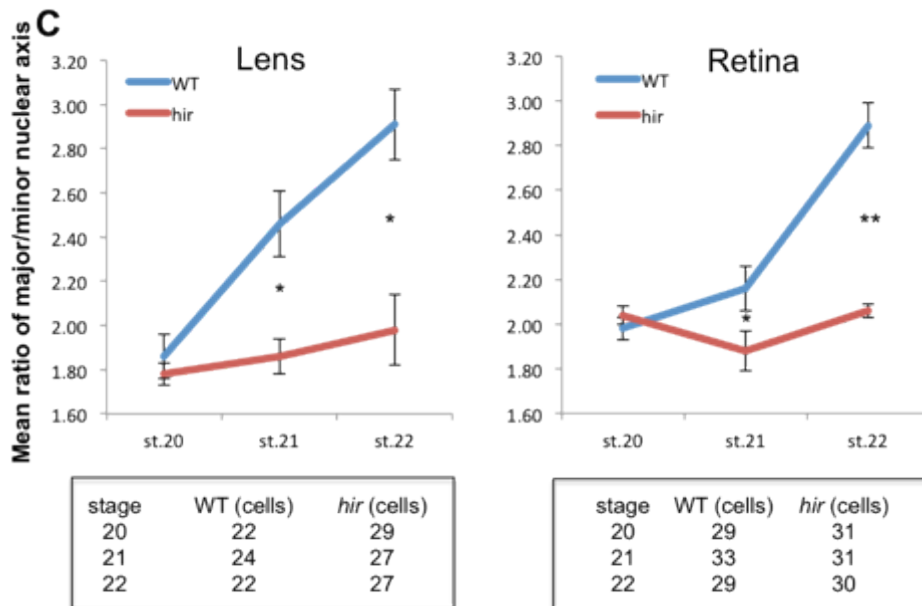


Figure 5.12 Tissue tension was reduced in *hirame* lens and retina. A, 3D rendering images of WT and *hir* embryos from confocal time-lapse series at st.22 (38 hpf). Embryos were labelled with MNFP. Blue and white nuclei are the 3D rendered nuclei. Scale bars=20 μ m. The compass shows the orientation of the embryo. A: anterior; P: posterior; M: medial; L: lateral. **B**, An illustration explaining how the major (longest) axis and minor (shortest) axis of a nucleus was measured. **C**, Quantification of the mean ratio of major to minor nucleus axis in the lens and the retina in both WT embryos and *hir* mutants from st.20 (31.5 hpf) to st.22 (38 hpf) (t-test, 3 WT and 3 *hir* embryos were analysed; * $P < 0.05$, ** $P < 0.01$). Panels A and B were generated in collaboration with Sean Porazinski.

5.2.7 Actomyosin activation is reduced in *hirame* mutants

The assembly of FN fibrils is dependent on the cell-generated tension, which is mediated by actomyosin contractility of the cytoskeleton (Heisenberg & Bellaïche, 2013). Higher actomyosin contractility enhances FN assembly while inhibition of myosin light chain kinase or RhoA GTPase decreases its assembly (Halliday and Tomasek, 1995; Zhang *et al.*, 1994, 1997; Zhong *et al.*, 1998). As actomyosin is a key regulator of cell-generated tension and is also involved in cell division (Scholey *et al.*, 2003), the activation status of actomyosin in the *hir* mutant was examined.

Contractility of actomyosin can be assessed by phosphorylation of myosin regulatory light chain (MRLC) at Serine 19 (Vicente-Manzanares *et al.*, 2009).

Therefore, phosphorylation Serine 19 of MRLC (pMRLC) was examined in WT embryos and *hir* mutants by immunoblotting. In WT embryo, pMRLC level increased from st.17 (25 hpf) to st.24 (44 hpf) (Fig.5.13). However the pMRLC level was lower in *hir* mutants throughout all stages (Fig.5.13).

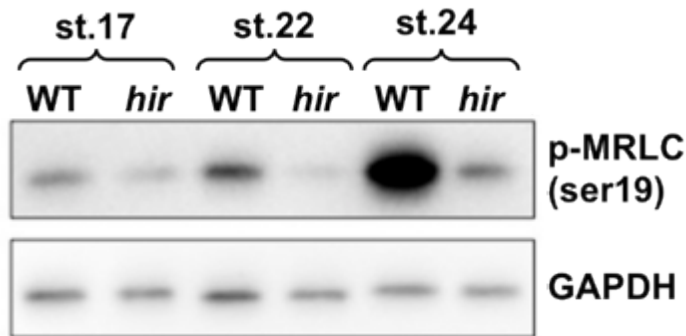


Figure 5.13. Phosphorylated MRLC levels are reduced in *hirame* mutants. Immunoblotting of phospho-myosin regulatory light chain (pMRLC) and control (GAPDH) at the indicated stages. pMRLC levels increased from st.17 (25 hpf) onwards in WT embryos, whereas in *hir* mutants the levels remained relatively low. Data was kindly provided by Dr. Shoji Hata.

5.2.8 Tissue tension of enveloping layer (EVL) is reduced in *hirame* mutants

The shape of EVL cells has been reported to correlate with their tissue tension (Köppen *et al.*, 2006). The EVL cells display a hexagonal to elongated morphology as epiboly proceeds, and the ratio of the longer to the shorter axis of a cell (length:width ratio, LWR, Fig.5.14A, 1) is an indicator of tissue tension (Köppen *et al.*, 2006). Therefore, LWR of individual EVL cell shape was quantified at around st16.5 (23 hpf) when EVL cells began to elongate in WT embryos, making differences in shape easier to detect in mutant embryos. Analysis was done in the following seven conditions. 1) WT embryos; 2) *hir* mutants; 3) maternal YAP knockdown *hir* mutants (*hir* embryos injected with the 0.3ng of YAP TBMO, termed mYAP KD *hir* thereafter) that exhibited more pronounced slow epiboly; 4) WT embryos injected with a translation-blocking (TB) morpholino against YAP (YAP TBMO, 0.6ng of 200 μ M); 5) MYH9a/10 knockdown WT embryos (myosin heavy chain 9a/10 TBMO injected into WT embryos, 0.6ng) as a control for myosin defective embryos; 6) WT embryos injected with MRLC AA mRNA (non-phosphorylatable MRLC, dominant-

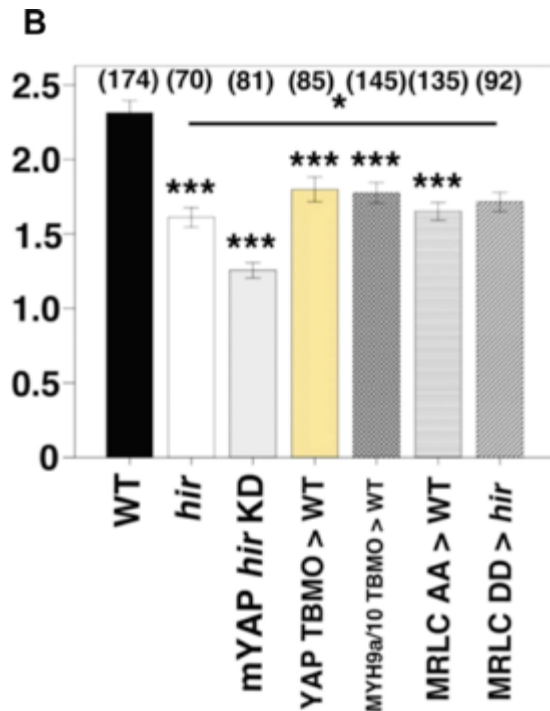


Figure 5.14. EVL tension is reduced in *hirame* mutant embryos. **A**, Cells of the EVL appear less elongated in *hir*, mYAP KD *hir* embryos and WT embryos injected with YAP TBMO. Furthermore, knockdown of components important for maintaining cellular tension (MYH9a/10 TBMO) or phosphomimicking the inactive state of MRLC (AA) in WT embryos also results in less elongated EVL cells. Injecting phosphoactive MRLC (DD) into *hir* mutants slightly rescues EVL cell elongation. 1) Schematic showing how EVL cell length (L) and width (W) was measured in marginal cells. EVL shape was visualised by phalloidin staining with fixed embryos at around 75% epiboly (\approx st.16.5, 23 hpf) and compared among, 2) WT, n=14; 3) *hir*, n=9; 4) mYAP KD *hir*, n=12, 5) WT embryos injected with a translation-blocking (TB) morpholino against YAP, n=9; 6) MYH9a/10 knockdown WT embryos, n=7; 7) MRLC-AA (dominant negative form) mRNA-injected WT, n=6; and 8) MRLC-DD (constitutive active form) mRNA-injected *hir* embryos, n=4. **B**, Quantification of EVL LWR for embryo types shown in A. Scale bar = 50 μ m. Total cell numbers measured are shown in parentheses above the graph. Error bars represent s.e.m. *** = p <0.001, one-way ANOVA. Panels B in collaboration with Sean Porazinski

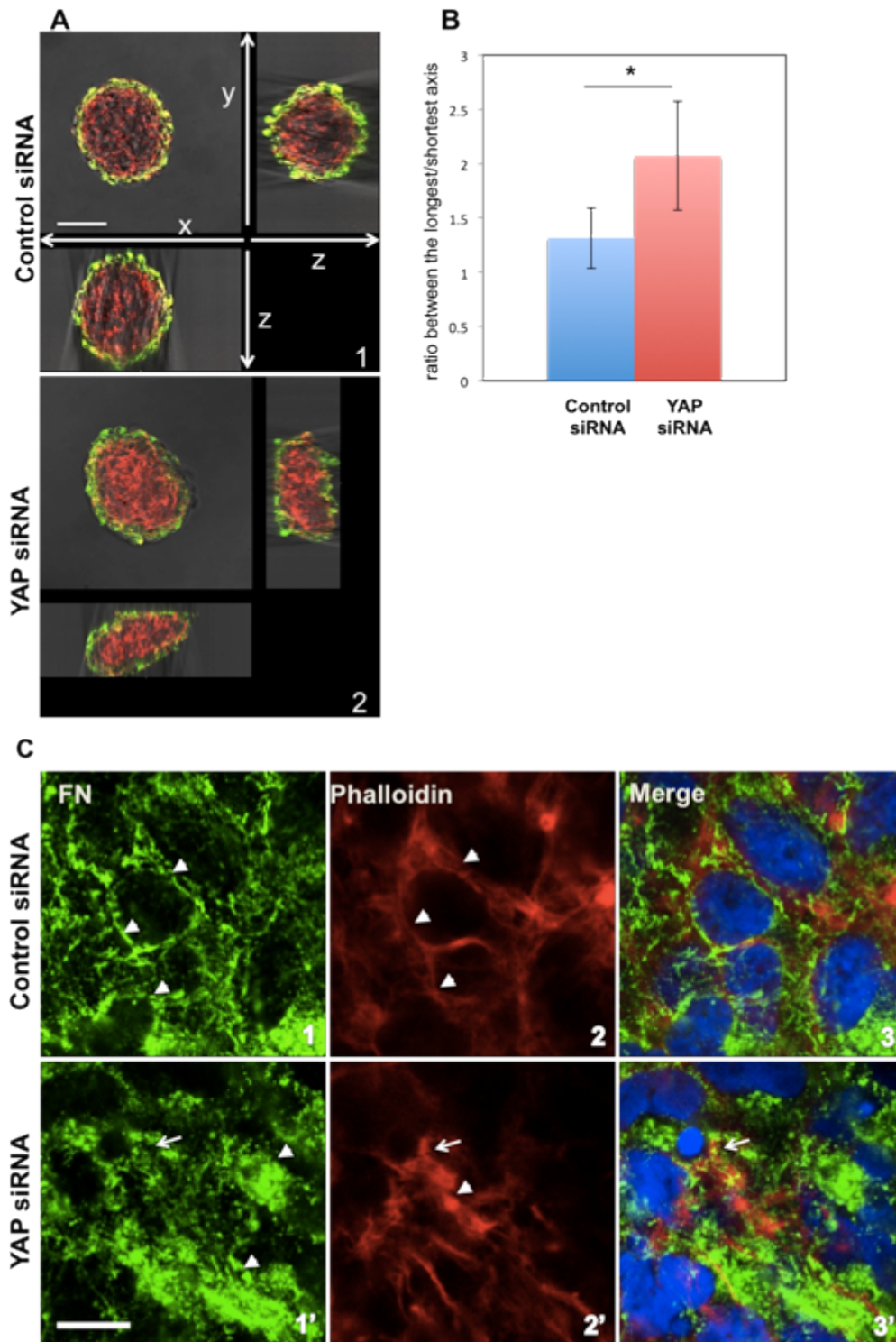
5.2.9 Over-polymerisation of F-actin leads to aberrant Fibronectin assembly

To gain mechanistic insights into YAP regulation of tissue tension and FN assembly and its potential conservation in humans, a human 3D spheroid *in vitro* culture system was necessary. Although 3D spheroids have been mainly

used to study cancer biology, they have served as an accessible *in vitro* system for testing human gene function in a controllable environment. The human telomerase-immortalised retinal pigmented epithelial cell line, hTERT-RPE1 (RPE1) was selected to generate 3D spheroids (3D spheroids were kindly generated and provided by Dr. Tatsuo Miyamoto. See Section 2.11 for details of preparation and processing of human spheroids), since siRNA YAP KD of these cells caused the least cell proliferation defects compared to another two mammalian epithelial cell lines tested (Madin Darby canine kidney (MDCK) and Michigan Cancer Foundation-7 (MCF7); personal communication with Dr. Tatsuo Miyamoto). The retinal pigment epithelium (RPE) is a polarised monolayer of pigmented cells that form the retinal-blood barrier (Bok, 1993). The RPE plays a crucial role in maintaining the homeostasis of the retina as it delivers nutrients from the choroid to the photoreceptor cells, while transporting ions, excess water and metabolic wastes in the opposite direction (Dornonville de la Cour M, 1993; Hamann, 2002). Besides, the RPE also has other essential functions such as light absorption, retinal proteins expression and secretion (Strauss, 2005).

Under slow centrifugation, unlike normal spheroids (Fig.5.15A 1), the YAP KD spheroids collapsed upon exposure to external forces (Fig.5.15A 2). Statistical analysis of the ratio of longest (L) /shortest (S) axes of control siRNA spheroids YAP KD spheroids showed a significant difference between the two samples (Fig.5.15B). These data suggested that YAP is also required for maintaining tissue tension for 3D tissue shape in human cells. YAP KD spheroids also lacked the fine beehive-liked FN fibrils and contained large FN deposits (Fig5.15C 1' arrowheads), as seen in the *hir* mutants. Cortical actomyosin contraction is required to stretch FN monomers for polymerisation to form FN fibrils. Consistently, FN fibril formation on the basal surface of control spheroids coincided with cortical F-actin bundles (arrowheads, Fig.5.15C 1-3). In contrast, loss of normal FN fibrils in YAP KD spheroids was associated with the reduced cortical F-actin bundles (Fig.5.15C 2'). Instead, F-actin aggregates were observed (Fig.5.15C 2' arrowhead), some of which were associated with large FN deposits (Fig.5.15C 1'-3' arrows), suggesting that a fraction of F-actin aggregates has increased local tension. Indeed, a

similar correlation of F-actin and FN fibril defects was observed in *hir* mutants (Fig.5.15D).



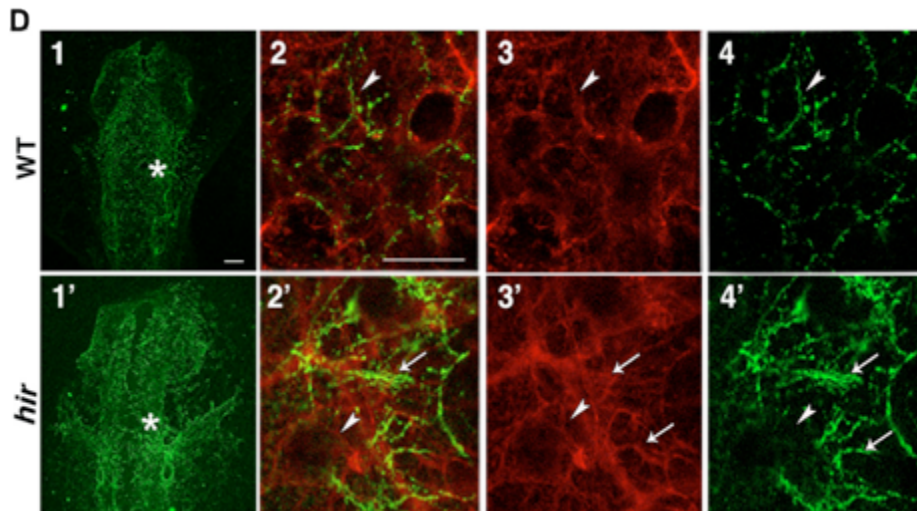


Figure 5.15 F-actin and FN localisations in 3D cultured YAP KD human cells and *hir* mutant embryos. **A**, Confocal 3D sectioning of longest and shortest axes of YAP/control (cont) KD spheroids after centrifugation. **B**, The ratio of longest (L)/shortest (S) axes of control siRNA spheroids (n=12) and YAP siRNA spheroids (n=7). Error bars represent \pm S.E.M. *P < 0.05, t-test. **C**, Whole-mount imaging of basal surfaces of RPE1 spheroids transfected with control siRNA (n=17) and YAP siRNA (n=13), stained for F-actin (red) and FN (green). (1, 1'), FN, (2, 2'), F-actin, (3, 3') merged. Arrowheads indicate cortical F-actin and FN fibrils localisation; arrows show ectopic F-actin aggregates and aberrant FN fibrils. **D**, Whole-mount imaging of WT (n=5) and *hir* mutants (n=4) stained for F-actin (red) and FN (green): (1, 1') whole view of embryos anterior up, only FN staining shown, (2-4, 2'-4') magnified view of the area indicated by asterisks in (1, 1'); merged (2, 2'), F-actin (3, 3') and FN (4, 4'). Arrowheads indicate cortical F-actin and FN fibrils in WT and corresponding region in *hir* (3, 4, 3', 4'); arrows show aberrant and ectopic F-actin and FN fibrils in (3', 4'). Scale bar (A) = 50 μ m; (C) = 10 μ m; (D) = 30 μ m.

5.3 Discussion

5.3.1 YAP is required for the formation of heart and Cuvierian ducts (CDs) via regulating Fibronectin (FN) assembly

Depletion of FN in mice, chicks and zebrafish leads to the *cardia bifida* where two separate hearts formed laterally to the body and the failure of blood vessel formation (George *et al.*, 1993; Linask and Lash, 1988a; Trinh & Stainier, 2004), suggesting FN is required for the formation of proper heart and blood vessels *in vivo*. Here in the medaka YAP mutant, such FN-related defects during the heart and blood vessel morphogenesis were also observed.

As described earlier in Chapter 3, *hir* mutants exhibit a unique flattened phenotype in addition to *cardiabifida* and truncated CDs. Analysis of FN localisation during heart formation in *hir* mutants showed that early FN deposition (st.20, 31 hpf) appears normal as expression of FN can be found laterally to the body where the cardiac precursors originate (Fig5.5). However, at st.22 (38 hpf) when the two populations of myocardial precursors migrate toward the midline to form the single heart, no FN deposition was detected at the midline but remained bilaterally in the *hir* embryo. At st.24 (44 hpf), while strong FN expression was observed in the heart ventricle in WT embryos beneath the midbrain-hindbrain boundary, the two populations of cardiac progenitors remained bilaterally in *hir* mutants (Fig.5.5).

FN deposition in the midline is required for the fusion of bilateral myocardial precursors in zebrafish and defects in adherens junctions between myocardial precursors is also identified in the zebrafish *nat (fn1)* mutant (Trinh & Stainier, 2004). Detailed analysis of cell polarity of cardiac precursors in *hir* mutants is necessary. While apical marker expression appears relatively normal (Fig.5.9), basal marker such as FN deposition is strongly affected in *hir* mutants. FN antibody staining in the *cmcl2:EGFP* transgenic embryos is required as it can provide more insight into how FN functions throughout the heart morphogenesis in both WT embryos and *hir* mutants.

Furthermore, downregulation of Mtx1, the zebrafish extra-embryonic yolk syncytial layer (YSL) specific transcription factor, can also cause *cardia bifid* (Sakaguchi *et al.*, 2006). Mtx1 in the extra-embryonic YSL appears to regulate the embryonic expression of fibronectin. Thus it would be interesting to assess whether the Mtx1 expression level in the *hir* mutant is altered.

Vasculogenesis is severely affected in mice FN null embryos (George *et al.*, 1993), while the formation of primitive red blood cells is normal. Similar results were observed in *hir* mutants during CD formation. The initiation and formation of blood cells appear normal in *hir* mutants, but the CDs are truncated. In WT embryos FN was expressed in both sides of the embryo body prior to the formation of the CDs and was faded once the CDs are formed. FN expression at the midline was also present throughout all stages examined in WT embryos. While *hir* mutant embryos had bilateral FN expressions at early stages (st.21-22, 34-38 hpf), the bilateral expression remained even at later stages (st.23-25, 41-50 hpf). Further FN1 antibody staining in the *fli::EGFP* transgenic embryos is necessary as some evidence has suggested that a fine FN matrix is necessary for the formation of CDs, as it serves a mechanical cue for the CDs cells to migrate correctly (Appendix Fig.8.1).

As mentioned in Chapter 3, some structures including dorsal aorta and gut (Fig 3.6 B, 3, 3') were found missing in *hir* mutants. In the less severe FN null mouse mutant (C57/BL6 background), formation of dorsal aortae is normal; however, the dorsal aortae and the heart appear collapsed (George EL *et al.*, 1997), which could be due to defective endothelial cell polarity. Thus, missing of dorsal aorta and gut could be due to collapsing of these structures in the mutant as FN assembly is affected. Or it could be due to missing of the gut primordia at early developmental stage. Expression pattern of molecular markers such as *gata-6*, *pdx* and *foxA2* (Wallace & Pack, 2003) for endodermal patterning and organ primordia within the developing digestive system needs to be investigated in the *hir* mutant. Cell apoptosis assay at early developmental stage before gut initiation starts can also be examined,

as it is possible that the missing gut is due to abnormal cell death of gut primordia.

Though whole-mount immunohistochemistry (IHC) analysis of FN protein localisation identified aberrant FN assembly in *hir* mutants, immunoblotting assay indicated that the total FN protein levels remained comparable to the WT embryo at earlier (st.17, 25 hpf) and later (st.23, 41 hpf) stages of development (Fig.5.6D). These data suggest that FN assembly rather than its production is affected in *hir* mutants. To conclude, YAP regulates proper FN fibrillisation, which provides a mechanical cue for the correct endothelial progenitor cell migration thus to initiate normal heart and CDs morphogenesis.

5.3.2 Deficient oriented cell division contributes to tissue flattening in *hir* mutants

Oriented cell division appears strongly affected in the *hir* mutant lens (Fig.5.10). Defective oriented cell division is also observed in the retina, neural tube and the ears (personal communication with Sean Porazinski). Oriented cell division is important for correct morphogenesis of tissues and has been well studied in the zebrafish neural tube (Tawk *et al.*, 2007).

Oriented cell division has been well studied in the retina, but less in the lens. In zebrafish retina, mitosis occurs parallel to the apical or basal surface (Das *et al.*, 2003), which may serve to add cells anteriorly and posteriorly to assist with the basal constriction of the retina. In WT embryos, a fairly equal frequency of parallel or perpendicular mitosis was seen (Fig.5.10), which helps the lens placode to grow proportionally and spherically. In the *hir* mutant, only parallel mitosis was observed suggesting the area of *hir* lens placode increases but not the thickness. It remains unclear if defective oriented cell division leads to the dislocation of lens placode and the formation of multiple lens placodes / lenses in the *hir* mutant.

5.3.3 FN fibril assembly is aberrant in *hir* mutants but blockage of FN assembly does not cause tissue flattening

FN antibody staining showed reduction of normal fibrils and increase of aberrant FN fibrils in *hir* mutants throughout development stages examined (st.15.5-23, 19-41 hpf). FN fibrillisation appears delayed and less organised during early developmental stages (st.15.5-17, 19-25 hpf) when epiboly proceeds. Inhibition of FN/integrin interactions and matrix assembly in *Xenopus* leads to arrest of epiboly (Marsden & DeSimone, 2001). This could explain the slow epiboly phenotype observed in the *hir* mutant.

At later stages (st.21-23, 34-41 hpf), the FN fibrils at the interspace between the olfactory placode and forebrain, lens and retina, somite boundaries as well as surrounding ears appeared coarse and rough compared to the smooth and fine fibrils seen in WT embryos (Fig.5.6A and B). Knockdown of FN also affects the initiation and maintenance of somite boundary maintenance and at later stage, the anterior somite formation and maintenance in zebrafish (Koshida *et al.*, 2005; Snow, *et al.*, 2008). This is consistent with the finding in Chapter 3 that anterior somites boundaries are less clear in *hir* mutant (Fig.3.4A and B) and probably the abnormal FN fibrils assembly contributes to this defect.

As abnormal FN fibrils assembly could be due to the blockage of FN assembly, in order to test if this was the cause of *hir* phenotype, mRNA encoding N-terminal 70kDa fragments of FN (FN 70kD), which act in a dominant negative manner to block FN assembly was injected into WT. Complete blockage of FN fibrils assembly leads to the tissue dislocation including lenses, ears (otic placodes) and *cardia bifida*, truncated Cuvierian ducts and distorted brain morphology but not tissue flattening (Fig.5.7). This suggests that tissue dislocation and cell migration defects could be due to aberrant FN assembly but that tissue flattening might be upstream of the FN assembly/fibrillogenesis defect.

5.3.4 YAP is required for FN-integrin interaction that further regulates the coordinated tissue/organ growth

FN fibrils assembly is initiated by FN-integrin interactions when FN binding to integrin receptors (Marsden & DeSimone, 2001), and integrin $\alpha_5\beta_1$ (*itg\alpha_5\beta_1*)

are the major receptors responsible for initial FN matrix assembly (Pankov *et al.*, 2000). As shown by immunohistochemistry and *in situ* hybridisation, enrichment of integrin- β 1 was reduced in *hir* mutants especially in the lens (Fig.5.11A and B). FN fibrills surrounding the lens also appears defective in *hir* mutant (Fig.5.8B). This FN assembly defect could be due to reduction of tissue tension (Mao and Schwarzbauer, 2005) and in turn affects FN-integrin signalling.

Activation of integrin-FN signalling is also required for the formation of polarised filopodia (Davidson *et al.*, 2006). During eye morphogenesis, filopodia normally mediate coordinated invagination of the lens and retina (Chauhan *et al.*, 2009). As abnormal filopodia protrusions were seen in *hir* between the lens and retina (Chapter 4), this suggests that failure of FN-integrin interaction may contribute to defective filopodia formation between the retina and lens in the mutant, resulting in lens dislocation and failure in the coordinated growth of the lens and retina to form a functional eye.

5.3.5 Actomyosin activity is reduced in *hirame* mutants and tissue tension is significantly reduced in the absence of YAP

The assembly of FN fibrils is dependent on the cell-generated tension, and actomyosin contractility contributes to FN fibril assembly (Halliday and Tomasek, 1995; Zhang *et al.*, 1994). Immunoblotting of pMRLC showed significantly reduced levels of actomyosin activity in *hir* mutants. This suggests that YAP may play a role in regulating cell tension via regulating actomyosin activity.

The shape of EVL cells has been reported to correlate with the tension of the overall tissue (Köppen *et al.*, 2006). As very loose and deformed periderm that originates from EVL was seen at st.23 (41 hpf; Fig.5.6C), suggesting reduction in tissue tension in *hir* mutants. EVL cell shape at early developmental stage (st.16.5, 23 hpf) was significantly less elongated in the *hir* mutant as the actomyosin reduced embryos via reduction of myosin heavy chain 9a/10 (MYH9a/10) and blockage of myosin regulatory chain activity (MRLC AA). Partial rescue of EVL tissue tension in *hir* mutants by activation

of actomyosin is consistent with our model that reduction of tissue tension in *hir* mutant is due to attenuated actomyosin activity.

Disruption of cortical F-actin bundles is the most probable cause of attenuated tissue tension since cortical F-actin contraction can be readily transmitted via cell-cell adhesion to generate tissue tension in epithelia. Both disruption of cortical F-actin bundles and the observed ectopic F-actin aggregates (Fig.5.15C) likely arise from F-actin over-polymerisation, detected in 3D cultured YAP KD cells (Fig.5.15C) and in *hir* mutants (Fig5.15D). F-actin over-polymerisation perturbs the F-actin turnover required for actomyosin contraction in the cytokinesis ring (Pinto *et al.*, 2012). Collectively, these data suggest YAP controls tissue tension via regulating actomyosin activity, thus to mediate proper FN fibril assembly.

Chapter 6: General discussion

6.1 The *hirame* phenotype and its underlying causes

The *hir* mutant survives until just before 6 days post fertilisation (6 dpf) when most of the organs have developed, allowing detailed analysis of the role of YAP for organogenesis, unlike YAP-null mice, which die around E8.5 (Morin-Kensicki *et al.*, 2006). The unique body flattening phenotype of *hir* mutants is associated with tissue flattening, tissue misalignment and cell migration defects. Organ and tissue flattening is seen most clearly in the brain, eye, neural tube (NT), and somites. Tissue misalignment is most evident in the lenses, olfactory vesicles and otic vesicles, which fails to invaginate into the retina, forebrain and hindbrain, respectively. Cell migration defects are mainly observed in epiboly during gastrulation and the formation of the Cuvierian ducts (CDs) and the heart during later developmental stages. This thesis has first characterised the *hir* phenotype followed by understanding the molecular mechanisms underlying the tissue flattening and misalignment. The major features of the *hir* phenotype and their possible causes are summarised in Table 6.1

Trait of <i>hirame</i> phenotype	Possible causes
Tissue and organ collapse:	
1. Brain	Missing brain ventricle formation, randomised cell division plane, reduced tissue tension and accelerated apoptosis.
2. NT	Reduced actomyosin activity, randomised cell division plane, abnormal FN assembly and reduced tissue tension.
3. Eyes	Reduced actomyosin activity, aberrant cell division plane and overall reduced tissue tension indicated by rounder nuclei.
4. Somites	Reduced actomyosin activity, aberrant cell division plane, cell slippage, overall reduced tissue tension and abnormal FN assembly.

<p>Tissue mislocation:</p> <p>1. Olfactory placode/pit</p> <p>2. Lens placode/vesicle</p> <p>3. Otic placode/vesicle</p>	<p>Abnormal FN assembly leading to disrupted filopodia formation and mislocation of adjacent tissues.</p> <p>Abnormal FN assembly leading to disrupted filopodia formation and mislocation of lenses and retinas.</p> <p>Abnormal FN assembly and defective lumen formation (multiple lumens or none).</p>
<p>Cell migration defects:</p> <p>1. Epiboly</p> <p>2. Cuvierian ducts</p> <p>3. Heart</p>	<p>Abnormal FN assembly</p> <p>Abnormal FN assembly, failing to provide mechanical cues for cells to migrate correctly.</p> <p>Abnormal FN assembly and defective cell migration.</p>

Table 6.1 Summary of the *hirame* phenotype and the potential underlying causes. The *hir* mutant exhibits three major phenotypes: tissue flattening, tissue mislocation and cell migration defects. Reduced tissue tension and tissue flattening is likely due to reduced actomyosin activity. Filopodia between tissues and cell-ECM adhesions do not form probably due to defective fibronectin-integrin signalling. Therefore tissues failed to undergo coordinated morphogenesis. Finally, cell migration defects are probably due to loss of polarity and aberrant migration cue caused by abnormal FN fibrillogenesis.

6.2 Is actomyosin-dependent tension the main cause of the *hirame* phenotype?

As mentioned in Table 6.1, several features of the *hir* phenotype including tissue flattening collapse, rounder nuclei, tissue dislocation, defects in cell migration and loss of oriented cell division, could potentially be caused by reduced tissue tension. Cell-generated tension, which is regulated by actomyosin contractility of the cytoskeleton, is essential for FN fibrils assembly (Heisenberg & Bellaïche, 2013). Indeed, the activation status of the myosin regulatory light chain (MRLC), which is the key for regulating non-muscle myosin II function, is dramatically reduced in the *hir* mutant. Disruption of cortical F-actin bundles (detected both *in vitro* and *in vivo*) is the most probable cause of attenuated tissue tension since cortical F-actin contraction can be readily transmitted via cell-cell adhesion to generate tissue tension in epithelia. Both disruption of cortical F-actin bundles and the observed ectopic F-actin aggregates likely arise from F-actin over-polymerisation, detected in 3D cultured YAP KD cells. F-actin over-polymerisation perturbs the F-actin turnover required for actomyosin contraction in the cytokinesis ring. Thus, most aspects of the *hir* phenotype appear to be the consequence of reduction in tension.

Overall tissue tension reduction is the most probable cause of the epithelial tissue and organ collapse observed in *hir* mutants. Once tissues/organs lose their proper mechanical rigidity, they will probably not be able to maintain their 3D shape. In line with this, the external force of gravity further affected collapse in *hir* mutants. Lack of contractility of actomyosin, a key regulator of cellular and tissue tension (Salbreux *et al.*, 2012), probably leads to misshaped organ/tissue in *hir* mutants, since rigidity is low. In addition, the normal morphogenesis essential for coordinated growth is also disrupted in *hir* mutants. Indeed actomyosin plays a crucial role in changing cell shape and sculpting tissue morphology (Wolpert and Tickle, 2010, p.291). Reduced actomyosin tension is also likely to cause the rounder nuclei in the cells and the less elongated cells in the enveloping layer of *hir* mutants. Furthermore, proper filopodia formation requires non-muscle myosin II phosphorylation (Ridley *et al.*, 2003), which is also reduced in *hir* mutants.

When blocking actin polymerisation in *Xenopus* by cytochalasin D, thicker and longer aberrant FN fibrils are observed (Davidson *et al.*, 2008), similar to those found in *hir* mutants. This suggests an actomyosin defect could result in the lack of FN fibrillation in the mutant since blocking actin polymerisation may also affect the function of the actomyosin network. Finally, the microenvironment of cells is essential for cell division, and the daughter cells are aligned with the external force field (Fink *et al.* 2011). It is possible that the cellular microenvironment is not providing sufficient mechanical cues due to defective FN fibrillation in *hir* mutants.

6.3 YAP regulation of tissue tension and FN assembly is probably mediated by ARHGAP18

ARHGAP18, which suppresses F-actin polymerisation by inhibiting RhoA activity, is one of the GTPase-activating proteins (GAPs) (Maeda *et al.*, 2011). Reduction of ARHGAP18 transcripts and protein levels were found in YAP KD spheroids (Porazinski *et al.*, 2015). Besides, ARHGAP18 KD spheroids exhibited reduced pMRLC levels and aberrant F-actin and FN assembly, which was similar to YAP KD spheroids (Porazinski *et al.*, 2015). Over-polymerisation of F-actin leads to both disruption of cortical F-actin bundles and formation of ectopic F-actin aggregates in YAP KD (Fig.5.15) and ARHGAP18 KD spheroids (Porazinski *et al.*, 2015). Thus, the disorganisation of F-actin is probably the cause of the flattening of the *hir* mutant rather than the consequence. These data suggest that ARHGAP18 is an effector of YAP in regulating cortical actomyosin network formation and controlling tissue tension (Porazinski *et al.*, 2015).

6.4 How YAP regulates the global 3D body shape of vertebrates?

Here we proposed a model explaining how YAP regulates 3D body shape formation *in vivo*, which extends from the molecular level to global body shape (Fig.6.1). YAP is essential for proper tissue tension by controlling expression of ARHGAP18, which mediates cortical actomyosin networks within individual cells. This tissue tension is required for cell stacking, which then generates correct 3D tissue architectures and proper assembly of ECM (FN assembly on

the basal surface of the tissue). Accurate 3D tissue architecture and ECM assembly contribute to the alignment of tissues (such as invagination of the lens into retina) to generate global 3D body shape (Fig.6.1 A).

The *hir* mutant provided a unique opportunity to investigate in live embryos how internal forces orchestrate cell and tissue dynamics to generate and align 3D tissues/organs within a living embryo. In the absence of YAP (Fig.6.1 B), transcripts and protein levels of ARHGAP18 were reduced, which attenuated actomyosin activity in *hir* mutants. Disrupted cortical F-actin bundles and ectopic F-actin aggregates were found at the surface of the tissue. Attenuation of actomyosin activity causes a reduction in tissue tension leading to slow epiboly and aberrant FN assembly as seen in *hir* during gastrulation and cell migration defects at later stages of development. Tension-mediated FN assembly could be the mechanism that integrates mechanical signals (e.g. tension generated by actomyosin) with biochemical signals (e.g. integrin signaling). This mechanism seems to be efficient since FN is the most upstream component in ECM assembly and initiates ECM organisation (Daley *et al.*, 2008). Notably, YAP-null mice show a phenotype similar to FN-null mice (Morin-Kensicki *et al.*, 2005). The collapse of the *hir* neural tube was associated with defective cell stacking due to compromised oriented cell divisions and cell alignments. Together, proper alignment of adjacent tissues (e.g. invagination of the lens into the retina) fails to occur in the mutant, which leads to the flattening of the embryo body.

Recent success in generating 3D eye cups from iPS/ES cells depends on self-organisation of tissue architecture and coordination of mechanical processes to shape the 3D eye cup (Sasai, 2013). The YAP controlled force-mediated morphogenesis could shed light on the intrinsic mechanism of tissue self-organisation. Thus, findings from this work could help to make more complex organs with coordinated alignment of multiple tissues and transplant them into patients.

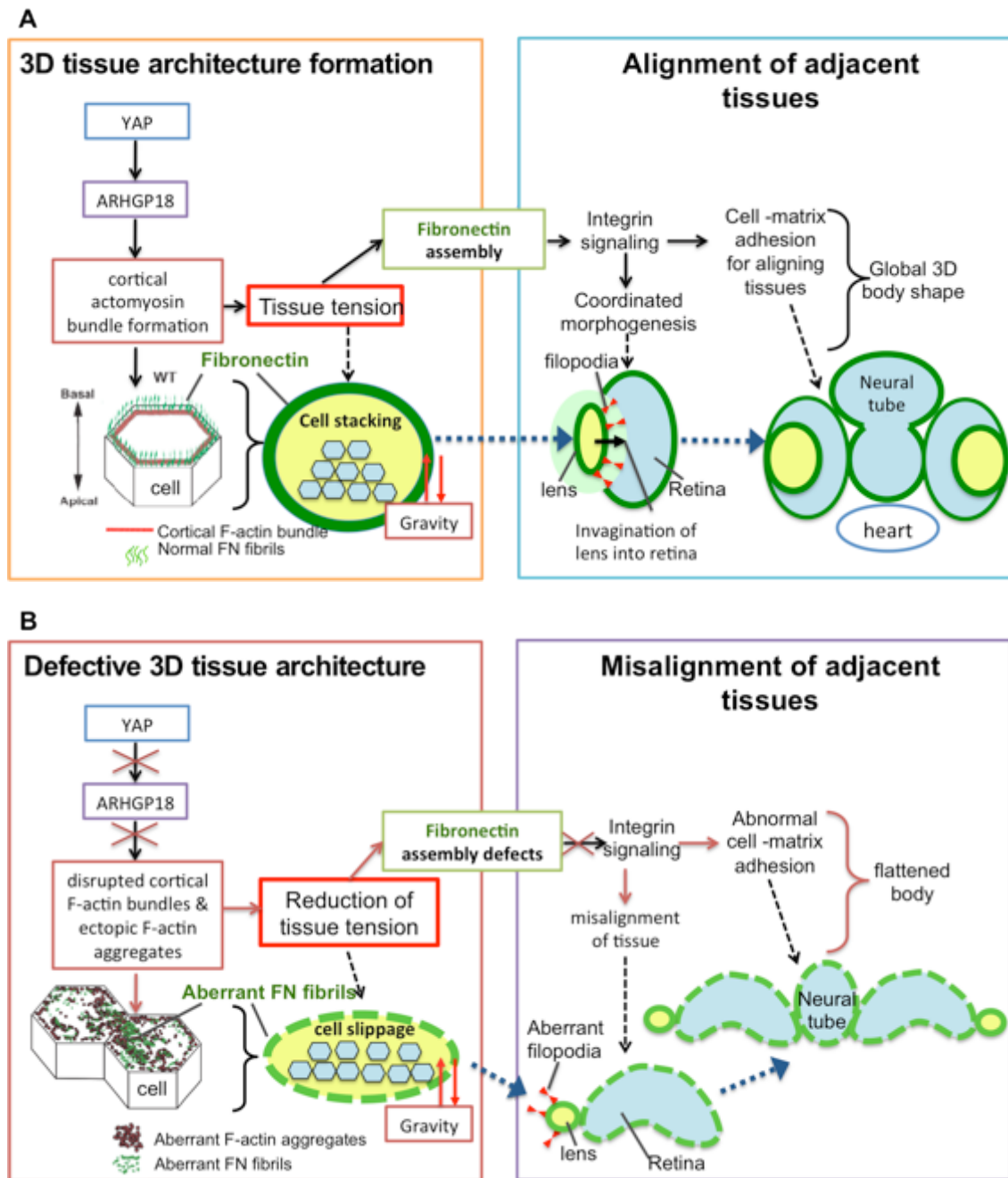


Figure 6.1. A model of YAP regulation of vertebrate 3D body shape. A, Illustration of how YAP regulates the formation of 3D tissues and their coordinated morphogenesis to build up the global vertebrate body shape. YAP mediates whole 3D tissue shape via the expression of ARHGAP18 (actin modulator). YAP regulation of actomyosin coordinates cell behaviours to build 3D tissues (e.g. the eye) with the correct tension. This triggers assembly of FN on the surface of these tissues, in turn activating integrin signalling. This leads to the formation of cell-matrix adhesions and the filopodia between tissues ensuring tissues are properly aligned. Consequently tissues can undergo coordinated morphogenesis leading to the global 3D body shape. Horizontal red arrows indicate increasing tissue tension. **B,** In the absence of

YAP, actin cytoskeleton modulator ARHGAP18 protein level is reduced, which then causes disrupted F-actin formation in *hir* mutants. Attenuation of F-actin activity causes a reduction in tissue tension leading to aberrant FN assembly. FN fibrils at the cell cortex are reduced and aberrant FN deposits coincide with ectopic F-actin aggregates in both *hir* mutants and YAP KD cells. Tension-mediated FN assembly could be the mechanism that integrates mechanical signals with biochemical signals (e.g. integrin signaling). The collapse of the *hir* neural tube was associated with defective cell stacking due to compromised oriented cell divisions and cell alignments. Proper tissues alignment doesn't happen in the mutant thus leads to the flattening of the body. Modified from Porazinski *et al.*, 2015.

6.5 Future work

Due to the time constraints, not all *hir* defects have been analysed comprehensively. Also, several interesting points have arisen based on the general characterisation of *hir* mutants. Further studies will be needed to 1) dissect the possible cause of multiple lumens formation in the mutant ear. Alteration of cell polarity could be one possibility, as formation of a lumen from cells requires apical-basal polarisation (Datta *et al.*, 2011). Analogous to the lens placode, it is likely that fragmenting otic placodes could result in multiple lumens. Thirdly, expression of genes (e.g. *vhnf1*) involved in lumen formation might be altered in *hir* mutants; 2) investigate likely defects result in missing structures including dorsal aorta and gut. There are several hypotheses. Firstly, formation of such structures did not occur at all. Expression pattern of molecular markers such as *gata-6*, *pdx* and *foxA2* (Wallace & Pack, 2003) for endodermal patterning and organ primordia within the developing digestive system needs to be investigated in the *hir* mutant. Secondly, cell apoptosis assay needs to be carried out to assess whether “disappearing” of these structures is due to excessive apoptosis; 3) examine if the retinal pigmented epithelium (RPE) is formed properly in the mutant, as the pigmentation of *hir* retina was strongly affected. This could be due to the pigmentation defects in RPE, or the complete loss of RPE. Morphological analysis at later stages (>st.28, 64 hpf) will be useful to identify which scenario is true. Expression of RPE specific markers can also be checked in the mutants; 4) examine whether the presence of multiple sensory placodes are due to formation of

multiple placodes or fragmenting placodes or mislocation of other type placode, thus early lineage trace might be necessary. Misexpression of *fgf3* and *fgf8* can lead to formation of ectopic otic vesicles and multiple otic vesicles respectively (Bajoghli *et al.*, 2004; Phillips *et al.*, 2004), but it is not known whether *fgf3* and *fgf8* are affected in *hir* mutants; 5) study *ARHGAP18* expression level *in vivo*. Further analysis of YAP-deficient human 3D spheroids revealed *ARHGAP18* is significantly reduced in the YAP KD spheroids. Besides, *ARHGAP18* KD spheroids exhibited reduced pMRLC levels and aberrant F-actin and FN assembly, which was similar to YAP KD spheroids (Porazinski *et al.*, 2015). However, these results were based on *in vivo* experiments. *ARHGAP18* transcripts and protein levels need to be checked in the medaka embryos. *ARHGAP18* mRNA injection into *hir* mutants also needs to be performed to check if the *hir* phenotype can be rescued. These are the areas of the mutant phenotype that require further work.

Chapter 7: References

- Akimenko, M. A., Ekker, M., Wegner, J., Lin, W., & Westerfield, M. (1994). Combinatorial expression of three zebrafish genes related to *distal-less*: part of a homeobox gene code for the head. *The Journal of Neuroscience: The Official Journal of the Society for Neuroscience*, 14(6), pp. 3475–3486.
- Aoki, Y., Saint-Germain, N., Gyda, M., Magner-Fink, E., Lee, Y.-H., Credidio, C., & Saint-Jeannet, J.-P. (2003). Sox10 regulates the development of neural crest-derived melanocytes in *Xenopus*. *Developmental Biology*, 259(1), pp. 19–33.
- Aragona, M., Panciera, T., Manfrin, A., Giullitti, S., Michielin, F., Elvassore, N., Dupont, S., Piccolo, S. (2013). A Mechanical Checkpoint Controls Multicellular Growth through YAP/TAZ Regulation by Actin-Processing Factors. *Cell*, 154(5), pp. 1047–1059.
- Asaoka, Y., Hata, S., Namae, M., Furutani-Seiki, M., & Nishina, H. (2014). The Hippo pathway controls a switch between retinal progenitor cell proliferation and photoreceptor cell differentiation in zebrafish. *PLoS One*, 9(5), e97365.
- Babb, S. G., Barnett, J., Doedens, A L., Cobb, N., Liu, Q., Sorkin, B. C., Yelick, P.C., Raymond, P.A., & Marris, J. A. (2001). Zebrafish E-cadherin: expression during early embryogenesis and regulation during brain development. *Developmental Dynamics: An Official Publication of the American Association of Anatomists*, 221(2), pp. 231–237.
- Baker, C. V., & Bronner-Fraser, M. (2001). Vertebrate cranial placodes I. Embryonic induction. *Developmental Biology*, 232(1), pp. 1–61.
- Bailey, A. P., Bhattacharyya, S., Bronner-Fraser, M., & Streit, A. (2006). Lens specification is the ground state of all sensory placodes, from which FGF promotes olfactory identity. *Developmental cell*, 11, pp. 505–517.
- Bao, Y., Hata, Y., Ikeda, M., & Withanage, K. (2011). Mammalian Hippo pathway: from development to cancer and beyond. *The Journal of Biochemistry*, 149, pp. 361–379.
- Baumgartner, R., Poernbacher, I., Buser N., Hafen, E., & Stocker, H. (2010). The WW domain protein Kibra acts upstream of Hippo in *Drosophila*. *Developmental cell*, 18, pp. 309–316.
- Bilder, D., Schober, M., Perrimon, N., (2003). Integrated activity of PDZ protein complexes regulates epithelial polarity. *Nature Cell Biology*. 5, pp. 53–58.

- Britsch, S., Goerich, D.E., Riethmacher, D., Peirano, R.I., Rossner, M., Nave, K.A., Birchmeier, C., & Wegner, M. (2001). The transcription factor Sox10 is a key regulator of peripheral glial development. *Genes & Development* 15, pp. 66–78.
- Bok D. (1993) The retinal pigment epithelium: a versatile partner in vision. *Journal of cell science. Supplement* 17, pp. 189–195.
- Camargo, F.D., Gokhale, S., Johnnidis, J.B., Fu, D., Bell, G.W., Jaenisch, R., & Brummelkamp, T.R. (2007). YAP1 increases organ size and expands undifferentiated progenitor cells. *Current Biology*, 17(23), pp. 2054–2060.
- Cao, X., Pfaff, S.L., & Gage, F.H. (2008). YAP regulates neural progenitor cell number via the TEA domain transcription factor. *Genes & Development*, 22(23), pp. 3320–3334.
- Chauhan, B.K., Disanza, A., Choi, S., Faber, S.C., Lou, M., Beggs, H.E., Scita, G., Zheng, Y & Lang, R.A. (2009). Cdc42- and IRSp53-dependent contractile filopodia tether presumptive lens and retina to coordinate epithelial invagination. *Development* 136, pp. 3657–3667.
- Chen, C.-L., Gajewski, K. M., Hamaratoglu, F., Bossuyt, W., Sansores-Garcia, L., Tao, C., & Halder, G. (2010). The apical-basal cell polarity determinant Crumbs regulates Hippo signaling in Drosophila. *Proceedings of the National Academy of Sciences of the United States of America*, 107(36), pp.15810–15815.
- Cherrett, C., Furutani-Seiki, M., & Bagby, S. (2012). The Hippo pathway: key interaction and catalytic domains in organ growth control, stem cell self-renewal and tissue regeneration. *Essays in Biochemistry*, 53(1), pp. 111–127.
- Chow, R. L., & Lang, R. A. (2001). Early eye Development in Vertebrates. *Annual Review of Cell and Developmental Biology*, (17), pp. 255–296.
- Collignon, J., Sockanathan, S., Hacker, a, Cohen-Tannoudji, M., Norris, D., Rastan, S., ... Lovell-Badge, R. (1996). A comparison of the properties of Sox-3 with Sry and two related genes, Sox-1 and Sox-2. *Development (Cambridge, England)*, 122(2), pp. 509–520.
- Cvekl, A., & Piatigorsky, J. (1996). Lens development and crystallin gene expression: many roles for Pax-6. *Bioessays* 18, pp. 621–630.
- Daley, W.P., Peters, S.B. & Larsen, M. (2008). Extracellular matrix dynamics in development and regenerative medicine. *Journal of Cell Science*, 121(3), pp. 255–264.
- Das, T., Payer, B., Cayouette, M., Harris, W.A. (2003). In vivo time-lapse imaging of cell divisions during neurogenesis in the developing zebrafish retina. *Neuron*, 37(4), pp. 597–609.

- Datta, A., Bryant, D. M., & Mostov, K. E. (2011). Molecular regulation of lumen morphogenesis. *Current Biology : CB*, 21(3), R126–136.
- Davidson, L.A., Marsden, M., Keller, R., Desimone, D.W. (2006) Integrin alpha5beta1 and fibronectin regulate polarized cell protrusions required for *Xenopus* convergence and extension. *Current Biology*, 16, pp. 833–844.
- Dong, J., Feldmann, G., Huang, J., Wu, W., Zhang, N., Comerford, S.A., Gayyed, M.F., Anders, R.A., Maitra, A., & Pan, D., (2007). Elucidation of a Universal Size-Control Mechanism in *Drosophila* and Mammals. *Cell*, 130, pp. 1120-1133.
- Dornonville de la Cour M. (1993). Ion transport in the retinal pigment epithelium. A study with double barrelled ion-selective microelectrodes. *Acta ophthalmologica Scandinavica. Supplement.* 209, pp. 1–32.
- Dzamba, B. J., Jakab, K. R., Marsden, M., Schwartz, M. A., & DeSimone, D. W., (2009). Cadherin Adhesion, Tissue Tension, and Noncanonical Wnt Signaling Regulate Fibronectin Matrix Organization. *Developmental Cell*, 16(3), pp. 421–432.
- Etienne-Manneville, S. (2004). Cdc42--the centre of polarity. *Journal of Cell Science*, 117(Pt 8), pp. 1291–1300.
- Fink, J., Carpi, N., Betz, T., Bétard, A., Chebah, M., Azioune, A., Bornens, M., Sykes, C., Fetler, L., Cuvelier, D., Piel, M. (2011). External forces control mitotic spindle positioning. *Nature Cell Biology*, 13(7), pp. 771–778
- Fujita, M., Isogai, S., Kudo, A. (2006). Vascular anatomy of the developing medaka, *Oryzias latipes*: A complementary fish model for cardiovascular research on vertebrates. *Developmental Dynamics*, 235(3), pp. 734–746.
- Furutani-Seiki, M., Sasado, T., Morinaga, C., Suwa, H., Niwa, K., Yoda, H., Deguchi, T., Hirose, Y., Yasuoka, A., Henrich, T., Watanabe, T., Iwanami, N., Kitagawa, D., Saito, K., Asaka, S., Osakada, M., Kunimatsu, S., Momoi, A., Elmasri, H., Winkler, C., Ramialison, M., Loosli, F., Quiring, R., Carl, M., Grabher, C., Winkler, S., Del Bene, F., Shinomiya, A., Kota, Y., Yamanaka, T., Okamoto, Y., Takahashi, K., Todo, T., Abe, K., Takahama, Y., Tanaka, M., Mitani, H., Katada, T., Nishina, H., Nakajima, N., Wittbrodt, J., & Kondoh, H., (2004). A systematic genome-wide screen for mutations affecting organogenesis in Medaka, *Oryzias latipes*, *Mechanisms of Development*, 121(7), pp. 647-658.
- Gao, N., & Kaestner, K. H. (2010). Cdx2 regulates endo-lysosomal function and epithelial cell polarity. *Genes & Development*, 24(12), pp. 1295–305. doi:10.1101/gad.1921510
- Gee, S. T., Milgram, S. L., Kramer, K. L., Conlon, F. L., & Moody, S. A. (2011). Yes-associated protein 65 (YAP) expands neural progenitors and

- regulates Pax3 expression in the neural plate border zone. *PLoS One*, 6(6), e20309.
- George, E. L., Georges-Labouesse, E. N., Patel-King, R. S., Rayburn, H., & Hynes, R. O. (1993). Defects in mesoderm, neural tube and vascular development in mouse embryos lacking fibronectin. *Development (Cambridge, England)*, 119(4), pp. 1079–1091.
- George, E. L., Baldwin, H. S., & Hynes, R. O. (1997) Fibronectins are essential for heart and blood vessel morphogenesis but are dispensable for initial specification of precursor cells. *Blood*, 90, pp. 3073–3081.
- Georges-Labouesse, E.N., George, E.L., Rayburn, H., Hynes, R.O. (1996). Mesodermal development in mouse embryos mutant for fibronectin. *Developmental Dynamics*, 207, pp. 145–156.
- Giancotti, F.G., and E. Ruoslahti. (1990). Elevated levels of the $\alpha 5\beta 1$ fibronectin receptor suppress the transformed phenotype of Chinese hamster ovary cells. *Cell*. 60, pp. 849–859.
- Glasgow, E., & Tomarev, S. I. (1998). Restricted expression of the homeobox gene *prox 1* in developing zebrafish. *Mechanisms of Development*, 76(1-2), pp. 175–178.
- Graziadei, P. P., & Monti-Graziadei, A. G. (1992). The influence of the olfactory placode on the development of the telencephalon in *Xenopus laevis*. *Neuroscience*, 46, pp. 617–629.
- Greiling, T. M. S., & Clark, J. I. (2009). Early lens development in the zebrafish: a three-dimensional time-lapse analysis. *Developmental Dynamics: An Official Publication of the American Association of Anatomists*, 238(9), pp. 2254–2265.
- Groves AK (2005) The Induction of the Otic Placode. In: Popper AN, Kelley MW, Wu DK, editors. *Development of the Inner Ear*. New York: Springer Verlag. pp. 10–42.
- Grzeschik, N.A., Parsons, L.M., Allott, M.L., Harvey, K.R., & Richardson, H.E. (2010). *Lgl/aPKC* and *Crb* regulate the Salvador/Warts/Hippo pathway. *Fly*, 4(4), pp. 288–293.
- Gustafsson, E., & Fassler, R. (2000). Insights into extracellular matrix functions from mutant mouse models. *Experimental Cell Research*, 261, pp. 52-68.
- Haffter, P., Granato, M., Brand, M., Mullins, M.C., Hammerschmidt, M., Kane, D.A., Odenthal, J., van Eeden, F.J., Jiang, Y.J., Heisenberg, C.P., Kelsh, R.N., Furutani-Seiki, M., Vogelsang, E., Beuchle, D., Schach, U., Fabian, C., Nüsslein-Volhard, C. (1996). The identification of genes with unique

- and essential functions in the development of the zebrafish, *Danio rerio*. *Development*, 123, pp. 1–36.
- Halliday, N.L., & Tomasek, J.J. (1995). Mechanical properties of the extracellular matrix influence fibronectin assembly in vitro. *Experimental Cell Research*, 217, pp. 109–117.
- Hamann S. (2002). Molecular mechanisms of water transport in the eye. *International Review of Cytology*. 215, pp. 395–431.
- Hamaratoglu, F., Willecke, M., Kango-Singh, M., Nolo, R., Hyun, E., Tao, C., Jafar-Nejad, H., & Halder, G. (2006). The tumour-suppressor genes NF2/Merlin and Expanded act through Hippo signalling to regulate cell proliferation and apoptosis. *Nature Cell Biology*, 8, pp. 27–36.
- Heallen, T., Zhang, M., Wang, J., Bonilla-Claudio, M., Klysiak, E., Johnson, R.L., Martin, J.F. (2011). Hippo pathway inhibits Wnt signaling to restrain cardiomyocyte proliferation and heart size. *Science*, 332, pp. 458–461.
- Heisenberg, C.-P., & Bellaïche, Y. (2013). Forces in Tissue Morphogenesis and Patterning. *Cell*, 153(5), pp. 948–962.
- Hill, V.K., Dunwell, T.L., Catchpoole, D., Krex, D., Brini, A.T., Griffiths, M., Craddock, C., Maher, E.R., & Latif, F. (2011). Frequent epigenetic inactivation of KIBRA, an upstream member of the Salvador/Warts/Hippo (SWH) tumor suppressor network, is associated with specific genetic event in B-cell acute lymphocytic leukemia. *Epigenetics*, 6(3), pp.326–332.
- Hochmann, S., Aghaallaei, N., Bajoghli, B., Soroldoni, D., Carl, M., & Czerny, T. (2007). Expression of marker genes during early ear development in medaka. *Gene Expression Patterns : GEP*, 7(3), pp. 355–362.
- Hong, J.-H., Yaffe, M.B. (2006). TAZ: a beta-catenin-like molecule that regulates mesenchymal stem cell differentiation. *Cell Cycle*, 5(2), pp.176–179.
- Hu, J., Sun, S., Jiang, Q., Sun, S., Wang, W., Gui, Y., & Song, H. (2013). Yes-associated protein (yap) is required for early embryonic development in zebrafish (*danio rerio*). *International Journal of Biological Sciences*, 9(3), pp. 267–278.
- Huang, C. J., Tu, C. T., Hsiao, C. D., Hsieh, F. J. & Tsai, H. J. (2003). Germ-line transmission of a myocardium-specific GFP transgene reveals critical regulatory elements in the cardiac myosin light chain 2 promoter of zebrafish. *Developmental Dynamics*, 228(1), pp. 30–40.
- Huang, J., Wu, S., Barrera, J., Matthews, K., Pan, D. (2005). The Hippo signaling pathway coordinately regulates cell proliferation and apoptosis

- by inactivating Yorkie, the Drosophila Homolog of YAP. *Cell*, 122(3), pp. 421–434.
- Hynes, R.O. Fibronectins. New York, NY: Springer-Verlag Inc; 1990.
- Iwamatsu, T. (2004). Stages of normal development in the medaka *Oryzias latipes*. *Mechanisms of Development*, 121, pp. 605–618.
- Jiang, Q., Liu, D., Gong, Y., Wang, Y., Sun, S., Gui, Y., & Song, H. (2009). Yap Is Required for the Development of Brain, Eyes, and Neural Crest in Zebrafish. *Biochemical and Biophysical Research Communications*, 384(1), pp. 114–119.
- Julich, D., Geisler, R., Holley, S.,A. (2005). Integrin α 5 and delta/notch signaling have complementary spatiotemporal requirements during zebrafish somitogenesis. *Developmental Cell*, 8, pp. 575–586.
- Jülich, D., Mould, A.P., Koper, E., Holley, S.A. (2009). Control of extracellular matrix assembly along tissue boundaries via Integrin and Eph/Ephrin signaling. *Development*, 136, pp. 2913–2921.
- Kango-Singh, M., & Singh, A. (2009). Regulation of organ size: insights from the Drosophila Hippo signaling pathway. *Developmental Dynamics*, 238, 1627–1637.
- Kasahara, M., Naruse, K., Sasaki, S., Nakatani, Y., Qu, W., Ahsan, B., Yamada, T., Nagayasu, Y., Doi, K., Kasai, Y., Jindo, T., Kobayashi, D., Shimada, A., Toyoda, A., Kuroki, Y., Fujiyama, A., Sasaki, T., Shimizu, A., Asakawa, S., Shimizu, N., Hashimoto, S., Yang, J., Lee, Y., Matsushima, K., Sugano, S., Sakaizumi, M., Narita, T., Ohishi, K., Haga, S., Ohta, F., Nomoto, H., Nogata, K., Morishita, T., Endo, T., Shin, I.T., Takeda, H., Morishita, S., & Kohara, Y. (2007). The medaka draft genome and insights into vertebrate genome evolution. *Nature*, 447, pp. 714-719.
- Katogi, R., Nakatani, Y., Shin-I, T., Kohara, Y., Inohaya, K., and Kudo, A. (2004). Large-scale analysis of the genes involved in fin regeneration and blastema formation in the medaka, *Oryzias latipes*. *Mechanisms of Development*, 121, pp. 861-872.
- Kim, N. G., Koh, E., Chen, X. and Gumbiner, B. M. (2011). E-cadherin mediates contact inhibition of proliferation through Hippo signaling-pathway components. *Proceedings of the National Academy of Sciences*, 108, pp. 11930-11935.
- Kitagawa, D., Watanabe, T., Saito, K., Asaka, S., Sasado, T., Morinaga, C., Suwa, H., Niwa, K., Yasuoka, A., Deguchi, T., Yoda, H., Hirose, Y., Henrich, T., Iwanami, N., Kunimatsu, S., Osakada, M., Winkler, C., Elmasri, H., Wittbrodt, J., Loosli, F., Quiring, R., Carl, M., Grabher, C., Winkler, S., & Furutani-Seiki, M. (2004). Genetic dissection of the

- formation of the forebrain in Medaka, *Oryzias latipes*. *Mechanisms of Development*, 121(7-8), pp. 673–685.
- Kleinman, H. K., Philp, D., & Hoffman, M. P. (2003). Role of the extracellular matrix in morphogenesis. *Current Opinion in Biotechnology*, 14(5), pp. 526–532.
- Kobayashi, M., Osanai, H., Kawakami, K., and Yamamoto, M. (2000). Expression of three zebrafish Six4 genes in the cranial sensory placodes and the developing somites. *Mechanisms of Development*, 98, pp. 151–155.
- Koh, W., Mahan, R. D., & Davis, G. E. (2008). Cdc42- and Rac1-mediated endothelial lumen formation requires Pak2, Pak4 and Par3, and PKC-dependent signaling. *Journal of Cell Science*, 121(7), pp. 989–1001.
- Kondoh, H. (1999). Transcription factors for lens development assessed in vivo. *Current Opinion in Genetics & Development*, 9, pp. 301–308.
- Köppen, M., Fernández, B.G., Carvalho, L., Jacinto, A., Heisenberg, C.-P. 2006. Coordinated cell-shape changes control epithelial movement in zebrafish and *Drosophila*. *Development*, 133(14), pp. 2671–2681.
- Koshida, S., Kishimoto, Y., Ustumi, H., Shimizu, T., Furutani-Seiki, M., Kondoh, H., & Takada, S. (2005). Integrin α 5-dependent fibronectin accumulation for maintenance of somite boundaries in zebrafish embryos. *Developmental Cell*, 8(4), pp. 587–598.
- Köster, R.W., Kühnlein, R.P., Wittbrodt, J., (2000). Ectopic Sox3 activity elicits sensory placode formation. *Mechanisms of Development*, 95, pp.175-187.
- Kretzschmar, K. & Watt, F.M., (2012). Lineage tracing. *Cell*, 148(1-2), pp.33–45.
- Ladher, R.K., Anakwe, K.U., Gurney, A.L., Schoenwolf, G.C., Francis-West, P.H. (2000). Identification of synergistic signals initiating inner ear development. *Science* 290, pp. 1965– 1967.
- Lang, R.A. (2004). Pathways regulating lens induction in the mouse. *The International Journal of Developmental Biology*, 48, pp. 783–791.
- Lawson, N.D. & Weinstein, B.M., 2002. In vivo imaging of embryonic vascular development using transgenic zebrafish. *Developmental biology*, 248(2), pp. 307–318.
- Lecaudey, V., Ulloa, E., Anselme, I., Stedman, A., Schneider-Maunoury, S., Pujades, C. (2007). Role of the hindbrain in patterning the otic vesicle: a study of the zebrafish *vhnf1* mutant. *Developmental Biology*, 303(1), pp. 134-143.

- Linask, K.K., Lash, J.W. (1988a) A role for fibronectin in the migration of avian precardiac cells. I. Dose-dependent effects of fibronectin antibody. *Developmental Biology*, 129, pp. 315–323.
- Linask, K.K., Lash, J.W. (1988b) A role for fibronectin in the migration of avian precardiac cells. II. Rotation of the heart-forming region during different stages and its effects. *Developmental Biology*, 129, pp. 324–329.
- Loh, S.-L., Teh, C., Muller, J., Guccione, E., Hong, W., & Korzh, V. (2014). Zebrafish yap1 plays a role in differentiation of hair cells in posterior lateral line. *Scientific Reports*, 4(4289).
- Loosli, F, S Winkler, C Burgtorf, E Wurmbach, W Ansorge, T Henrich, C Grabher, Arendt, D., Carl, M., Krone, A., Grzebisz, E., & Wittbrodt, J. (2001). Medaka Eyeless Is the Key Factor Linking Retinal Determination and Eye Growth. *Development*, 128 (20), pp. 4035–4044.
- Lowery, L. A., De Rienzo, G., Gutzman, J. H., & Sive, H. (2009). Characterization and classification of Zebrafish brain Morphology Mutants. *Anatomical Record (Hoboken)*, 292(1), pp. 94–106.
- Lu, L., Li, Y., Kim, S.M., Bossuyt, W., Liu, P., Qiu, Q., Wang, Y., Halder, G., Finegold, M.J., Lee, J.S., & Johnson, R.L. (2010). Hippo signaling is a potent in vivo growth and tumor suppressor pathway in the mammalian liver. *Proceedings of the National Academy of Sciences*, 107, pp. 1437–1442
- Macara, I. G., Guyer, R., Richardson, G., Huo, Y. & Ahmed, S. M. (2014). Epithelial Homeostasis. *Current Biology*, 24, R815–R825.
- Magnusson, M. K., & Mosher, D. F. (1998). Fibronectin : Structure, Assembly, and Cardiovascular Implications. *Arteriosclerosis, Thrombosis, and Vascular Biology*, 18(9), pp. 1363–1370.
- Mammoto, T., & Ingber, D. E. (2010). Mechanical control of tissue and organ development. *Development (Cambridge, England)*, 137(9), pp. 1407–1420.
- Mao, Y., & Schwarzbauer, J. E. (2005). Fibronectin fibrillogenesis, a cell-mediated matrix assembly process. *Matrix Biology: Journal of the International Society for Matrix Biology*, 24(6), pp. 389–399.
- Marcelo, K. L., Goldie, L. C., & Hirschi, K. K. (2013). Regulation of endothelial cell differentiation and specification. *Circulation Research*, 112(9), pp. 1272–1287.
- Maroon, H., Walshe, J., Mahmood, R., Kiefer, P., Dickson, C., Mason, I. (2002). Fgf3 and Fgf8 are required together for formation of the otic placode and vesicle. *Development* 129, pp. 2099–2108.

- Marsden, M., & DeSimone, D. W. (2001). Regulation of cell polarity, radial intercalation and epiboly in *Xenopus*: novel roles for integrin and fibronectin. *Development (Cambridge, England)*, 128(18), pp. 3635–3647.
- Matsui, T., Raya, A., Callol-Massot, C., Kawakami, Y., Oishi, I., Rodriguez-Esteban, C., Belmonte, J.C. (2007) miles-apart-Mediated regulation of cell-fibronectin interaction and myocardial migration in zebrafish. *Nature clinical practice Cardiovascular medicine*, 4, S77–S82.
- Mattila, P. K., & Lappalainen, P. (2008). Filopodia: molecular architecture and cellular functions. *Nature Reviews Molecular Cell Biology*, 9(6), pp. 446–454.
- Maeda, M., Hasegawa, H., Hyodo, T., Ito, S., Asano, E., Yuang, H., Funasaka, K., Shimokata, K., hasegawa, Y., Hamaguchi, M., & Senga, T. (2011). ARHGAP18, a GTPase-activating protein for RhoA, controls cell shape, spreading, and motility. *Molecular biology of the cell*, 22(20), pp. 3840–3852.
- Miyasaka, N., Knaut, H., and Yoshihara, Y. (2007). Cxcl12/Cxcr4 chemokine signaling is required for placode assembly and sensory neurons pathfinding in the zebrafish olfactory system. *Development* 134, pp. 2459–2468.
- Mochizuki, E., Fukuta, K., Tada, T., Harada, T., Watanabe, N., Matsuo, S., Hashimoto, H., Ozato, K., Wakamatsu, Y. (2005). Fish mesonephric model of polycystic kidney disease in medaka (*Oryzias latipes*) pc mutant. *Kidney International*, 68(1), pp. 23-34.
- Morin-kensicki, E. M., Boone, B. N., Howell, M., Stonebraker, J. R., Teed, J., Alb, J. G., Magnuson, T. R., O'Neal, W., & Milgram, S.L. (2006). Defects in Yolk Sac Vasculogenesis , Chorioallantoic Fusion , and Embryonic Axis Elongation in Mice with Targeted Disruption of Yap65 Defects in Yolk Sac Vasculogenesis , Chorioallantoic Fusion , and Embryonic Axis Elongation in Mice with Targeted Disrupt. *Molecular and Cellular Biology*, 26(1), pp. 77–87.
- Nelson, C. M. & Bissell, M. J. (2006). Of extracellular matrix, scaffolds, and signaling: tissue architecture regulates development, homeostasis, and cancer. *Annual Review of Cell and Developmental Biology*, 22, pp. 287-309.
- Nishioka, N., Inoue, K., Adachi, K., Kiyonari, H., Ota, M., Ralston, A., Yabuta, N., Hirahara, S., Stephenson, R. O., Ogonuki, N., Makita, R., Kurihara, H., Morin-Kensicki, E. M., Nojima, H., Rossant, J., Nakao, K., Niwa, H., & Sasaki, H. (2009). The Hippo signaling pathway components Lats and Yap pattern Tead4 activity to distinguish mouse trophectoderm from inner cell mass. *Developmental Cell*, 16(3), pp. 398–410.

- Noisa, P., & Raivio, T. (2014). Neural crest cells: From developmental biology to clinical interventions. *Birth Defects Research. Part C, Embryo Today: Reviews*, 102(3), pp. 263–274.
- Nornes, S., Clarkson, M., Mikkola, I., Pedersen, M., Bardsley, A., Martinez, J. P., Krauss, S., and Johansen, T. (1998). Zebrafish contains two pax6 genes involved in eye development. *Mechanisms of Development*, 77, pp.185–196.
- Ohyama, T. Groves, A.K. Martin, K. (2007). The first steps towards hearing: mechanisms of otic placode induction. *The International Journal of Developmental Biology*, 51, pp. 463–472.
- Pan, D. (2010). The hippo signaling pathway in development and cancer. *Developmental Cell*, 19(4), pp. 491–505.
- Pankov, R., Cukierman, E., Katz, B. Z., Matsumoto, K., Lin, D. C., Lin, S., Hahn, C., & Yamada, K. M. (2000). Integrin dynamics and matrix assembly: tensin-dependent translocation of alpha(5)beta(1) integrins promotes early fibronectin fibrillogenesis. *The Journal of Cell Biology*, 148(5), pp. 1075–1090.
- Park, B.Y., & Saint-Jeannet, J.P. (2010). Induction and segregation of the vertebrate cranial placodes. San Rafael (CA): Morgan and Claypool Life Sciences.
- Parmigiani, C., McAvoy, J. (1984). Localisation of laminin and fibronectin during rat lens morphogenesis. *Differentiation*.28, pp. 53–61.
- Patan, S. (2004). Vasculogenesis and angiogenesis. *Cancer Treatment and Research*, 117, pp. 3–32.
- Penzel, R., Oswald, R., Chen, Y., Tacke, L., & Grunz, H. (1997). Characterization and early embryonic expression of a neural specific transcription factor xSOX3 in *Xenopus laevis*. *The International Journal of Developmental Biology*, 41(5), pp. 667–677.
- Pfeffer, P. L., Gerster, T., Lun, K., Brand, M., and Busslinger, M. (1998). Characterization of three novel members of the zebrafish Pax2/5/8 family: Dependency of Pax5 and Pax8 expression on the Pax2.1 (noi) function. *Development*, 125, 3063–3074.
- Pinto, I. M., Rubinstein, B., Kucharavy, A., Unruh, J. R., & Li, R. (2012). Actin Depolymerization Drives Actomyosin Ring Contraction during Budding Yeast Cytokinesis. *Developmental Cell*, 22, pp. 1247–1260.
- Porazinski, S. R., Wang, H., Furutani-Seiki, M. (2010). Microinjection of Medaka Embryos for use as a Model Genetic Organism. *Journal of Visualised Experiments* (46), e1937, doi:10.3791/1937

- Porazinski, S., Wang, H., Furutani-Seiki, M. (2011). Essential techniques for introducing medaka to a zebrafish laboratory--towards the combined use of medaka and zebrafish for further genetic dissection of the function of the vertebrate genome. *Methods in Molecular Biology (Clifton, NJ)*, 770, pp. 211–241.
- Porazinski, S., Wang H., Asaoka Y., Behrndt, M., Miyamoto, T., Morita, H., Hata, S., Sasaki, T., Krens, S. F. G., Osada, Y., Asaka, S., Momoi, A., Linton, S., Miesfeld, J. B., Link, B. A., Senga, T., Castillo-Morales, A., Urrutia, A. O., Shimizu, N., Nagase, H., Matsuura, S., Bagby, S., Kondoh, H., Nishina, H., Heisenberg, C-P., and Furutani-Seiki, M. (2015). YAP is essential for tissue tension to ensure vertebrate 3D body shape. *Nature*. Available at: <http://www.nature.com/doi/10.1038/nature14215>.
- Ramos, A., & Camargo, F. D. (2012). The Hippo signaling pathway and stem cell biology. *Trends in Cell Biology*, 22(7), pp. 339–346.
- Ridley, A.J., Schwartz, M.A., Burridge, K., Firtel, R.A., Ginsberg, M.H., Borisy, G., Parsons, J.T., & Horwitz, A.R. (2003). Cell Migration: Integrating Signals from Front to Back. *Science*, 302(5651), pp. 1704–1709.
- Rossier, O. M., Gauthier, N., Biais, N., Vonnegut, W., Fardin, M.-A., Avigan, P., Heller, E.R., Mathur, A., Ghassemi, S., Koeckert, M.S., Hone, J.C., & Sheetz, M. P. (2010). Force generated by actomyosin contraction builds bridges between adhesive contacts. *The EMBO journal*, 29(6), pp.1055–1068.
- Rozario, T., & Desimone, D. W. (2011). The Extracellular Matrix in Development and Morphogenesis: A Dynamic View. *Developmental Biology*, 341(1), pp. 126–140.
- Rozario, T., Dzamba, B., Weber, G. F., Davidson, L. a, & DeSimone, D. W. (2009). The physical state of fibronectin matrix differentially regulates morphogenetic movements in vivo. *Developmental Biology*, 327(2), 386–398.
- Rupp, P. A., & Little, C. D. (2001). Integrins in Vascular Development. *Circulation Research*, 89(7), pp. 566–572.
- Russell, L.B., Montgomery, C.S., (1982). Supermutagenicity of ethylnitrosourea in the mouse spot test: comparisons with methylnitrosourea and ethylnitrosourethane. *Mutation Research*, 92, pp. 193–204.
- Sahly, I., Andermann, P., and Petit, C. (1999). The zebrafish *eya1* gene and its expression pattern during embryogenesis. *Development Genes and Evolution*, 209, pp. 399–410.
- Sakaguchi, T., Kikuchi, Y., Kuroiwa, A., Takeda, H. & Stainier, D. Y. R. (2006) The yolk syncytial layer regulates myocardial migration by influencing

- extracellular matrix assembly in zebrafish. *Development* 133, pp. 4063–4072
- Salbreux, G., Charras, G., & Paluch, E. (2012). Actin cortex mechanics and cellular morphogenesis. *Trends in Cell Biology*, 22(10), pp. 536–545.
- Sasai, Y. (2013). Cytosystems dynamics in self-organization of tissue architecture. *Nature* 493, pp. 318–326.
- Saucedo, L.J., & Edgar, B.A. 2007. Filling out the Hippo pathway. *Nature Reviews: Molecular Cell Biology*, 8(8), pp. 613–621.
- Schartl, M., Wilde, B., Laisney, J. a G. C., Taniguchi, Y., Takeda, S., & Meierjohann, S. (2010). A mutated EGFR is sufficient to induce malignant melanoma with genetic background-dependent histopathologies. *The Journal of Investigative Dermatology*, 130(1), pp. 249–258.
- Schlegelmilch, K., Mohseni, M., Kirak, O., Pruszek, J., Rodriguez, J.R., Zhou, D., Kreger, B.T., Vasioukhin, V., Avruch, J., Brummelkamp, T.R., & Camargo, F.D. (2011). Yap1 acts downstream of ! α -catenin to control epidermal proliferation. *Cell*, 144(5), pp.782–795.
- Schlosser, G. (2006). Induction and specification of cranial placodes. *Developmental Biology*, 294(2), pp. 303–351.
- Schlüter, M. A., & Margolis, B. (2009). Apical lumen formation in renal epithelia. *Journal of the American Society of Nephrology: JASN*, 20(7), pp. 1444–1452.
- Scholey, J. M., Brust-mascher, I., & Mogilner, A. (2003). Cell division. *Nature*, 422(April), pp. 746–752.
- Schwarzbauer, J.E., & Sechler, J.L., 1999. Fibronectin fibrillogenesis: a paradigm for extracellular matrix assembly. *Current opinion in cell biology*, 11(5), pp. 622-627.
- Schwob, J.E., (2002). Neural regeneration and the peripheral olfactory system. *The Anatomical Record*. 269, pp. 33–49.
- Sims, J. R., Karp, S., & Ingber, D. E., (1992). Altering the cellular mechanical force balance results in integrated changes in cell, cytoskeletal and nuclear shape. *Journal of Cell Science*, 103, pp. 1215-1222.
- Singh, P., Carraher, C., & Schwarzbauer, J.E., (2010). Assembly of Fibronectin Extracellular Matrix. *Annual review of cell and developmental biology*, 26 (1), pp. 387-419.
- Shima, A., & Shimada, A., (1988). Induction of mutations in males of the fish *Oryzias latipes* at a specific locus after gamma-irradiation. *Mutation Research*, 198, pp. 93–98.

- Shima, A., & Mitani, H. (2004). Medaka as a research organism: past, present and future. *Mechanisms of Development*, 121(7-8), pp. 599–604.
- Sjodal, M., Edlund, T., & Gunhaga, L. (2007). Time of exposure to BMP signals plays a key role in the specification of the olfactory and lens placodes ex vivo. *Developmental Cell*, 13, pp. 141–149.
- Snow, C. J., Peterson, M. T., Khalil, A., & Henry, C. A. (2008). Muscle development is disrupted in zebrafish embryos deficient for fibronectin. *Developmental Dynamics: An Official Publication of the American Association of Anatomists*, 237(9), pp. 2542–2553.
- Song, H., Mak, K. K., Topol, L., Yun, K., Hu, J., Garrett, L., Chen, Y., Park, O., Chang, J., Simpson, R. M., Wang, C-Y., Gao, B., Jiang, J., & Yang, Y. (2010). Mammalian Mst1 and Mst2 kinases play essential roles in organ size control and tumor suppression. *Proceedings of the National Academy of Sciences of the United States of America*, 107(4), pp. 1431–1436.
- Staley, B.K., & Irvine, K.D., (2010). Warts and yorkie mediate intestinal regeneration by influencing stem cell proliferation. *Current Biology*, 20(17), pp. 1580–1587.
- Streit, A. (2004). Early development of the cranial sensory nervous system: from a common field to individual placodes. *Developmental Biology*, 276(1), pp. 1–15.
- Streit, A. (2008). The cranial sensory nervous system: specification of sensory progenitors and placodes. *Stem Book. Stem Cell Research Community*. pp. 1-18.
- Strauss O. (2005) The retinal pigment epithelium in visual function. *Physiological Reviews*. 85, pp. 845–881.
- Sudol, M. (1994). Yes-associated protein (YAP65) is a proline-rich phosphoprotein that binds to the SH3 domain of the Yes proto-oncogene product. *Oncogene*, 9(8), pp. 2145–2152.
- Sudol, M., Chen, H.I., Bougeret, C., Einbond, A., & Bork, P. (1995a). Characterization of a novel protein-binding module--the WW domain. *FEBS Letters*, 369, pp. 67-71.
- Sudol, M., Bork, P., Einbond, A., Kastury, K., Druck, T., Negrini, M., Huebner, K., & Lehman, D. (1995b). Characterization of the mammalian YAP (Yes-associated protein) gene and its role in defining a novel protein module, the WW domain. *The Journal of Biological Chemistry*, 270, pp. 14733-14741.
- Sun, Z., & Hopkins, N. (2001). Vhnf1, the MODY5 and familial GCKD-associated gene, regulates regional specification of the zebrafish gut,

- pronephros, and hindbrain. *Genes and Development*, 15(23), pp.3217–3229.
- Takeda, H., & Shimada, A. (2010). The art of medaka genetics and genomics: what makes them so unique? *Annual Review of Genetics*, 44, pp. 217–241.
- Tanaka, M., Kinoshita, M., Kobayashi, D., & Nagahama, Y. (2001). Establishment of medaka (*Oryzias latipes*) transgenic lines with the expression of green fluorescent protein fluorescence exclusively in germ cells: a useful model to monitor germ cells in a live vertebrate. *Proceedings of the National Academy of Sciences of the United States of America*, 98(5), pp. 2544–2549.
- Tawk, M., Araya, C., Lyons, D.A., Reugels, A.M., Girdler, G.C., Bayley, P.R., Hyde, D.R., Tada, M., & Clarke, J.D. (2007). A mirror-symmetric cell division that orchestrates neuroepithelial morphogenesis. *Nature*, 446(7137), pp. 797–800.
- Thisse, C., & Thisse, B. (2005) High Throughput Expression Analysis of ZF-Models Consortium Clones. ZFIN Direct Data Submission (<http://zfin.org>).
- Tibber, M.S., Kralj-Hans, I., Savage, J., Mobbs, P.G., & Jeffery, G. (2004). The orientation and dynamics of cell division within the plane of the developing vertebrate retina. *The European Journal of Neuroscience*, 19(3), pp. 497–504.
- Trinh, L. A., & Stainier, D. Y. R. (2004). Fibronectin Regulates Epithelial Organization during Myocardial Migration in Zebrafish. *Developmental Cell*, 6, pp. 371–382.
- Tryon, R.C., Higdon, C.W. & Johnson, S.L. (2011). Lineage relationship of direct-developing melanocytes and melanocyte stem cells in the zebrafish. *PloS one*, 6(6), p.e21010.
- Uwanogho, D., Rex, M., Cartwright, E.J., Pearl, G., Healy, C., Scotting, P.J., & Sharpe, P.T. (1995). Embryonic expression of the chicken Sox2, Sox3 and Sox11 genes suggests an interactive role in neuronal development. *Mechanisms of Development*, 49, pp. 23-36.
- Varelas, X., Samavarchi-Tehrani, P., Narimatsu, M., Weiss, A., Cockburn, K., Larsen, B.G., Rossant, J., & Wrana, J.L. (2010). The Crumbs complex couples cell density sensing to Hippo-dependent control of the TGF- β -SMAD pathway. *Developmental Cell*, 19, pp. 831–844.
- von Trotha, J.W., Campos-Ortega, J.A. & Reugels, A.M. (2006). Apical localization of ASIP/ PAR-3:EGFP in zebrafish neuroepithelial cells involves the oligomerization domain CR1, the PDZ domains and the C-terminal portion of the protein. *Developmental Dynamics*. 235, pp. 967–977.

- Wallace, K. N., & Pack, M. (2003). Unique and conserved aspects of gut development in zebrafish. *Developmental Biology*, 255(1), pp. 12–29.
- Wang, K., Degerny, C., Xu, M., & Yang, X-J. (2009). YAP, TAZ, and Yorkie: a conserved family of signal-responsive transcriptional coregulators in animal development and human disease. *Biochemistry and Cell Biology = Biochimie et Biologie Cellulaire*, 87(1), pp. 77–91.
- Watanabe, T., Asaka, S., Kitagawa, D., Saito, K., Kurashige, R., Sasado, T., Morinaga, C., Suwa, H., Niwa, K., Henrich, T., Hirose, Y., Yasuoka, A., Yoda, H., Deguchi, T., Iwanami, N., Kunimatsu, S., Osakada, M., Loosli, F., Quiring, R., Carl, M., Grabher, C., Winkler, S., Bene, F. D., Wittbrodt, J., Abe, K., Takahama, Y., Takahashi, K., Katada, T., Nishina, H., Hondoh, H., & Furutani-Seiki, M. (2004). Mutations affecting liver development and function in Medaka, *Oryzias latipes*, screened by multiple criteria. *Mechanisms of Development*, 121(7-8), pp. 791–802.
- Watanabe, T., Hosoya, H. & Yonemura, S. (2007). Regulation of myosin II dynamics by phosphorylation and dephosphorylation of its light chain in epithelial cells. *Molecular Biology of the Cell*, 18(2), pp. 605–616.
- Whitlock, K. E., & Westerfield, M. (2000). The olfactory placodes of the zebrafish form by convergence of cellular fields at the edge of the neural plate. *Development* (Cambridge, England), 127(17), pp. 3645–3653.
- Wittbrodt, J., Shima, A., & Scharl, M. (2002). Medaka--a model organism from the far East. *Nature Reviews. Genetics*, 3(1), pp. 53–64.
- Winkler, S., Loosli, F., Henrich, T., Wakamatsu, Y. and Wittbrodt, J. (2000). The conditional medaka mutation *eyeless* uncouples patterning and morphogenesis of the eye. *Development* 127, pp. 1911-1919.
- Wolpert, L., & Tickle, C. (2011). Principles of Development. Oxford University Press. 4th Edition. Oxford, UK.
- Yamada, K.M. & Cukierman, E. (2007). Modeling Tissue Morphogenesis and Cancer in 3D. *Cell*, 130(4), pp. 601–610.
- Zhang, H., Deo, M., Thompson, R. C., Uhler, M. D., & Turner, D. L. (2012). Negative regulation of Yap during neuronal differentiation. *Developmental Biology*, 361(1), pp. 103–115.
- Zhang, N., Bai, H., David, K.K., Dong, J., Zheng, Y., Cai, J., Giovannini, M., Liu, P., Anders, R.A., & Pan, D. (2010). The Merlin/NF2 tumor suppressor functions through the YAP oncoprotein to regulate tissue homeostasis in mammals. *Developmental cell*, 19, pp. 27–38.
- Zhang, Q., Checovich, W.J., Peters, D.M., Albrecht, R.M., & Mosher, D.F., 1994. Modulation of cell surface fibronectin assembly sites by lysophosphatidic acid. *Journal of Cell Biology*, 127, pp. 1447–1459.

- Zhang, Q., Magnusson, M.K., & Mosher, D.F., 1997. Lysophosphatidic acid and microtubule-destabilizing agents stimulate fibronectin matrix assembly through Rho-dependent actin stress fiber formation and cell contraction. *Molecular Biology of the Cell*, 8, pp. 1415–1425.
- Zhao, B., Wei, X., Li, W., Udan, R.S., Yang, Q., Kim, J., Xie, J., Ikenoue, T., Yu, J., Li, L., Zheng, P., Ye, K., Chinnaiyan, A., Halder, G., Lai, Z.C., & Guan, K.L. (2007). Inactivation of YAP oncoprotein by the Hippo pathway is involved in cell contact inhibition and tissue growth control. *Genes & Development*, 21(21), pp. 2747–2761.
- Zhao, B., Ye, X., Yu, J., Li, L., Li, W., Li, S., Yu, J., Lin, J.D., Wang, C.Y., Chinnaiyan, A.M., Lai, Z.C., & Guan, K.L. (2008). TEAD mediates YAP-dependent gene induction and growth control. *Genes & Development*, 22(14), pp.1962–1971.
- Zhao, B., Kim, J., Ye, X., Lai, Z.C., & Guan, K.L. (2009). Both TEAD-binding and WW domains are required for the growth stimulation and oncogenic transformation activity of yes-associated protein. *Cancer Research*, 69(3), pp. 1089–1098.
- Zhao, B., Li, L., Lei, Q., & Guan, K.L. (2010a). The Hippo-YAP pathway in organ size control and tumorigenesis: an updated version. *Genes & Development*, 24(9), pp. 862–874.
- Zhao, B., Li, L., Tumaneng, K., Wang, C.Y., & Guan, K.L. (2010b). A coordinated phosphorylation by Lats and CK1 regulates YAP stability through SCF (beta-TRCP). *Genes & Development*, 24(1), pp. 72–85.
- Zhong, C., Chrzanowska-Wodnicka, M., Brown, J., Shaub, A., Belkin, A.M., & Burridge, K., 1998. Rho-mediated contractility exposes a cryptic site in fibronectin and induces fibronectin matrix assembly. *Journal of Cell Biology*, 141, pp. 539–551.
- Zhou, D., Conrad, C., Xia, F., Park, J.S., Payer, B., Yin, Y., Lauwers, G.Y., Thasler, W., Lee, J.T., Avruch, J., & Bardeesy, N. (2009). Mst1 and Mst2 maintain hepatocyte quiescence and suppress hepatocellular carcinoma development through inactivation of the Yap1 oncogene. *Cancer Cell*, 16, pp. 425–438
- Zygar, C. A., Cook, T. L., & Grainger, R. M. (1998). Gene activation during early stages of lens induction in *Xenopus*. *Development (Cambridge, England)*, 125(17), pp. 3509–3519.

Chapter 8: Appendix

8.1 FN matrix is required for the formation of Cuvierian Ducts (CDs)

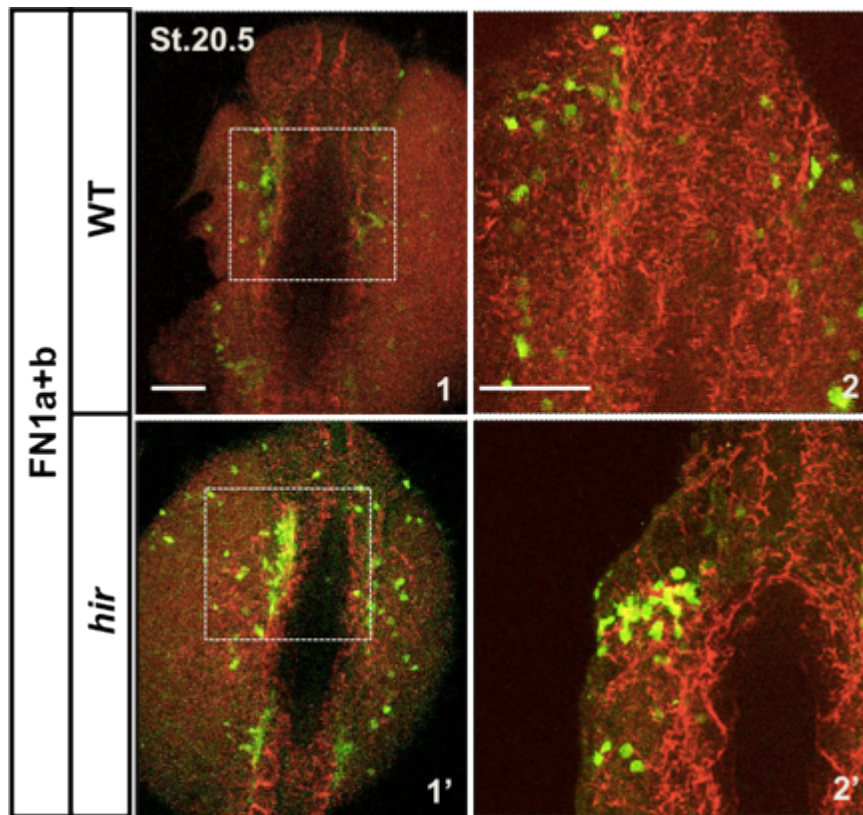


Figure 8.1 Fine Fironectin matrix is required for guiding the migration of endothelial precursors that forms Cuvierian Ducts (CDs). Dorsal views of whole-mount FN antibody staining (red) in the *fli::EGFP* transgenic embryos at st.20.5 (33 hpf). 2, 2' are the magnifications of boxed areas in 1 and 1' respectively. Scale bar = 100 μ m.

8.2 Publications

Porazinski, S.R., **Wang, H.**, Furutani-Seiki, M. 2011. Essential techniques for introducing medaka to a zebrafish laboratory--towards the combined use of medaka and zebrafish for further genetic dissection of the function of the vertebrate genome. *Methods in Molecular Biology*, pp. 211-41.

Miyamoto, T., Porazinski, S., **Wang, H.**, Borovina, A., Ciruna, B., Shimizu, A., Kajii, T., Kikuchi, A., Furutani-Seiki, M., Matsuura, S. 2011. Insufficiency of BUBR1, a mitotic spindle checkpoint regulator, causes impaired ciliogenesis in vertebrates. *Human Molecular Genetics*, 20 (10), pp. 2058-70.

Porazinski, S. R., **Wang, H.**, Furutani-Seiki, M. Dechoriation of Medaka Embryos and Cell Transplantation for the Generation of Chimeras. *Journal of Visualised Experiments*. (46), e2055, doi:10.3791/2055 (2010).

Porazinski, S. R., **Wang, H.**, Furutani-Seiki, M. Microinjection of Medaka Embryos for use as a Model Genetic Organism. *Journal of Visualised Experiments* (46), e1937, doi:10.3791/1937 (2010)

Porazinski, S., **Wang, H.**, Asaoka, Y., Behrndt, M., Miyamoto, T., *et al.* 2015. YAP is essential for tissue tension to ensure vertebrate 3D body shape. *Nature* doi:10.1038/nature14215